Max-Planck-Institut für Festkörperforschung

Stuttgart - Grenoble

MAX-PLANCK-INSTITUT
für Festkörperforschung

2001

Max-Planck-Institut für Festkörperforschung
Stuttgart - Grenoble

Wissenschaftlicher Tätigkeitsbericht

1. Januar 2001 – 31. Dezember 2001

Stuttgart: Max-Planck-Institut für Festkörperforschung
Heisenbergstrasse 1, D–70569 Stuttgart
Postfach: 80 06 65, D–70506 Stuttgart
Telefon: (0711) 6 89 – 0
Telefax: (0711) 6 89 – 10 10

Grenoble: C.N.R.S. – Max-Planck-Institut für Festkörperforschung
Avenue des Martyrs, B.P. 166
F-38042 Grenoble – Cedex 9 / France
Telefon: 33 / 476 85 56 00
Telefax: 33 / 476 85 56 10

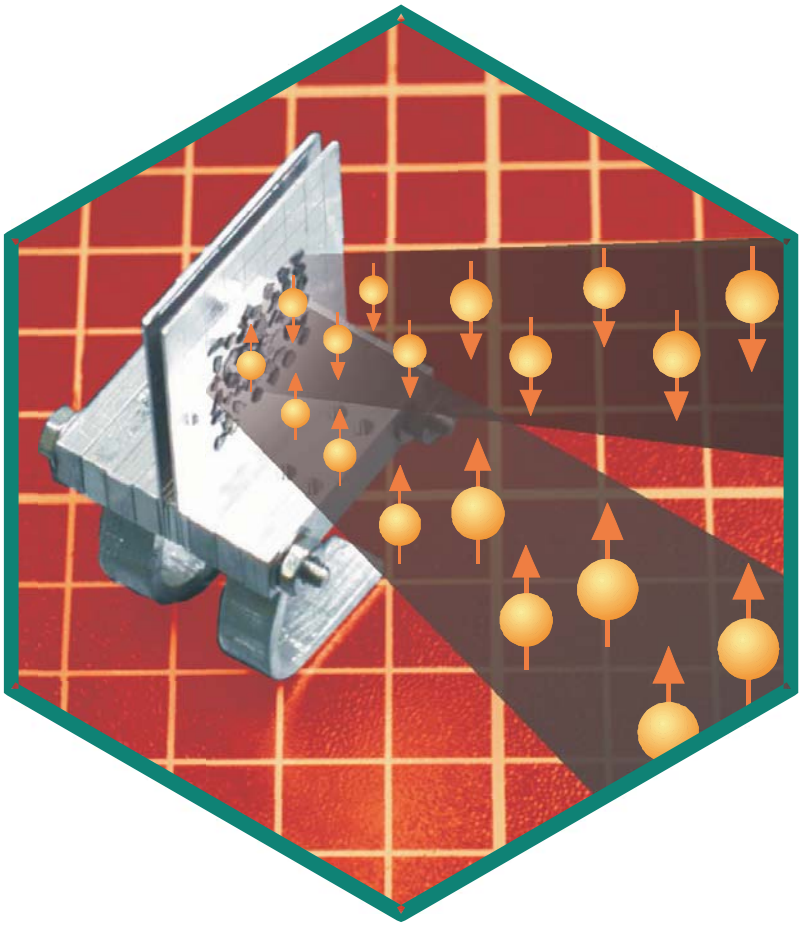

About the hexagon on the title page

The picture illustrates an investigation of a mosaic of crystals of the high temperature superconductor $Tl_2Ba_2CuO_6$ by spin-flip neutron scattering. In addition to a reversal of the neutron spin, magnetic excitations in the material cause a loss of neutron energy and momentum that can be detected in a spectrometer. An unusual, 'resonant' magnetic excitation mode observed in earlier neutron scattering experiments on some copper oxide superconductors has played an important role in the scientific debate about the origin of high temperature superconductivity. However, such experiments typically require large single crystals that are only available for very few families of copper oxides. The question of whether this mode is generic to all high temperature superconductors, or whether it is a consequence of peculiarities of the crystal structure of specific compounds, had remained unanswered for a long time. In collaboration with French and Russian researchers, a group at the MPI-FKF has now used a new approach to this problem [Science **295**, 1045 (2002)]. They assembled a mosaic of about 300 small single crystals of $Tl_2Ba_2CuO_6$, a material with both a high superconducting transition temperature $T_c \approx 90\,\mathrm{K}$) and an exceptionally simple crystal structure. The total volume of the crystal array proved large enough to detect the resonant mode in this prototypical high-T_c material. This experiment establishes the magnetic mode as one of very few generic spectral features of the copper oxides that will have to be considered by all theories of high temperature superconductivity.

Dieser Bericht will Ihnen einen Einblick in die wissenschaftlichen Arbeiten des Instituts im Jahre 2001 vermitteln. Er kann natürlich nicht vollständig sein. Die zahlreichen Publikationen lassen sich inhaltlich nicht auf wenige Seiten reduzieren. Der erste Teil soll Ihnen einen Eindruck von den wissenschaftlichen Aktivitäten der einzelnen Abteilungen und Gruppen geben. Der zweite Teil enthält die vollständige Veröffentlichungsliste sowie sonstige nützliche Informationen über das Institut. Einzelheiten können Sie auf der Web-Seite des Instituts finden (www.fkf.mpg.de).

Wir haben sehr bedauert, dass unser Kollege Michele Parrinello zum 1.7.2001 das Institut verlassen hat. Er hat einen Ruf an die ETH Zürich angenommen und ist außerdem Direktor des Swiss Center for Scientific Computing in Manno. Das Kollegium ist sehr froh darüber, dass Herr Parrinello dem Institut als auswärtiges wissenschaftliches Mitglied verbunden bleibt. Wir sind zur Zeit intensiv auf der Suche nach einem geeigneten Nachfolger.

Mit großer Freude konnten wir zum 1. November 2001 unseren neuen Kollegen Walter Metzner begrüßen. Er kam von der RWTH Aachen zu uns und leitet jetzt die Abteilung Theorie II.

Ende 2001 haben wir den Kollegen Peter Wyder in den Ruhestand verabschiedet.

Wir danken allen Mitarbeitern für die gezeigten Leistungen und die sehr gute Arbeit. Sie sind Grundlage für eine wegweisende Gestaltung der Zukunft unseres Instituts.

Stuttgart – Grenoble DAS KOLLEGIUM

April 2002

Contents

Selected Research Reports

Strongly correlated systems

Superconductivity

New structures and materials

Theory

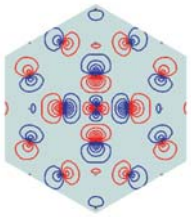

The ANDERSEN department attempts to improve the understanding of the properties of condensed matter by means of electronic structure calculations. This involves performing parameter-free density-functional (DF) calculations for specific systems of current interest, extending DF theory and going beyond, deriving electronically correlated model Hamiltonians, solving these Hamiltonians, and developing numerical tools for doing so. For most applications, it is crucial to use an intelligible, general, and numerically efficient single-electron representation, and this causes recurrent developments of the muffin-tin orbital (MTO) method. With the newest version we could identify the essential material-dependent one-electron parameter for the hole-doped high-temperature superconducting cuprates and derive the corresponding conduction-band orbitals. Savrasov's linear-response method enabled us to perform the first, complete electron-phonon calculation for magnesium diboride. Finally, electronic and transport properties of alkali- and field-doped fullerenes and other strongly correlated systems were studied by means of Quantum Monte Carlo calculations. The relation between superconductivity and structure was investigated for the field-doped fullerenes. The large-T resistivity of the high-T_c cuprates was shown to be consistent with resistivity saturation. [34,68]

⬡ Wannier-like orbital for the conduction band of the high temperature superconductor $HgBa_2CuO_4$, plotted in the CuO_2-plane. This orbital has Cu $d_{x^2-y^2}$ symmetry and extends over several neighboring oxygen (*) and copper (+) sites. It was computed with the third-generation linear muffin-tin orbital (LMTO) method, using the local density approximation (LDA).

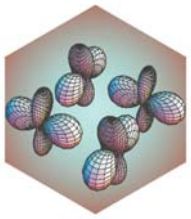

The electronic properties of solids are analyzed and computed in METZNER's department with a main emphasis on systems where electronic correlations play a crucial role, such as cuprates, manganites and other transition metal oxides. Besides symmetry breaking phase transitions leading to magnetism, orbital and charge order, or superconductivity, correlations can also cause electron localization and many other striking many-body effects not described by the generally very successful independent electron approximation. Our present research focuses in particular on high temperature superconductors with their complex interplay of magnetic, superconducting and charge correlations, and also on manganites and vanadates, whose electronic properties are determined by the interplay of orbital, spin and charge degrees of freedom. Another topic is the influence of lattice degrees of freedom on electronic properties, via Jahn-Teller distortion and electron-phonon interaction. Besides bulk properties of one-, two- and three-dimensional systems also problems with a mesoscopic length scale are studied. In particular, a recent research project deals with inhomogeneous quantum wires. The correlation problem is attacked with various numerical and field-theoretical techniques: exact diagonalization, density matrix renormalization group (DMRG), dynamical mean-field theory (DMFT), functional renormalization group and (1/N)-expansion. Modern many-body methods are not only being applied, but also further developed within our group. [53,63]

⬡ Orbital order in a single layer of undoped $LaMnO_3$. The study of electronic properties of doped manganites, which show such remarkable phenomena like the colossal magnetoresistance, is an active research field because of the subtle interplay of charge, orbital, spin and lattice degrees of freedom.

Physics

KEIMER's department studies the structure and dynamics of highly correlated electronic materials by spectroscopic and scattering techniques. Topics of particular current interest include the interplay between charge, orbital and spin degrees of freedom in transition metal oxides and the mechanism of high-temperature superconductivity. Experimental techniques being used include elastic and inelastic neutron scattering, normal and anomalous X-ray scattering, Raman scattering off and in resonance as well as in high magnetic fields, spectral ellipsometry (including synchrotron radiation as a source), and optical and X-ray measurements under high pressure and high magnetic fields. Experiments at external neutron sources are carried out on a regular basis, and a spectrometer at the new research reactor FRM-II in Munich is under construction. The latter instrument will use a novel combination of triple axis and neutron spin echo techniques to optimize the energy resolution and allow the determination of lifetimes of magnetic and lattice vibrational excitations throughout the Brillouin zone. The group is a member of the CMC-CAT consortium operating an insertion-device synchrotron beamline at the Advanced Photon Source at Argonne National Lab (USA), and maintains close contact with research groups at the NSLS at Brookhaven National Lab (USA). At the NSLS and at the ANKA synchrotron in Karlsruhe, the group also operates Fourier ellipsometers for the far infrared spectral range. Close collaborations also exist with the crystal growth service group at the MPI where large, high-quality single crystals of oxide compounds are prepared with state-of-the-art optical furnaces, as well as with the high pressure and technology service groups. [49,82,85]

⬡ Central part of the novel triple axis spectrometer being built by Keimer's group at the research reactor FRM-II in Munich. Two pairs of resonant spin echo coils designed to achieve extremely high energy resolution are shown in both incident and scattered beams.

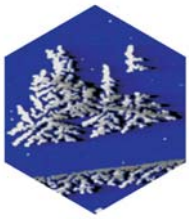

Research efforts in KERN's department are centered on nanometer-scale science and technology, primarily focusing on solid state phenomena that are determined by small dimensions and interfaces. Materials with controlled size, shape and dimension ranging from clusters of a few atoms to nanostructures with several hundred or thousand atoms, to ultra-thin films with nanometer thickness are studied.

A central scientific goal is the detailed understanding of interactions and processes on the atomic and molecular scale. Novel methods for the characterization and control of processes on the atomic scale as well as tools to manipulate and assemble nanoobjects are developed. Of particular interest are: fundamentals of epitaxial growth and self-organization phenomena, atomic scale fabrication and characterization of metal, semiconductor and molecular nanostructures, quantum electronic transport in nanostructures, atomic scale electron spectroscopy and optics on the nanometer-scale. As surface phenomena play a key role in the understanding of nanosystems the structure, dynamics and reactivity of surfaces in contact with gaseous or liquid phases are also in the focus of interest. [29,31,65]

⬡ The scanning tunneling microscope image in the logo of the Abteilung Kern shows a silver dendrite grown at 130 K on a platinum (111) surface.

The electronic properties of heterostructures, quantum wells, superlattices and molecular systems, in particular the influence of quantum phenomena on the transport and optical response are the main topics in the VON KLITZING's department. Optical and transport measurements in magnetic fields up to 20 Tesla and temperatures down to 20 mK are used to characterize the systems. The quantum Hall effect is studied by analyzing electrical breakdown, time-resolved transport, edge channels and the behavior of composite fermions. Electron-phonon interactions in low-dimensional systems and the phonon transmission through interfaces are investigated with ballistic phonon techniques. Time-resolved photoconductivity, luminescence, and Raman measurements in magnetic fields are methods of characterizing the low-dimensional electronic systems. A strong current interest is the preparation of nanostructures either by self-organized growth or by lithographic and synthetic routes (nanotubes and other synthetic nanoparticles) and the investigation of coupled two- and zero-dimensional electronic systems (electron drag, Kondo resonances, single electron transistor). The experiments are supported within the group by theoretical investigations of the transport and dynamic response of these low-dimensional electronic systems. [27,37,58]

⬡ Demanding technologies are needed for the preparation of devices used in quantum transport experiments. The figure shows a typical example where the combination of interrupted epitaxial growth, special etching processes, focused ion beam writing, contact diffusion, and gate evaporation leads to two electron layers with a distance of only 10 nm and separate contacts.

The Grenoble HML-Außenstelle of the Institute operates jointly with the French Centre National de la Recherche Scientifique (C.N.R.S.) the Grenoble High Magnetic Field Laboratory. During the first couple of years, there were two separate laboratories, the French and the German part, respectively; these have then been put together into one single laboratory on the basis of a contract for collaboration; Frenchmen and Germans are working together, with one director and one single technical and scientific policy. This contract of collaboration between the C.N.R.S. and the MPG will end in 2004. The aim of the laboratory is to provide high magnetic fields with a wide range of scientific instrumentation (temperatures 30 mK to 1000 K, pressures up to 24 GPa, voltages nV to 50 kV, currents pA to several kA, etc.) allowing many interesting investigations. In the years 1990/1991, most of the technical installations were renewed and the dc-power supply was extended from 10 MW to 25 MW. We now have one of the world's most modern power and cooling installation for the generation of high magnetic fields in operation with a 20 MW resistive magnet producing a world record field in the 30 Tesla range in a bore of 5 cm. In addition, the MPG and the C.N.R.S. decided to finance a new hybrid system for fields in the 40 Tesla range. All these magnets guarantee the leading role of the Grenoble HML also in the years to come. In accordance with its mission, the in-house research at the HML shows a considerable diversification into several fields in condensed matter physics, where the use of high magnetic fields is interesting or necessary, such as the study of metals, semiconductors, 2D electronic systems, magneto-optics, high-field NMR and ESR, polymers and all sorts of soft matter and even some biological systems. [24,74]

⬡ SCOTS (Stress and Cooling Optimized Tubular Solenoids) and Bitter Coil. High-power magnets to produce stationary magnetic fields of more than 30 T with 20 MW.

Chemistry

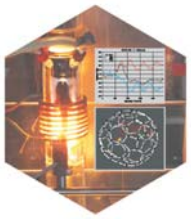

JANSEN's department puts the main emphasis on basic research in the field of preparative solid state chemistry with the goal of developing modern materials. Classes of materials currently under investigation include oxides and nitrides of non-metals as well as fullerenes, e.g., new binary and ternary oxides synthesized under high oxygen pressure, superconducting oxides, ionic conductors, structural oxide-ceramics and pigments, amorphous inorganic nitridic covalent networks, or endohedral fullerenes and fullerides. Besides employing traditional solid state synthesis methods, a large number of alternative techniques is used, e.g., the sol-gel-process, synthesis under high pressure, via an rf-furnace, at low temperatures in liquid ammonia, or by electrochemical methods. Optimizing the syntheses of these materials is only a first, though crucial step, however. In addition, their chemical and physical properties, in particular optical, electrical and magnetic behavior, are analyzed both at high and low temperatures, with particular emphasis on X-ray diffraction and spectroscopic methods. This provides the basis for placing the results in the proper context regarding structure-property-relationships and modern concepts of bond-theory.

A long-term goal of the department is to increase the predictability of solid state chemistry, i.e., to predict the existence of not-yet-synthesized compounds, calculate their properties, and finally provide prescriptions for their synthesis. This work involves both theoretical and synthetic aspects; on the theoretical side, structure candidates are determined using global optimization techniques, while on the preparative side kinetically controlled types of reactions that allow low-temperature synthesis of (possibly metastable) compounds, e.g., electrochemical reactions or the use of molecular precursors, are being developed. [96,99]

⬡ When simultaneously evaporating graphite and a metal in a rf-furnace, endohedral fullerenes can be synthesized in relatively high yields. Individual representatives like $Ba@C_{74}$ are isolated by HPLC and subsequently characterized spectroscopically. The structures and the dynamic behavior of these fullerenes are investigated using the Car-Parrinello molecular dynamics method.

MAIER's department is concerned with physical chemistry of the solid state, more specifically with chemical thermodynamics and transport properties. Of particular interest are ion conductors (such as proton, metal ion and oxygen ion conductors) and mixed conductors (especially perovskites). A major theme is the understanding of mass and charge transport, chemical reactivities and catalytic activities in relation to defect chemistry. Besides the clarification of local properties in terms of elementary mechanisms, also their superposition to the overall system property is investigated (inhomogeneous systems, especially multiphase systems and functional ceramics). In this context interfaces and nanosystems are in the focus of interest. The research ranges from atomistic considerations and phenomenological modeling to electrochemical and thermochemical experiments. Since electrochemical investigation immediately affects the coupling of chemical and electrical phenomena, the research is directed towards both basic solid state problems as well as energy and information technology (fuel cells, chemical sensors). [39,42,43]

⬡ Ionic and electronic charge carriers (point defects) are the relevant particles as far as chemical kinetics and mass transport is concerned. They are establishing the interaction with the neighboring phases and act on electrical and chemical driving forces.

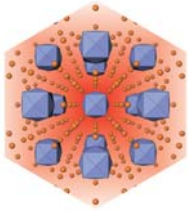

SIMON's department emphasizes the investigation of metal-rich compounds (main group metals, *d* and *f* metals). The purpose of the work is on one side the development of concepts of structure and bonding (e. g., systematization of condensed cluster concept) and on the other side the search for new materials (e.g., metal-rich compounds, transition metal clusters, reduced rare earth halides, hydride, carbide, boride, boride carbide, aluminide and silicide halides of the rare earth metals, alkali and alkaline earth metal suboxides and subnitrides), phase relationships and relations between structure, chemical bonding and properties. Electron microscopy is used to characterize microcrystalline phases up to full structure refinement as well as analysis of real structure. Superconductivity is of special interest following a chemical view of the phenomenon in terms of a tendency towards pairwise localization of conduction electrons. Other fields of interest are structures of molecular crystals (in situ grown crystals of gases and liquids). Experimental techniques like diffractometry with X-rays and neutrons, XPS, UPS, HRTEM and measurements of magnetic susceptibility as well as electrical transport properties are used. [76,102,104,112]

⬡ $Ba_{14}CaN_6Na_{14}$ – Picodispersed salt in a metal.

Scientific Service Groups

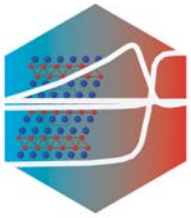

The CHEMICAL SERVICE GROUP (Kremer) develops techniques and provides experimental facilities to support all experimental groups of the Institute with the characterization of the transport and magnetic properties of new compounds and samples. This objective requires a high versatility of all experimental methods including the development and cultivation of experimental setups to perform measurements on very small samples by contactless methods under inert gas conditions. Available are commercial SQUID magnetometers, ac-susceptometers allowing measurements down to 0.3 K and magnetic fields up to 12 T, a contactless microwave transport method, ac- and dc-electrical transport measurements in magnetic fields up to 12 T and temperatures down to 0.3 K. Materials currently under investigations are novel superconductors, unusual magnetoresistive materials, low-dimensional and frustrated magnetic systems and intermetallic rare earth compounds. [93]

⬡ $Y_2C_2X_2$ – A halide superconductor. The white solid lines symbolize the electrical resistivity, the heat capacity and the magnetic susceptibility proving $Y_2C_2I_2$ to be a superconductor with a T_c of 10 K.

The COMPUTER SERVICE GROUP (Burkhardt) supports ≈150 workstations in the various Departments and Service Groups of the Institute. The services include hardware bring up and maintenance, installation and administration of various UNIX-based operating systems (AIX, Tru64 Unix, HP-UX, Linux and Solaris) and a common application software server for these systems. Furthermore the group administers 3 parallel computers (one 84-processor IBM RS/6000 SP/2, one 20-processor CRAY T3E and one Siemens hpc-line Linux-Cluster with 32 CPUs) for the Andersen and Metzner theory groups. A PC hard- and software standard has been defined and is being continuously adapted to the rapidly changing market. This standard is now accepted throughout the Institute, allowing the group to offer centralized PC application services coupled with partial outsourcing of the initial PC software installation. This way almost 100 newly installed PCs were delivered in 2001 (69% WinNT, 17% Linux, 11% Win9x). The ADSM based central backup and archive service is open to all supported systems. At the end of the year approximately 170 computers used the automated nightly backup resulting in a total storage volume of 5.5 Terabyte. Email is now handled by a central Linux based Email server, providing improved virus protection and a Web interface for the scientists abroad.

⬡ View inside the Tape Library of the DV-FKF. Every night the data of 170 computers of the Institute is backed up. At the moment, the total ADSM backup and archive volume amounts to 5.5 Terabyte.

The CRYSTAL GROWTH SERVICE GROUP (Lin) applies, modifies and develops techniques, such as traveling solvent floating zone (TSFZ) with infrared image furnace), Bridgman, top seeded solution growth and Czochralski methods to grow single crystals from the melt or solution. A wide variety of crystals has been supplied to the physics and chemistry departments at the MPI-FKF and to outside collaborators. These range from isotopically pure semiconductors to fullerenes and transition metal oxides. Two new floating zone furnaces have been installed in 1999 and 2000 and are now fully operational. They are used predominantly to grow large single crystals of transition

metal oxides for neutron and optical spectroscopy as well as for growth of manganese oxides. Typical examples are superconducting oxides $REBa_2Cu_3O_{7-\delta}$, $Bi_2Sr_2Ca_{n-1}Cu_nO_{2+4n+\delta}$ (n = 1, 2, 3), $RE_{2-x}M_xCuO_4$ and colossal magnetoresistance oxides $RE_{1-x}M_xMnO_3$ (RE: rare earth and M = Sr, Ce, Pb and Nd). Gas phase methods are modified to grow crystals of II-VI and III-V compounds with defined isotopic components from low amounts of source materials. The growth of the new compound $RuSr_2GdCu_2O_8$ is in progress. Accurate characterization is done with the aim of improving and obtaining high quality single crystals, e.g., superconductivity, crystal composition including oxygen content, structure and phase determined using SQUID, X-ray diffraction (XRD) method, differential thermal and thermal gravimetry analysis (DTA/TGA). [88]

⬡ A view of the inside chamber of the four ellipsoidal infrared image (TSFZ) furnace.

Research within the HIGH PRESSURE SERVICE GROUP (Syassen) is concerned with the effects of hydrostatic pressure on structural, lattice dynamical and electronic properties of crystalline solids and their high-pressure phases. The primary experimental methods are synchrotron X-ray diffraction and low-temperature optical spectroscopies. Materials currently under investigation are intermetallic compounds, semiconductors and their heterostructures, transition metal oxides, and low-dimensional solids. Pressure experiments in other research groups are supported through design of equipment and in scientific collaborations. [71,106,110]

⬡ Schematic view of a diamond window high pressure cell.

The CENTRAL INFORMATION SERVICE (Marx, Schier) for the institutes of the Chemistry, Physics and Technology (CPT) section of the Max Planck Society, situated at the Max Planck Institute for Solid State Research in Stuttgart, has access to many external commercial databases, especially from the host STN International (Fachinformationszentrum Karlsruhe). The information service offers searches for scientists at Max Planck Institutes, which cannot be done by themselves due to complexity or lack of access. Furthermore, the scientists are welcome to ask for help and support in all questions concerning scientific information.

Today, databases are a major tool in processing the actual information flood in science. Literature databases provide links to the original scientific literature. They are mostly online versions of printed abstract services like Chemical Abstracts or Physics Abstracts. Compound or material related searches are done in the files of the Chemical Abstracts Service, to which is no general access for Max Planck scientists until now. Beside these databases, covering general topics like chemistry and physics, there are many highly specialized databases on specific topics like material science, engineering, environment and many others. In addition various national and international patent files are available.

Factual databases enable searching numerical data like chemical and physical properties of substances. The Science Citation Index provides the possibility to retrieve the citing papers of publications as well as total citation statistics of scientists, institutes or research disciplines for research evaluation.

⬡ The archives of science are growing from the flood of information: One of the about 30 million substances in the compound file of the American Chemical Abstracts Service. Effective databases and search systems in conjunction with document delivery systems produce relief.

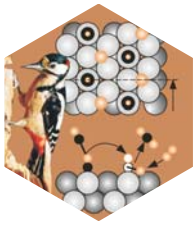

The main goal of the INTERFACE ANALYSIS SERVICE GROUP (Starke) in terms of service is to quantify the chemical composition and to characterize the atomic geometry of solid-solid and gas-solid interfaces. Our scientific interest is focused on an atomistic understanding of mechanisms that control the reactivity at transition metal surfaces and the corresponding oxide surfaces, and how the reactivity is related to the actual surface structure and its electronic properties. We are employing the techniques of quantitative low energy electron diffraction and spectroscopic methods. For the service group three new machines will be purchased. First, TOF-SIMS (time-of-flight secondary ion mass spectrometry) will be used to quantify the chemical composition at interfaces as a function of the depth. Additionally, this system is equipped with a preparation chamber for in situ preparation of surfaces and ultra thin films. A white-light interferometer in combination with an atomic force microscope is used to analyze the crater profiles after sputtering. Second, a high-end ESCA (Electron Spectroscopy for Chemical Analysis) system in combination with an extended transfer system which comprises an UHV chamber for photo-electron diffraction, a high pressure reaction cell, an infrared Fourier-transform spectrometer, and a preparation chamber for the preparation of molecular films on metal surfaces will be ionstalled. The third equipment will be an Auger microscope with a LaB_6 filament, reaching a lateral resolution of 30 nm in the spectroscopic mode and 10 nm in secondary electron imaging. [115]

⬡ Interface analysis includes the study of surface reactions (right) and the erosion of solid materials (left) by sophisticated methods.

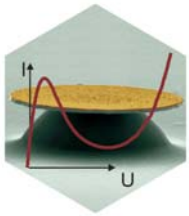

Main subject in the MBE SERVICE GROUP (Dietsche, Schmidt) is the preparation and characterization of III/V and group IV semiconductor heterostructures. We apply molecular beam epitaxy (MBE) for the material systems AlGaAs/GaAs, InGaAs and AlInGaP on GaAs substrate, and SiGe/Si on Si substrate. Our main interest is the preparation of low-dimensional structures.
Lateral confinement is achieved by MBE-growth on patterned substrates, and by island formation in epitaxial growth of strained heterostructures. We are also investigating an atomically defined in situ etching technique based on $AsBr_3$ within the MBE system. The group IV element MBE activities are concentrated on the self-assembly of Ge/Si nanostructures and on Si/SiGe Esaki-diodes for new Si based devices. Recently, a new focus is the formation of free-standing semiconductor nanotubes. The preparation is controlled by selective under-etching of strained epitaxial semiconductor bilayers. [21]

⬡ Si/SiGe interband tunneling diode. A room temperature peak to valley current ratio of 6 is achieved on Si due to extremely sharp doping profiles and atomically defined heterostructures prepared by MBE.

The OPTICS AND SPECTROSCOPY SERVICE GROUP (Kuhl) comprises the spectroscopy service lab and the ultrafast optics lab. The spectroscopy service lab provides experimental facilities for studying the optical properties of condensed matter by standard spectroscopic techniques. The laboratory is equipped with commercial grating and Fourier-spectrometers which allow absorption and reflection measurements over the total range from the ultraviolet to the far infrared. Data can be routinely taken at temperatures between 4 and 300 K. Recently, the sample characterization techniques have been extended by standard Raman spectroscopy. The primary research subjects of the ultrafast op-

tics lab are time-resolved studies of ultrafast optical and electrical phenomena in solids. Several pico- and femtosecond laser systems including devices for the generation of sub-10 fs pulses as well as for the amplification of 150 fs pulses to 5 μJ at 200 kHz are available. Broad tunability of the photon energy is attainable by optical parametric amplifiers. Time-resolved photoluminescence, pump-probe experiments, degenerate four-wave-mixing and coherent Raman techniques are employed to investigate the coherent and incoherent relaxation dynamics of excitons, free carriers (electrons and holes) and phonons as well as carrier transport phenomena. Materials preferentially under investigation are III-V and II-VI semiconductors, in particular low-dimensional systems (quantum wells, quantum wires, and quantum dots). The variation of the relaxation processes and times as a function of the dimensionality of the carrier system is a central topic of the research.
Important current research projects are dealing with coherent light / matter coupling, control of light / matter interaction by nanostructuring, generation and dynamics of coherent phonons, generation and characterization of ultrashort optical pulses, pico- and subpicosecond electronics. [45]

⬡ Optical parametric amplifier generating tunable femtosecond pulses for coherent semiconductor spectroscopy.

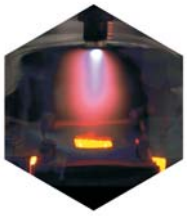

The TECHNOLOGY SERVICE GROUP (Habermeier) offers service work in the fields of thin film deposition technologies, microlithography and fabrication of contacts to semiconductors and ceramic materials. The experimental facilities for the thin film work include the conventional high vacuum evaporation and sputtering (dc, rf and reactive) techniques. Additionally, pulsed laser deposition facilities are installed to prepare thin films with complex chemical composition such as high temperature superconductors, perovskites with colossal magnetoresistance and ferroelectric materials. In the area of microlithography simple masks with design rules down to 5 μm can be realized in one photoreduction step. Recently, a Laser Mask Macro Projector has been installed which offers the possibility for direct, chemistry-free thin film patterning. The etching techniques available include wet chemical etching, ion milling and plasma etching as well. The research activities of the group are closely related to the service tasks. Thin film deposition of doped Mott insulators such as high temperature superconductors and doped rare earth manganites exhibiting colossal magnetoresistance play a central role. Pulsed laser deposition and rf-sputtering are the techniques applied. The main focus of interest is currently the systematic study of epitaxial strain and thus a tailored modification of the arrangement of bonding angles and bonding distances in the CMR and HTS thin films. Additionally, the preparation and investigation of magnetic and superconducting oxide superlattices (manganites, ruthenates and cuprates) and their mutual electronic interaction special heterostructures have been fabricated. Bilayer structures consisting of ferromagnetic and antiferromagnetic manganites are used to study the magnetic exchange bias effects, FM / SC / FM trilayers are used to investigate spin-polarized tunnel phenomena in HTC thin films. [56]

⬡ Pulsed laser deposition has become a widespread technique for the fabrication of epitaxial thin films of multicomponent materials like doped lanthanum manganites and superconducting materials.

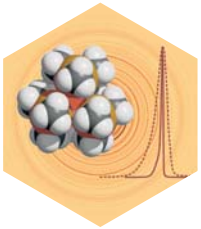

The X-ray Diffraction Service Group (Dinnebier) provides X-ray diffraction measurements of single crystals and powders in the laboratory at room and low temperature. Research within the X-ray diffraction service group is mainly concerned with the determination of crystal structures and microstructural properties (strain, domain size) of condensed matter from powder diffraction data. In addition, methodological development within this area is pursued. Special expertise in the field of solution and refinement of crystal structures from powder diffraction data can be provided. Scientific cooperation in the field of non-routine structure determination (phase transitions, disorder, anisotropic peak broadening etc.) from powders is offered. This includes the performance of experiments at synchrotron and neutron sources at ambient and non-ambient conditions. Materials currently under investigation include organometallic precursors, binary and ternary oxides, ionic conductors, electronic and magnetic materials, and rotator phases. [78]

⬡ Quasispherical molecule of tetrakistrimethylstannylsilane with underlying two dimensional image plate powder diffraction pattern. The superimposed Bragg reflections demonstrate the difference in resolution between laboratory and synchrotron data.

Nanostructures

Since many years nanostructured materials are an interdisciplinary research field of our Institute. This trend seems quite natural since ever decreasing semiconductor devices and constantly increasing synthetic structures are about to overlap in size. The following contributions present some highlights ranging from lithographically nanostructured semiconductors over carbon nanotubes to virus particles.

Fabrication of free-standing nanoobjects

Ch. Deneke, C. Müller, and O.G. Schmidt

Two different approaches are generally used to fabricate nanometer structures. The bottom-up approach relies on the self-formation process of self-assembling nanostructures, such as semiconductor quantum dots or chemically synthesized nanoparticles, whereas the top-down approach utilizes lithographic and etching techniques to create well-defined and well-positioned nano-electromechanical systems (NEMS). A huge impact is expected if these two approaches could be merged into one single technology.

Recently, it was shown that semiconductor layers form a new class of free-standing nanoobjects if they are released from their substrate [V.Y. Prinz *et al.*, Physica E **6**, 828 (2000); O.G. Schmidt *et al.*, Nature **410**, 168 (2001); O.G. Schmidt *et al.*, Advanced Materials **13**, 756 (2001)]. The fabrication process combines self-formation with standard semiconductor processing techniques and therefore establishes a powerful integration of top-down and bottom-up approach.

A layer structure consisting of a thin sacrificial layer followed by one or more top layers are grown pseudomorphically onto a substrate by solid source molecular beam epitaxy. The sacrificial layer is than removed ex-situ with selective etching. As a result the top layer structure is released from the substrate and can form a novel kind of nanoobject. We can distinguish two different methods for nanotube formation.

For the first method a single layer is grown on top of a sacrificial layer. After the ex-situ etching step the top layer wraps up and folds back onto its own substrate (see Fig. 1). This method requires not necessarily any special features of the layer structure and is therefore general. The second method involves a special design of the layer structures. Two different and lattice mismatched materials

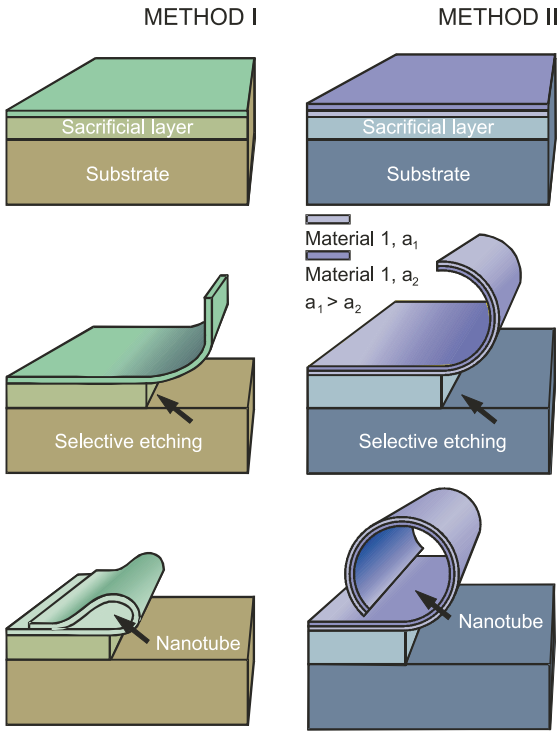

Figure 1: *Folding (Method I) an rolling up (Method II) nanotubes.*

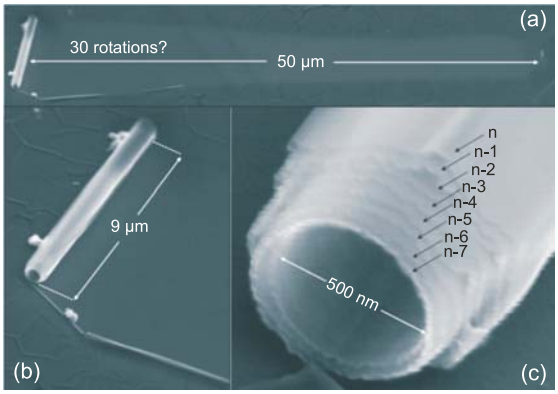

Figure 2: *Multi-wall InGaAs nanotube on a GaAs surface. (a) The tube has rolled up over a distance of 50 µm and has a length of 9 µm (b). (c) Magnification of the lower opening, demonstrating at least eight full rotations.*

are grown pseudomorphically on top of each other introducing thus strain in the structure. The strain results in a momentum that forces the top layers to roll up when released from the substrate. The position of the nanotube is defined by the starting point and the etching time, while the diameter can be scaled by changing the layer thicknesses and the built-in strain.

A layer sequence of 2.83 nm AlAs, 1.9 nm $In_{0.33}Ga_{0.67}As$ and 3.5 nm GaAs was grown on top of a GaAs (001) substrate. The InGaAs/GaAs bilayer is inherently strained due to the lattice mismatch between the two materials. During the ex-situ etching step the AlAs layer is removed by HF solution. As a result the bilayer is released from its substrate. A scanning electron microscope of the resulting nanotube is presented in Fig. 2. The tube has rolled up over a distance of 50 μm and has a diameter of approximately 500 nm. We therefore conclude that the nanotube has performed about 30 rotations.

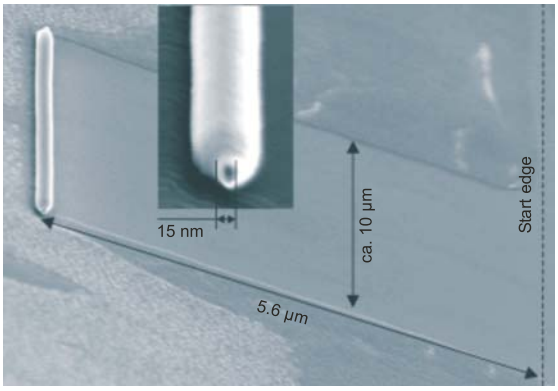

Figure 3: *Nanotube with a diameter of 15 nm. The tube rolled over a distance of 6 µm performing 30 rotations.*

Figure 3 shows a nanotube obtained from a layer structure consisting of 2.83 nm AlAs/ 0.41 nm $In_{0.33}Ga_{0.67}As$ / 1.25 nm GaAs. This nanotube has a diameter of 15 nm and has rolled

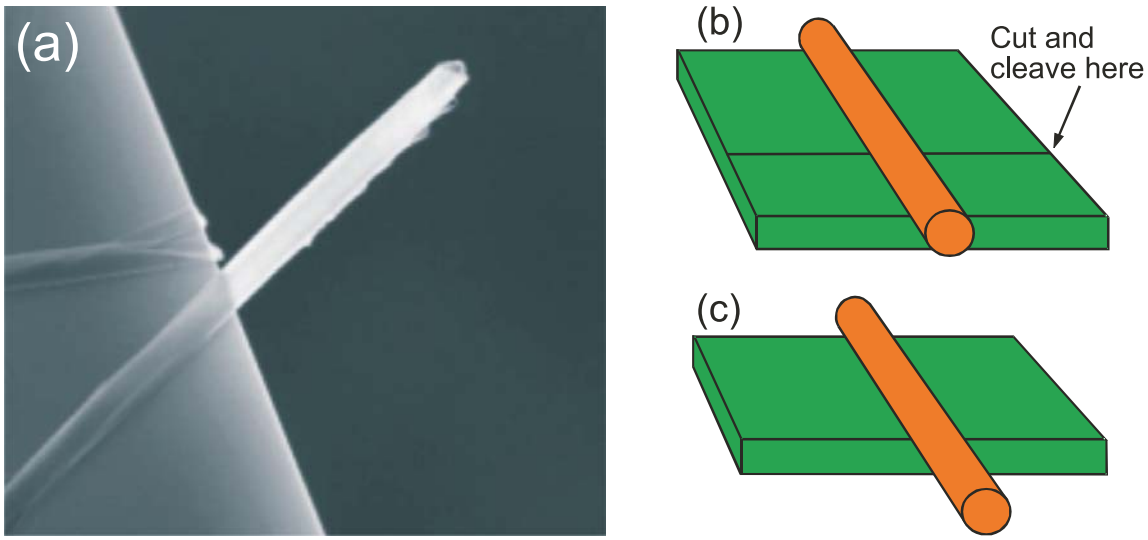

Figure 4: *(a) Completely free-standing nanotube. (b), (c) Schematic illustration of the fabrication of the nanotube.*

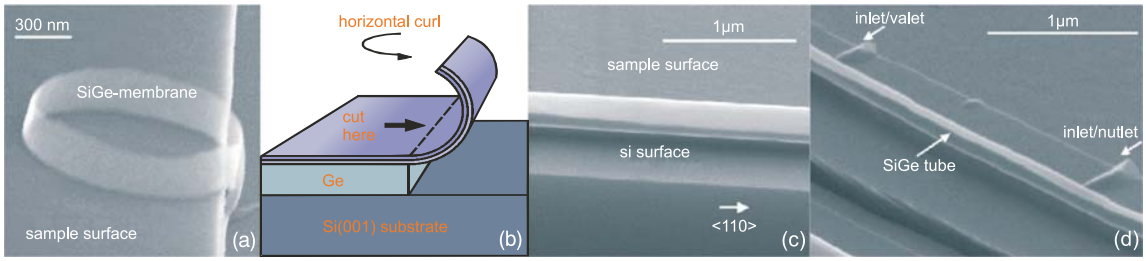

Figure 5: *(a) Ring-like vertical membrane based on a strained bilayer SiGe/Si system. (b) Schematic illustration of the formation process of the free-standing membrane. (c) Nanopipeline based on a folded back SiGe layer (method I). (d) Tube from semiconductor/metal hybrid layer system.*

up over 6 μm, again performing about 30 rotations. Our results demonstrate that the inner to outer diameter ratio can be tuned over a wide range. Whereas the nanotube in Fig. 2 has a ratio of nearly 1, the nanotube in Fig. 3 exhibits a ratio of only 0.125. This special design freedom makes the nanotubes ideal candidates for fundamental investigations as well as for possible applications.

An entirely free-standing nanotubes is presented in Fig. 4(a). The sample was cleaved perpendicular to the nanotube so that the tube extends over the cleaved edge (see Fig. 4(b) and (c)).

The technique introduced here is not restricted to III-V semiconductors nor to free-standing nanotubes. Other nanometer-size objects can be produced such as ultra-thin vertical membranes or helical coils.

Figure 5(a) shows a ring-like free-standing membrane formed out of a strained SiGe layer structure. The formation of the membrane follows a two step procedure (see Fig. 5(b)). In the first step the bilayer bends up perpendicularly to the surface. In a second step the bilayer starts to curl horizontally giving rise to the ring-like membrane in Fig. 5(a).

Figure 5(c) shows a nanotube from a layer structure consisting of a semiconductor layer, an oxide and a metal layer. On top of a Ge sacrificial layer a SiGe layer sequence was grown, starting with a Ge content of 70% and ending with a pure Si layer. The Si layer was oxidized and Ti was finally deposited on top of the structure. After selective etching a nanotube formed on the surface – integrating different materials.

The object shown in Fig. 5(d) represents a Si-based nanopipeline formed after method I. A layer with 40% average Ge concentration was grown on top of a 70 nm thick Ge sacrificial buffer layer. Creases formed perpendicular to the main tube, showing potential for inlet and outlet channels in a more complex nanopipeline system.

In conclusion, the release of semiconductor layers from their substrate offers a new route to form well-defined and well-positioned nanometer-sized objects on substrate surfaces. We have applied this technique to created nanotubes with different sizes and geometries and out of different material systems. Some of the tubes performed 30 rotations on the surface. Other objects like ultra-thin ring-like membranes and nanopipeline systems have been presented.

Electrical magneto-chiral anisotropy

G.L.J.A. Rikken, V. Krstic, S. Roth, and P. Wyder

Many physical systems are chiral, i.e., can exist in two forms that are each others' mirror image. Recently, a new polarization-independent optical effect was discovered in chiral media; magneto-chiral anisotropy (MCHA), which corresponds to an extra term in the dielectric constant of a chiral medium which is proportional to $\boldsymbol{k}\cdot\boldsymbol{B}$, where $\mathbf{k}$ is the wavevector of the light and $\boldsymbol{B}$ is the external magnetic field.

An electrical conductor can also be chiral; the material may crystallize in a chiral space group, like tellurium or β-manganese or be composed of chiral subunits like chiral molecules. Even if the material itself is non-chiral, it may still be formed into a chiral shape, like a helix. In all these cases, the conductor can exist in two forms, each of which is the mirror image of the other and which we call right (D) or left (L) handed.

In some chiral conductors, spin-polarized electronic transport has been studied and effects similar to natural circular dichroism in optical absorption have been observed. However, spin-polarization is not synonymous with chirality, as it is odd under time-reversal and even under parity-reversal. Only particles having a non-zero drift velocity *and* a longitudinal angular momentum are chiral. As charged particles in a magnetic field acquire angular momentum due to their cyclotron motion, charge carriers moving parallel to the magnetic field form a chiral system. The symmetry arguments used for the existence of optical MCHA may also be applied to the case of electrical transport, and the question comes to mind if an analogous effect exists in chiral conductors.

Onsager showed that for a generalized transport coefficient σ_{ij} (e.g., the electrical conductivity tensor), close to thermodynamic equilibrium one can write

$$\sigma_{ij} = \int_{-\infty}^{0} < y_i(0)\, y_j(t) > \mathrm{d}t = \sigma_{ji}^{\dagger}, \qquad (1)$$

where † denotes time-reversal and the y_i denote microscopic parameters describing the system. If y_i and y_j have the same time-reversal symmetry, one finds $\sigma_{ij}(\boldsymbol{B}) = \sigma_{ji}(-\boldsymbol{B})$. This is equivalent to the statement that any two-terminal resistance can only have an even magnetic field dependence. The frequently employed term 'linear magnetoresistance' refers in fact always to a magnetic field dependence where R varies linearly with B for large B, but which is still even in B and depends only on its magnitude. In chiral systems, symmetry allows all microscopic properties to have an odd dependence on the wavevector $\boldsymbol{k}$ of the moving particles. Equation (1) then gives $\sigma_{ij}(\boldsymbol{k},\boldsymbol{B}) = \sigma_{ji}(-\boldsymbol{k},-\boldsymbol{B})$. More specifically we find

$$\sigma_{ij}(\boldsymbol{k}\cdot\boldsymbol{B}) = \sigma_{ji}(-\boldsymbol{k}\cdot-\boldsymbol{B}) = \sigma_{ji}(\boldsymbol{k}\cdot\boldsymbol{B}), \qquad (2)$$

and so there are no time-reversal symmetry objections against a linear dependence of σ_{ii}, and therefore of any two-terminal resistance, on $\boldsymbol{k}\cdot\boldsymbol{B}$. As $\langle\boldsymbol{k}\rangle \propto \boldsymbol{I}$, the electrical current, we conjecture that the two-terminal electrical resistance of a chiral conductor subject to a magnetic field $\boldsymbol{B}$ is of the form, omitting higher order terms in $\boldsymbol{I}$ and $\boldsymbol{B}$ for simplicity,

$$R^{\mathrm{D/L}}(\boldsymbol{I},\boldsymbol{B}) = R_0\left\{1+\beta B^2+\chi^{\mathrm{D/L}}(\boldsymbol{I}\cdot\boldsymbol{B})\right\}, \qquad (3)$$

where parity reversal symmetry requires that $\chi^{\mathrm{D}} = -\chi^{\mathrm{L}}$. Therefore such a $\boldsymbol{I}\cdot\boldsymbol{B}$ term can only exist for chiral conductors. The parameter β describes the normal magnetoresistance, that is allowed in all conductors. We call the effect corresponding to the linear magnetic field dependence in Eq. (3) electrical magneto-chiral anisotropy (EMCHA), in direct analogy to the optical case. The existence of this effect is the direct consequence of the simultaneous breaking of time-reversal symmetry by a magnetic

field and of parity by chirality and is therefore fundamental and universal. Several microscopic mechanisms of EMCHA can be imagined.

In a chiral medium, scatterers like crystal defects, phonons or other charge carriers will in general be chiral. In a longitudinal magnetic field, the scattering probabilities of the chiral charge carriers will be dependent on the relative handedness of these carriers and the scatterers. This will lead to a magnetic field dependence of the carrier scattering rate in a chiral conductor, and therefore lead to a change of its electrical resistance. Such a dependence has been calculated for the scattering of free electrons by chiral molecules in a magnetic field.

We have experimentally studied the chiral scattering mechanism as a source of EMCHA by measuring the two-terminal resistance of straight bismuth wires containing screw dislocations due to a torsional deformation. These dislocations will act as chiral scattering centers. The two-terminal magneto-chiral anisotropy of these distorted wires was experimentally determined as $\Delta R(I, B_{\rm ext}) \equiv R(I, B_{\rm ext}) - R(-I, B_{\rm ext})$ by means of standard phase-sensitive detection techniques.

Figure 6 shows a typical result for the magneto-chiral anisotropy of wires subjected to a L and to a D distortion. Clear EMCHA is observed, of opposite sign for the opposite handedness of torsion. Also shown is that the same L wire no longer shows EMCHA after it has been annealed close to its melting point. After this treatment, the zero-field resistance has returned to its value before distortion to within 1%, which proves that most of the screw dislocations have disappeared.

Consequently, the EMCHA must vanish, in agreement with our observation. For other wires investigated, the magnitude of the observed effect differed from that in Fig. 6 by up to an order of magnitude. However the sign of the magneto-chiral anisotropy always corresponded to the handedness of the distortion. This proves that scattering of charge carriers by chiral objects causes EMCHA.

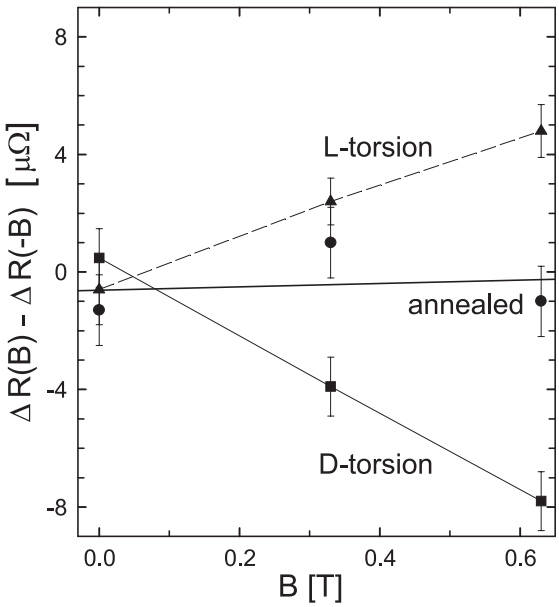

Figure 6: *Two-terminal magneto-chiral resistance anisotropy difference* $\Delta R(I, B_{ext}) - \Delta R(I, -B_{ext})$ *of D and L distorted bismuth wires with a length of 10 mm, a diameter of 0.5 mm, and I = 0.2 A, at 77 K. Also shown is the behavior of the L wire after annealing. Typical zero-field resistance of the wires is 20 m*Ω.

The second microscopic mechanism is based on the magnetic self-field. In general, a current carrying chiral conductor will posses a magnetization, the sign of which depends on the direction of the current and the handedness of the conductor. For a non-chiral material, the resistivity is given by $\rho(B) = \rho_0 \left\{1 + \beta B^2\right\}$. A D- or L-helix made of this material, carrying a current I, will generate an axial magnetic field at the position of the charge carriers $B_{\rm a} = \alpha^{\rm D/L} I$, where $\alpha^{\rm D/L}$ depends on the geometry of the helix, and $\alpha^{\rm D} = -\alpha^{\rm L}$.

If an external field $B_{\rm ext}$ is applied parallel to the helix axis, the charge carriers in the conductor feel $B_{\rm ext} + B_{\rm a}$. The resistance of such a helix is then given by (neglecting higher order terms)

$$R^{\mathrm{D/L}}(I, B_{\mathrm{ext}}) = R_{\mathrm{o}}\{1 + \beta B_{\mathrm{ext}}^2 + 2\alpha^{\mathrm{D/L}} \beta I B_{\mathrm{ext}} + O(I^2)\}. \quad (4)$$

So, although the material resistivity is an even function of the total magnetic field, for the resistance of a chiral conductor, due to the self-field, a term linear in the external magnetic field and the current exists. We have used bismuth helices to study experimentally this self-field effect as source for EMCHA. Figure 7 shows the magneto-chiral anisotropy ΔR for a D- and a L-helix of the same dimensions, as a function of magnetic field, at 77 K. Clearly a linear magnetoresistance is found, and of opposite slopes for the opposite handedness. Also shown are the theoretical predictions based on Eq. (4) and the calculated α and measured β values.

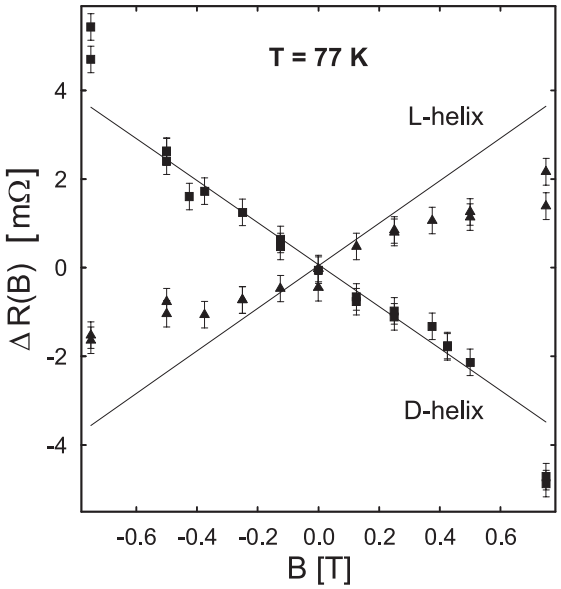

Figure 7: *Two-terminal magneto-chiral resistance anisotropy $\Delta R(I, B_{ext})$ of D (squares) and L (triangles) bismuth helices (7 turns, 8 mm diameter and 0.8 mm pitch) with I = 0.2 A, as a function of the external magnetic field B_{ext}, at 77 K. The solid lines are the predictions based on Eq. (4). Typical zero-field resistance of the helices is 0.2 Ω.*

Our experimental findings on macroscopic chiral conductors therefore quantitatively verify the self-field mechanism as source for EMCHA in electronic transport. The self-field effect will be operative at all length scales and will therefore induce EMCHA in all chiral conductors. Equation (3), should also apply to molecular chiral conductors. We have therefore also studied magnetotransport in metallic single-wall carbon nanotubes (SWCNT). We have indeed observed EMCHA for these conductors (Fig. 8). As we have no control over the handedness of SWCNT, the sign of the effect is arbitrary for any given SWCNT.

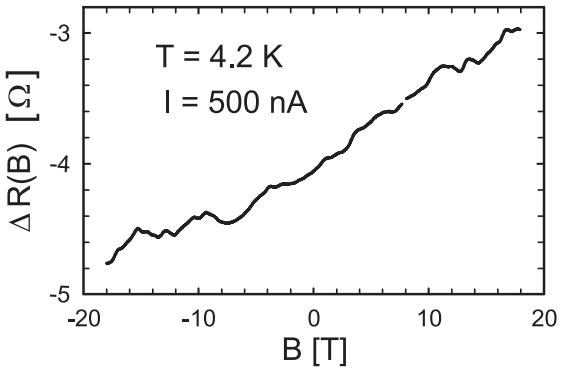

Figure 8: *Two-terminal magneto-chiral resistance anisotropy $\Delta R(I, B_{ext})$ of a SWCNT at 4.2 K. Typical zero-field resistance is about 7 kΩ.*

The statistics of the observed signs is in agreement with the natural abundance of left and right handed, and a chiral SWCNT. We have performed quantum transport calculations using the simplest possible model, namely a free electron on a helix in a magnetic field to model magnetotransport in SWCNT. This model can be solved analytically and we find that for both ballistic and diffusive helical conductors, EMCHA occurs in their two-terminal resistance.

Our experimental results confirm the validity of our conjecture of Eq. (3) and prove the existence of electrical magneto-chiral anisotropy in chiral conductors, ranging from molecules to macroscopic objects. One may also expect MCHA in other transport phenomena involving the movement of charge in chiral media. In particular, in analogy with the recently reported enantioselective magneto-chiral photochemistry, one may expect that MCHA in electrochemistry in magnetic field can lead to enantioselectivity.

Suspension bridges from individual carbon nanotubes

K. Atkinson, J. Fraysse, G. Gu, G.-T. Kim, A. Minett, and S. Roth

Carbon nanotubes are unique 'molecules' and a variety of measurements can be carried out on one and the same individual tube: e.g., electrical transport, Raman scattering, scanning tunneling spectroscopy etc. In these experiments, the nanotubes are usually adsorbed onto solid substrates. Certainly the substrates have an influence on the properties of the tubes and therefore measurements on free standing tubes are highly desirable. In addition, if free standing tubes are available, the elastic and mechanical properties can be studied.

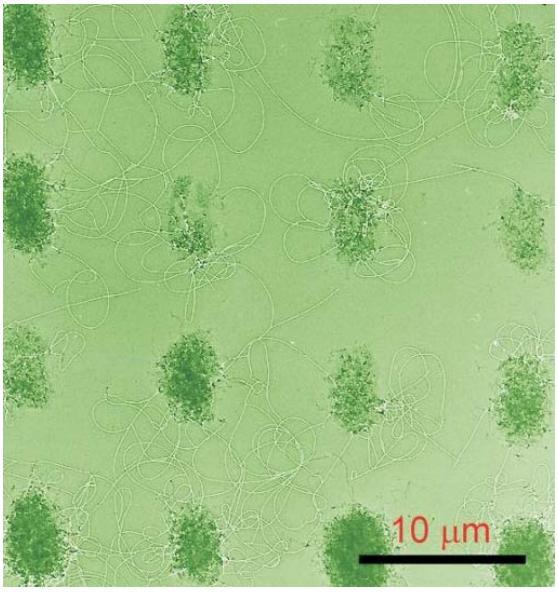

Figure 9: *TEM image showing CVD grown single-walled nanotubes between catalyst islands ($FeCl_3$, MoO_2Cl_2, block copolymer).*

One method of preparing free standing tubes is by growing them between catalyst islands. Figure 9 shows a transmission electron microscope image (TEM) of a thin (10 nm) silicon nitride membrane to which small droplets of catalyst solution ($FeCl_3$, MoO_2Cl_2, block copolymer) have been added by microcontact printing. If such a sample is placed into an oven and acetylene is blown over it at some 900°C, nanotubes grow between the islands, and many of these tubes are free standing [G. Gu *et al.*, Advanced Functional Materials **11**, 295 (2001)].

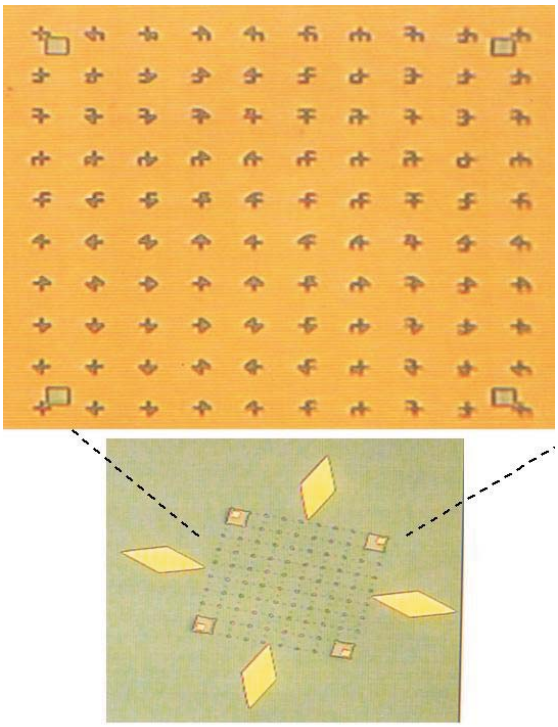

Figure 10: *Illustration of how the co-ordinate marker system appears on a substrate.*

An alternative method of preparation is based on electron beam lithography. Here one of the key problems is to relocate nanotubes in the electron microscope which have previously been selected by the atomic force microscope. To this end we have developed a marker system (Fig. 10) where cartesian coordinates are coded in some sort of sino-korean characters [G.T. Kim *et al.*, Applied Physics Letters **79**, 3497 (2001)].

The device shown in Fig. 11 has been obtained in the following manner: First, a set of markers was e-beam lithographed onto an oxide layer of a silicon chip, then a layer of photoresin was spun onto the surface. Nanotubes were then deposited at random and covered with a

second layer of photoresin. A suitable nanotube was selected with the atomic force microscope (AFM), and was then relocated with the aid of the markers by the electron beam machine. Holes were dug into the photoresin by hitting it with the electron beam and dissolving the illuminated parts. The holes were then filled by evaporating metal into them, and finally the remainder of the photoresin was removed [G.-T. Kim *et al.*, Applied Physics Letters (in print) 2002].

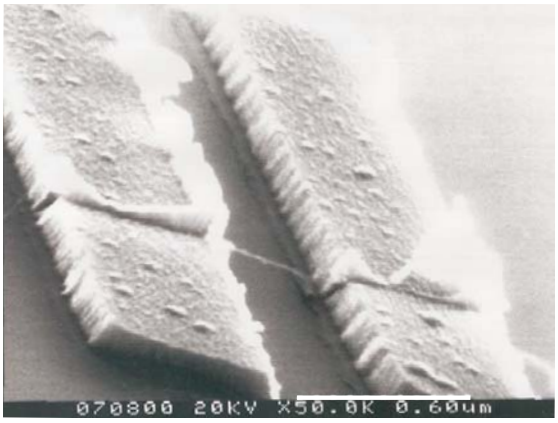

Figure 11: *SEM image of a suspended single-walled carbon nanotube between two metal contacts. Scale bar is 0.6 μm.*

The trench between the metal blocks in Fig. 11 is about 300 nm wide. If a Raman microscope is focused onto the 'nanotube suspension bridge', the Raman modes of the free standing tube can be studied; and the transport properties can be investigated by connecting the metal blocks to bond pads as is standard in semiconductor microtechnology. The trench is wide enough to hover along with the tip of an atomic force microscope, and from the force needed to strain the tube, the elastic modulus can be determined. In our case we have obtained $Y = 0.5$ TPa for Young's Modulus, which is in good agreement with theoretical expectations and with experimental values published by other groups.

If we work with a conducting microscope tip, we can use it to inject electric charges onto the tube. From previous experiments on bucky paper [R. Baughman *et al.*, Science **284**, 1340 (1999)] we know that the electrically charged tube will stretch (it will behave like an electromechanical actuator or an 'artificial muscle'). The charged tube will be electrostatically attracted by the countercharge at the (degenerately doped) silicon substrate and if a square wave potential is applied to the tube, a strain signal is picked up by the atomic force microscope, as shown in Fig. 12.

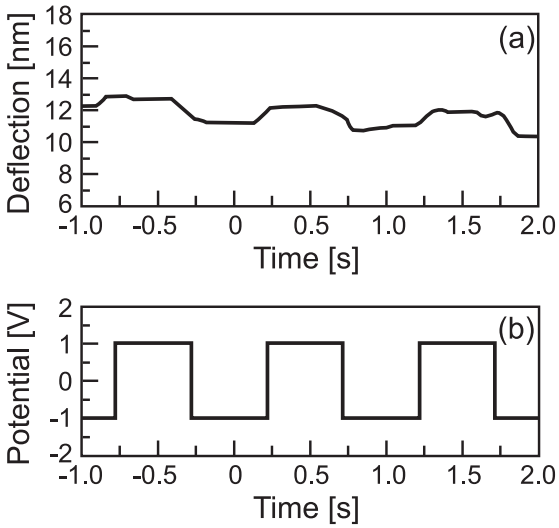

Figure 12: *AFM cantilever deflection (a) as a function of applied potential (b) versus time [G. Gu et al., unpublished data].*

Consequently we have a demonstrator for a nanoactuator and we expect that these nanomechanical investigations will lay the foundations for nanovalves and nanopumps in nanofluidic devices integrated onto silicon chips ('chemical laboratory on a chip').

Chemical modification of carbon nanotubes: from single molecule chemistry to single-electron transistors

S. Kooi, J. Cui, Y. Fan, U. Schlecht, R. Sordan, M. Burghard, and K. Kern

Controlled chemical modification of carbon nanotubes is required for applications that are based on the specific interaction of the tubes with other molecules or functional surfaces. These applications include chemical sensors in the gas or liquid phase, mechanically reinforced composite materials, atomic force microscopy tips of tailored chemical sensitivity, as well as electrical contacting of biological systems such as nerve cells. The chemistry of carbon nanotubes, however, is far less developed than the chemistry of their small counterparts, the fullerenes. Up to now chemical modifications were performed only on bulk nanotube material, and hardly allow control over the functionalization degree.

Electrochemical modification of individual carbon nanotubes. We were able to demonstrate that individual single-walled carbon nanotubes (SWCNTs) can be controllably modified via an approach that combines nanolithography and electrochemistry. In this way it is possible to separately study the effect of chemical modification on the electronic properties of both metallic and semiconducting SWCNTs. Moreover, electrochemical functionalization is well-suited to alter the nanotubes since the extent of reaction can be directly controlled via the magnitude and duration of the applied potential.

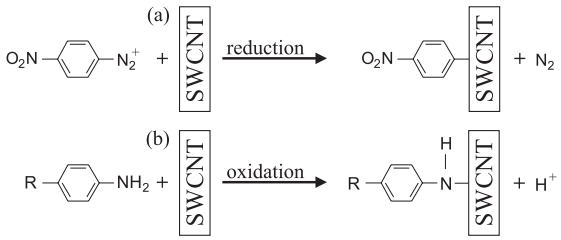

Figure 13: *Electrochemical modification of carbon nanotubes based on reductive (a) or oxidative (b) coupling of substituted phenyl groups.*

Two different coupling schemes were established for SWCNTs, working under either reductive or oxidative conditions (Fig. 13). In the reductive coupling, schematically presented in Fig 13(a), electron transfer takes place from the SWCNT to an aromatic diazonium salt in the electrolyte solution. As a result, a phenyl radical is created that can form a covalent bond to the carbon lattice of the tube, presumably at a defect site. In the case of oxidative coupling, shown in Fig 13(b), an aromatic amine is used to produce a radical cation as reactive agent at the SWCNT surface.

Especially the oxidative coupling reaction offers the possibility to functionalize the carbon nanotubes with acidic (R = –COOH) or basic (R = $–CH_2–NH_2$) groups attached to the benzene ring. These functional groups could be used for further attachment of functional building blocks, for example nanowires or nanocrystals, and therefore provide access to more complex device architectures.

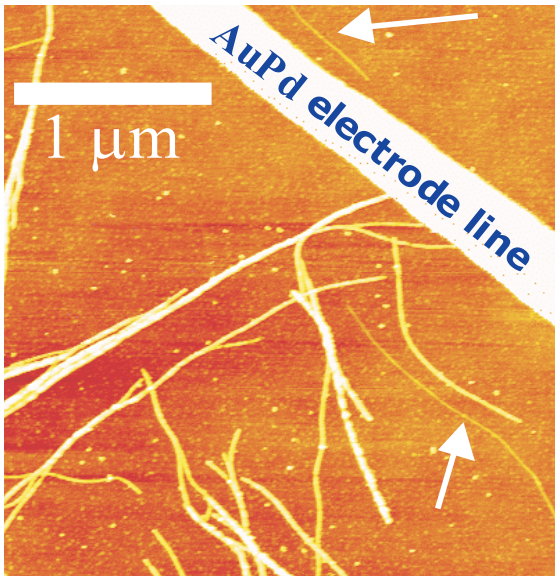

Figure 14: *Single-walled carbon nanotubes, contacted by an AuPd electrode, after oxidative coupling of a substituted aromatic amine.*

As a representative example, the atomic force microscopy (AFM) image in Fig. 14 depicts individual SWCNTs (and small SWCNT bundle) after oxidative coupling of 4-aminobenzylamine (R = –CH_2–NH_2 in the scheme above). The two SWCNTs marked by arrows remained unchanged since they are not electrically connected to the electrode line.

In contrast, the other contacted objects show a thickness increase of ≈ 10 nm, which is attributed to the formation of a layer consisting of polymerized phenyl radicals. Thinner layers can be deposited by shorter application of the potential, however, the coating is then harder to detect by AFM. It was found that the thickness of the coating correlates well with the time for which the fixed potential is applied.

Room temperature single-electron transistor (SET) by local chemical modification of SWCNTs. Individual SWCNTs, due to their small diameter of 1–2 nm, appear as suitable components of devices that operate on the basis of single-electron tunneling. In this context single-electron transistors are of special interest, e.g., for application as current standard.

Normally single-electron tunneling can be observed in individual SWCNTs only at low temperatures since the electrode distance is typically ≈ 100 nm, which is still accessible by conventional e-beam lithography. The fabrication of SWCNT-based SETs that operate at higher temperature therefore requires to define an ultra-small island within the tube. Such an island or quantum dot has been realized by creating a chemically modified SWCNT section of 10 nm length.

The method employed to fabricate the dot uses a V_2O_5 nanowire (10 nm in width) on top of the tube as a protection mask during the evaporation of an ultra-thin insulating layer (SiO). After dissolving the oxide nanowire, an uncovered tube section of the same length is obtained, which is then modified by a short O_2 plasma treatment. This last fabrication step is schematically displayed in Fig. 15. Importantly, the procedure includes deposition and etching steps that are compatible with conventional microelectronic fabrication techniques.

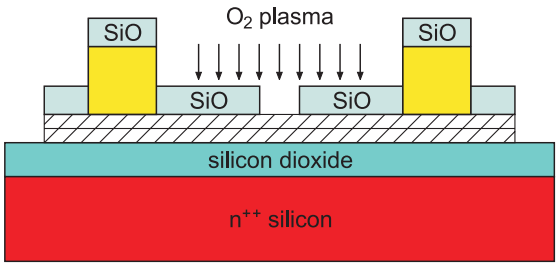

Figure 15: *Last step in the fabrication of the carbon nanotube single-electron transistor. Shown is the short oxygen plasma treatment used to chemically alter the unprotected SWCNT segment.*

The SWCNT device, which comprises the modified region as quantum dot and the unaltered tube parts as electrical leads, clearly shows single-electron tunneling features at liquid helium temperature, as revealed by the differential conductance peaks in Fig. 16 (black curve).

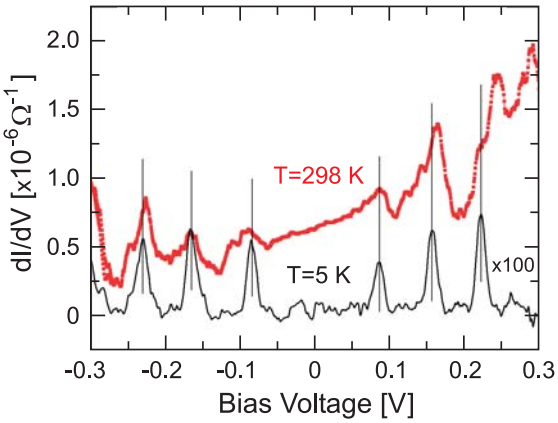

Figure 16: *Differential conductance of the locally modified carbon nanotube at 5 K (black curve) and at room temperature (red curve). The red curve is vertically shifted for clarity.*

These peaks are likely to reflect both Coulomb charging and the discrete energy levels due to electron confinement in the axial direction. Due to the small dot size, $\approx (2\times 2\times 10)$ nm, the dif-

ferential conductance peaks are still observable at room temperature (red curve in Fig. 16).

Moreover, since the device revealed conductance oscillations as a function of gate voltage at 298 K, it functions as a room temperature single-electron transistor. Although the nature of the chemical modification brought about by the plasma treatment and the origin of the two tunneling barriers required for de-coupling the dot from the rest of the tube are still not clarified, it is expected that better defined modification of the SWCNT (for example via electrochemical coupling of chemical groups) will allow to fabricate devices of tailored transport and high stability characteristics.

Tobacco Mosaic Virus as biological template for nanofabrication

A.M. Bittner, M. Knez, X.C. Wu, and K. Kern;
M. Sumser, C. Wege, and H. Jeske (Molecular Biology and Plant Virology, Stuttgart University)

The fabrication of nanostructures with well-defined chemical composition and low defect concentration is a prerequisite for the determination of their intrinsic physical properties. However, nanostructures are usually much larger than molecules and they do show defects and thus non-uniformity. Chemically spoken, a macroscopic sample of nanoobjects consists of a distribution of different molecular species. Directly connected with the size is the problem of uniform chemical composition. The best examples are probably proteins where a change in a single amino acid can make the molecule functional or non-functional. This leads to the idea of using biomolecules either as functional nanostructures or as templates for such.

In order to have a large number of chemical functions, but a well-defined and even stable structure we chose the Tobacco Mosaic Virus (TMV). It exclusively attacks tomato and tobacco plants and is completely harmless for mammals. The virus is produced and investigated in cooperation with the Molecular Biology and Plant Virology Department at Stuttgart University. TMV is a stable tube-like complex of a helical RNA strand and 2130 coat proteins (see Fig. 17). The proteins, too, are helically arranged; ca. 16.3 units build up one turn. The size is 300 nm with 18 nm outer and 4 nm inner diameter. The special shape makes this virus an interesting nanoobject, especially as template for reactions.

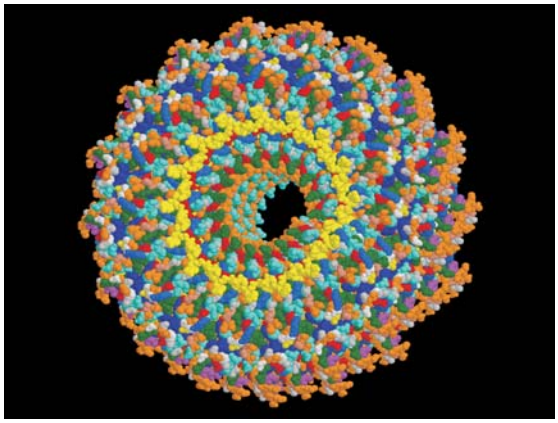

Figure 17: *Model of ca. 6.9 nm of the 300 nm long Tobacco Mosaic Virus (TMV). Yellow: helical RNA, containing the genome. In the helically arranged 49 coat proteins (three turns) each amino acid moiety is colored, reflecting the chemical complexity.*

On one hand, the molecule is so stable that it tolerates temperatures up to 90°C and pH-values from 3.5 to 9 and even several organic solvents such as ethanol or aqueous DMSO. On the other hand, the outer surface provides hy-

droxyl and carboxylate functional groups; in Fig. 17 the orange threonine moieties (hydroxyl groups) on the outer surface are obvious. The inner channel is quite similar, but in addition contains the RNA (yellow) and flexible loops of the protein that comprise threonine, but also the light blue glutamine with its primary amide group. This *chemical* heterogeneity on the nm scale is – in contrast to uniform inorganic nanotubes or wires – not usually investigated.

We found that the adsorption behavior of a TMV suspension depends strongly on the chemical properties of the outer surface, i.e., on the carboxylate and on the hydroxyl groups. This can be exploited by tuning the pH-value of a suspension to fit the substrate chemistry. Even covalent linkages to these groups are possible. The binding to standard surfaces (gold, graphite and mica, oxidized silicon wafers, glass) was investigated with different protocols such as acid treatment or binding to self-assembled monolayers with 'sticky' acid chloride terminal groups.

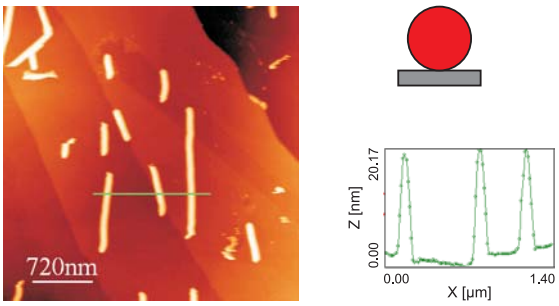

Figure 18: *Non-contact Scanning Force Image of TMV adsorbed on highly oriented pyrolytic graphite. A height profile (cut along the green line) shows 18 nm diameter.*

With scanning probe techniques (in air and in aqueous solution) a range of apparent heights from 10 nm to the maximum of 18 nm was found. Non-contact Scanning Force Microscopy turned out to be the optimal method for a direct comparison of apparent heights. The theoretical diameter / height of 18 nm is only encountered when surface-virus interactions are minimized, e.g., on the unreactive and hydrophobic graphite (see Fig. 18; note that many particles aggregate end-to-end, thus forming tubes longer than 300 nm).

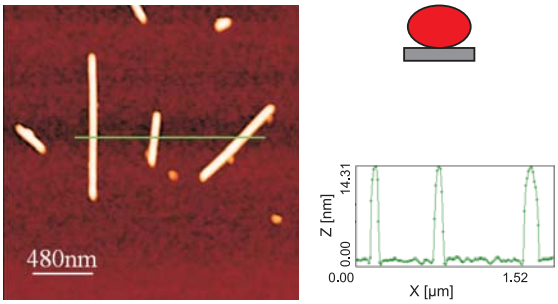

Figure 19: *Non-contact Scanning Force Image of TMV adsorbed on an oxidized silicon wafer. A height profile (cut along the green line) shows 14 nm height which is less than the diameter of the free virus.*

In contrast, lower apparent heights are always connected to hydrophilic interfaces or to covalent binding as in Fig. 19 on a hydrophilic (oxide-covered) silicon wafer. The lower height is due to stronger interaction, e.g., via hydrogen bonds to the surface, leading to a radial compression of the virus. In analogy to biological mechanisms such as dissociation of the protein to liberate the RNA in a plant cell, the flexibility of the rod depends on the chemistry of its surrounding, here of the surface.

In order to arrange the particles in regular arrays the adsorption protocols can easily be combined with MicroContact Printing. First experiments showed that the stability of TMV allows a transfer from a microstructured soft polymer stamp to a surface. A new transfer method was developed which relies on an only partially hydrophilic stamp that is completely covered by several layers of TMV. In this way large areas (several cm^2) can be structured in a fast, highly parallel way. Ideal substrates are hydrophilic (mica or silicon, see Fig. 19) and can thus strongly bind up to a monolayer of the virus.

Chemical modifications of TMV are not restricted to very mild conditions as for most biomaterials. We attained binding and reduction of palladium and gold ions with virus suspensions, verified by Transmission Electron Microscopy. The thus produced nanoscale metal clusters can act as catalysts, e.g., for the local electroless deposition of nickel. In detail, we first adsorbed Pd^{2+} from aqueous $PdCl_4^{2-}$. An important point was counteracting the hydrolysis of this complex by working at rather low pH-values and/or high chloride concentrations, conditions that may easily be detrimental to other biomolecules. After centrifugation we placed the TMV in a Ni^{2+}/ hypophosphite electroless deposition bath of roughly neutral pH, and in some cases heated to 50°C. Hypophosphite proved to be a reductand that did not affect the TMV structure. The samples were then investigated with Transmission Electron Microscopy. The majority of viruses appeared unchanged while about a quarter were filled with up to 6 clusters (black in Fig. 20(a), the single TMV of 300 nm length appears grey).

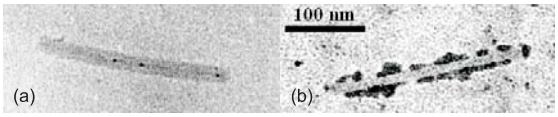

Figure 20: *Transmission Electron Micrographs (200 keV) of TMV on a carbon grid. (a) After treatment with $PdCl_4^{2-}$ and electroless deposition from $Ni^{2+} + H_2PO_2^-$; (b) after electroless deposition from $Ag^+ + HCHO$. Grey: virus, black: metal clusters.*

Surprisingly nearly all clusters were found *inside* the virus channel. Electron diffraction proved that these clusters contain nickel. A tentative interpretation is that the outermost surface of the coat proteins mainly exhibits alkane and alkanol chains, carboxylate and amides, while RNA and a *flexible* loop of the coat protein form the channel walls. Here amine groups of various chemical nature can interact with Pd^{2+} and bind it stronger than the other chemical groups. In this respect we mention that the channel – albeit narrow – should not prevent the diffusion of species; the hydrophilicity of the RNA and the protein loops should allow for a straightforward wetting of the channel by hydrophilic liquids.

When the ions are reduced and coalesce to Pd clusters, they can act as activation centers for the electroless deposition of metals like nickel, in fact forming Pd / Ni core / shell clusters. It is exiting that other protocols give different results, e.g., a selective coating of the outer surface can be achieved with silver and formaldehyde as shown in Fig. 20(b). Here the availability of strong coordination of Ag^+ by carboxylate on the outer surface may be kinetically favored.

These results point towards simple wet chemical syntheses of metal tubes and metal nanowires on biotemplates under full conservation of the biochemical functionality. Incorporation of TMV into existing structures can be achieved by chemical means, i.e., covalent linkages, offering a 'bottom-up' structuring. Alternatively, MicroContact Printing, a 'top-down' structuring method, offers a possibility for arranging (metalized) TMV in defined patterns. Both should allow contacting the virus electrically and thus to gain more insight in its electrical properties.

Transport

Transport is one of the basic phenomena in solid state science: transport of electricity, transport of heat, transport of matter. The following contributions are examples of our research on transport of ions in interfaces, on phonon and polariton transport in semiconductors, on electron transport in metals and on charge transport in coupled two-dimensional layers. Some further highlights of transport studies can be found in other chapters of this report, in particular under the headings of 'Strongly correlated materials' and 'Nanostructures'.

Saturation of electrical resistivity in metals

M. Calandra and O. Gunnarsson

In a metal, the electrical resistivity ρ, grows with the temperature T, due to the increased scattering of the electrons by phonons. Typically, $\rho(T) \sim T$ for large temperatures. For some metals with a very large ρ, however, the resistivity essentially saturates for large T. The resistivity is often described in a semiclassical picture, where an electron, on the average, travels a mean free path l before it is scattered. Typically, $l \gg d$, where d is the atomic separation. For the systems with resistivity saturation, however, l becomes comparable to d. Work in the 1970's suggested that saturation occurs universally when $l \sim d$. Later work has, however, found apparent exceptions, such as alkali-doped fullerenes and high-T_c cuprates. Intuitively, resistivity saturation seems natural. One might expect that at worst, an electron could be scattered at each atom, leading to $l \sim d$. Such a semiclassical picture, however, breaks down when $l \sim d$, and it is contradicted by the lack of saturation for the fullerenes.

Saturation is clearly observed for, e.g., A15 compounds, such as Nb_3Sb, where the resistivity saturates at about 0.10 to 0.15 mΩ cm. For the high-T_c cuprates and the fullerenes, the Ioffe-Regel condition predicts a larger saturation resistivity, about 0.7 and 1 mΩ cm, respectively. Experimentally, however, the resistivities reach much larger values; several mΩ cm for the cuprates and almost 20 mΩ cm for hole-doped fullerenes, suggesting a lack of saturation in these systems.

To discuss resistivity saturation, we use the f-sum rule

$$\frac{2}{\pi}\int_0^\infty \sigma(\omega)\,\mathrm{d}\omega \;=\; -\frac{1}{3}\frac{d^2 e^2}{\Omega}\,T_\mathrm{K}\,, \qquad (5)$$

where $\sigma(\omega)$ is the optical conductivity, d is the separation of the scattering centers, Ω is the volume of a unit cell and T_K is the the kinetic energy per unit cell. We assume that T is large enough that the Drude peak has been smeared out and that $\sigma(\omega)$ is a smooth function. The removal of the Drude peak may be due to any scattering mechanism, electron-phonon, electron-electron or disorder scattering. We furthermore assume that $\sigma(\omega) = 0$ for $\omega > W$, where W is the one-particle band width. This should be a good approximation, since $\omega > W$ would involve multiple electron-hole excitations and have a small weight. We can then write

$$\sigma(\omega = 0) = \frac{\gamma}{W}\int_0^\infty \sigma(\omega)\,\mathrm{d}\omega\,, \qquad (6)$$

where γ depends on the shape of $\sigma(\omega)$. We expect γ to be a bit larger than unity, and explicit calculations for models with electron-phonon or electron-electron scattering give values of the order two to four. Localization could lead to a γ

much smaller than unity and a resistivity much larger than predicted below (by $\rho = 1/\sigma(\omega = 0)$). Since, however, we consider large temperatures, localization should not occur.

We first consider non-interacting electrons in a band with the orbital degeneracy n at $T = 0$. Then we can write

$$T_{\mathrm{K}} = 2\mathrm{n}\int_{-W/2}^{\mu} \varepsilon N(\varepsilon)\,\mathrm{d}\varepsilon \equiv -2\mathrm{n}\alpha W\,,$$

where $N(\varepsilon)$ is the density of states per orbital and spin, μ is the chemical potential and α depends on the shape $N(\varepsilon)$ and the filling. For a half-filled semielliptical $N(\varepsilon)$ $\alpha \sim 0.1$. This result is relatively independent of the specific shape of $N(\varepsilon)$. We then obtain

$$\frac{1}{\rho} = \sigma(0) = \frac{\pi\,\mathrm{n}}{3}\,\alpha\gamma\,\frac{d^3}{\Omega}\,\frac{e^2}{\hbar d}\,. \qquad (7)$$

For a weakly correlated transition metal compound like Nb_3Sn, the Nb *4d* orbital plays the main role, and we use $\mathrm{n} = 5$. Considering the A15 lattice of Nb_3Sn, the resistivity should not exceed a value of about $0.14\,\mathrm{m}\Omega\,\mathrm{cm}$ [M. Calandra *et al.*, Physical Review Letters **26**, 266601-1 (2001)]. This value is shown by the horizontal line in Fig. 21 and it compares well with the experimental saturation resistivity of about $0.15\,\mathrm{m}\Omega\,\mathrm{cm}$ for Nb_3Sn. This resistivity corresponds to a mean free path of the order d.

We next consider the low T behavior, assuming an electron-phonon scattering mechanism (strength λ)

$$\rho(T) = 8\pi^2\,\frac{\lambda T k_{\mathrm{B}}}{\hbar\Omega_{\mathrm{pl}}^2}\,, \qquad (8)$$

where k_{B} is the Boltzmann constant. Ω_{pl} is the plasma frequency, which depends on the average Fermi velocity. Figure 21 shows the straight line corresponding to Eq. (8) as well as a calculation of the resistivity. The resistivity curve initially follows Eq. (8), describing how the amplitude of the Drude peak is gradually reduced, reducing $\sigma(\omega = 0)$ and increasing $\rho(T)$. When the two lines intersect, the Drude peak has been entirely lost. At roughly this T the rapid growth of $\rho(T)$ stops and saturation occurs. Nb_3Sn has a rather large λ and a very small Ω_{pl}, leading to very steep slope.

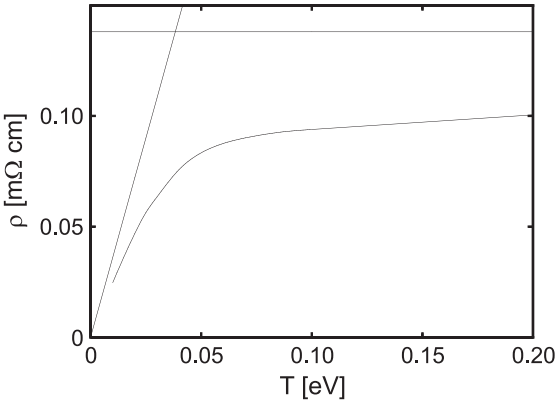

Figure 21: *Resistivity for a model Nb_3Sn. The horizontal line shows the saturation resistivity (Eq. (7)) and the linear in T resistivity (Eq. (8)). Saturation happens before these two lines intersect.*

As a result the curves intersect at a value of T which is experimentally accessible. For most metals, however, the slope of the low T curve is such that the intersection would happen well above T's that can be reached experimentally. Then no saturation is seen. Nb_3Sn has a rather large unit cell, leading to a complicated band structure with many forbidden crossings. This leads to rather flat bands, a small Ω_{pl} and a rapid increase of $\rho(T)$. This is in contrast to Nb, which has only one atom per unit cell and a substantially larger Ω_{pl}. For Nb signs of saturation are seen, but at a larger T and less pronounced than for Nb_3Sn.

We now consider a model of a strongly correlated system, appropriate for the cuprates. In these systems the transport properties should mainly be determined by the Cu–O antibonding band of Cu x^2-y^2 and O $2p$ character. Thus we consider one orbital per site and the orbital degeneracy $\mathrm{n} = 1$. We furthermore assume that the Coulomb interaction U between two electrons on the same site is so large that double occupancy of a site can be neglected. We therefore use a two-dimensional $t-J$ model for describing the system.

We first notice that if the model has one electron per site, hopping is completely suppressed by the Coulomb energy, and $T_K = 0$. Introducing doping (x holes per site), however, makes hopping possible. The probability that a given site is occupied is $(1-x)$. An electron can hop to a neighboring site only if this site is empty, the probability for which is about x. From this we obtain a crude estimate

$$T_K = -4\,t\,x(1-x)\,,$$

where four is the number of nearest neighbor and t is the hopping integral. Explicit calculations for the $t-J$ model show this result overestimates $|T_K|$ by about 15%. Insertion of this result (with the prefactor 3.4) in Eqs. (5, 6) gives

$$\rho(T) = \frac{0.35}{x(1-x)} \quad \mathrm{m\Omega\,cm}\,. \tag{9}$$

For small x, this result is much larger than the Ioffe-Regel resistivity ($0.7\,\mathrm{m\Omega\,cm}$). It is also much larger than the saturation resistivity $0.14\,\mathrm{m\Omega\,cm}$ derived above for a model of weakly correlated transition metal compounds. This is due to the strong reduction of the kinetic energy in the cuprates, due to strong correlation effects, in particular for small dopings.

Figure 22 compares the experimental resistivity for $La_{2-x}Sr_xCuO_4$ with the saturation resistivity deduced from the kinetic energy calculated in the $t-J$ model. For all values of x, the resistivity is smaller than the predicted saturation resistivity. Therefore, the experimental results do not demonstrate absence of saturation. Actually, for x = 0.04 and x = 0.07 the experimental data show signs of saturation, while for x = 0.15 and x = 0.34 one would have to study much higher (and experimentally unaccessible) T to demonstrate lack of saturation. We therefore conclude that the results for $La_{2-x}Sr_xCuO_4$ are consistent with resistivity saturation, although the saturation happens at much larger resistivities than predicted by the Ioffe-Regel condition.

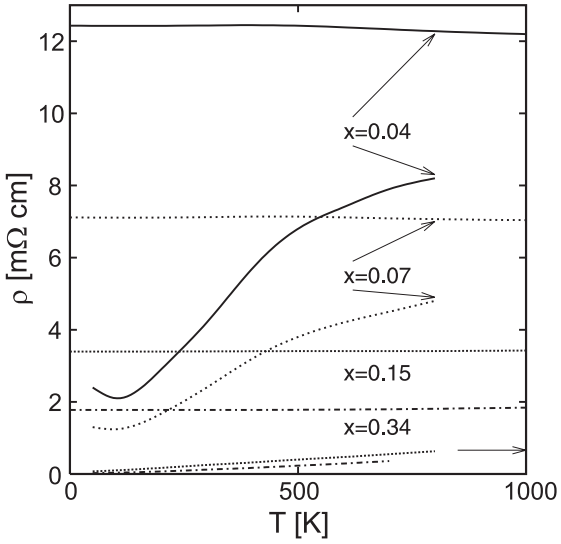

Figure 22: *The resistivity as a function of T for $La_{2-x}Sr_xCuO_4$ and the saturation resistivity according to the f-sum rule for x = 0.04 (full curve) x = 0.07 (broken curve) x = 0.15 (dotted curve) and x = 0.34 (dash-dotted curve). The horizontal arrow shows the saturation resistivity expected from the Ioffe-Regel condition. The figure illustrates that there are signs of saturation for small x at roughly the resistivities where saturation is expected. For larger x, much larger T would have to be considered to test whether there is saturation.*

We finally consider the alkali-doped fullerenes, A_3C_{60} (A = K, Rb). These systems have orientational disorder. Therefore, already at $T = 0$ the resistivity is comparable to the saturation resistivity estimated from Eq. (8). In these system the main scattering mechanism is believed to be due to intramolecular phonons, which couple to the level energies and create fluctuations in these energies. Due to the small band width, the fluctuations become comparable to the band width at temperatures that can be reached experimentally. The band width then grows with T, roughly as $\sqrt{a+bT}$, where a and b are material constants. The fluctuations reduce the kinetic energy, since two neighboring levels may have very different energies, which strongly suppresses hopping. A crude estimate shows that $T_K \sim c/\sqrt{a+bT}$, where c is a material constant. Inserting this in Eqs. (5, 6) gives

$$\rho(T) \sim \rho(T=0) + dT,$$

where d is a material constant. Indeed, quantum Monte-Carlo calculations for a model of these systems show a lack of saturation even for extremely large values of T [O. Gunnarsson *et al.*, Nature **405**, 1027 (2000)], as predicted above. We therefore expect a lack of saturation for the fullerenes, putting these systems in a different class than the high-T_c cuprates.

The fullerenes differ from systems of the type of Nb_3Sn in two respects. Firstly, in Nb_3Sn the phonons couple primarily to the hopping matrix elements. As a result, both T_K and W grow with T. These effects therefore tend to cancel to some extent (see Eqs. (5, 6)). Secondly, the temperature scale for these effects are much large for Nb_3Sn due to the larger band width, and the effects are therefore rather small at realistic T's, leading to a weak T dependence after saturation has occurred.

Negative friction between two-dimensional electron gases

S. Lok, S. Kraus, W. Dietsche, and K. v. Klitzing;
W. Wegscheider (TU München and Universität Regensburg)

Normally, friction between two bodies means that one of them accelerates the other one into the same direction as the first one is moving. Recent experiments, however, have shown that this is not necessarily so if one considers friction between two two-dimensional electron gases (2DEG) in GaAs/AlGaAs heterostructures exposed to a magnetic field.

In a frictional drag experiment between electronic layers, a drive current is passed through one layer and the resulting drag voltage along the second layer is measured (Fig. 23(a)). The distance between the layers is of the order of 10 to 100 nm. Normally, the frictional drag between the charges in the two layers is either caused by purely Coulombic interaction or by phonon exchange. The experimental structures are produced by molecular beam epitaxy. The particular difficulty of the frictional drag samples lies in the necessity to produce separate electric contacts to the two layers. The technique used at our institute is schematically shown in Fig. 23(b).

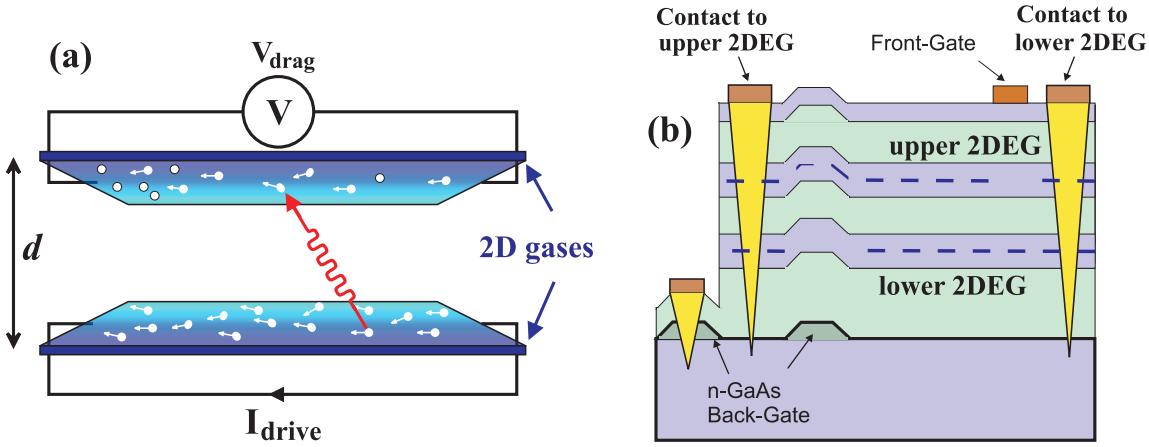

Figure 23: *(a) Principle of a drag experiment. The current passing through the bottom layer induces a drag voltage in the top layer by the exchange of excitations (red). (b) Two dimensional charge gases with distances down to 10 nm can be separately contacted by using field-effect gates from the top and the bottom.*

Contacts are made by conventional diffusion of doping material (yellow triangles in the figure). By using either the top or the buried gate contacts one can utilize the semiconductor field effect and ensure that eventually only one of the two layers is connected to the respective contact. Particularly important for this process is the ability to overgrow the prestructured substrates without degradation of the resulting layers.

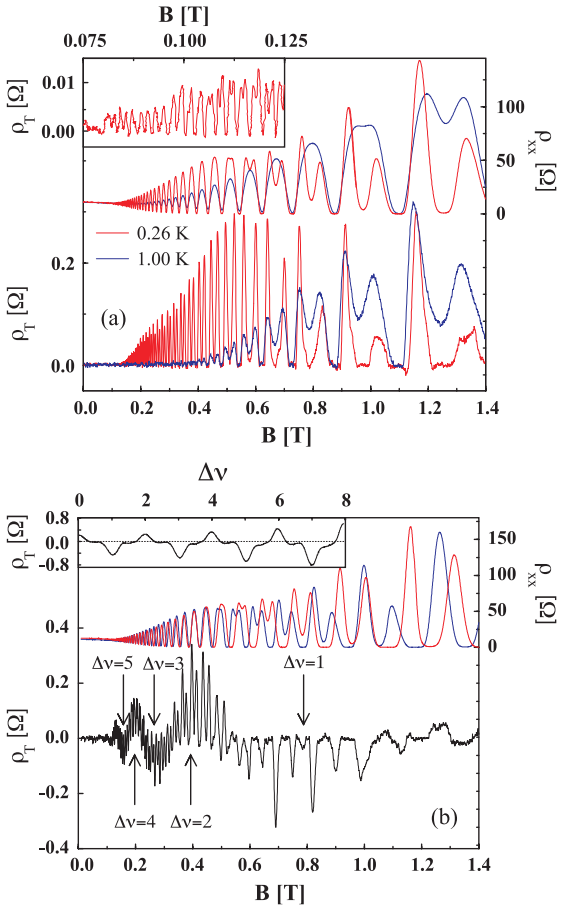

Figure 24: *(a) Top: Longitudinal resistances of the two 2d electron gases having equal densities. Bottom: Drag between the two layers. The periodicity is doubled until spin splitting becomes significant in the resistance curves at higher magnetic fields. The inset shows an enlargement of the small field region of the drag. (b) Similar as in (a) except that the densities in the two layers are different. The drag becomes now periodically negative. The anomalous behavior disappears as soon as the spin splitting is complete in higher fields. The inset shows the oscillating behavior of the drag on varying the density in one of the layers at B = 0.6 T.*

Frictional drag has been measured at a large number of different densities in the two layers. An examples for equal density is shown in Fig. 24(a). In the top part the resistivity along one of the 2DEGs is shown. The well-known Shubnikov-de Haas oscillations are observed. The drag voltage between the two layers is shown in the bottom. Compared to the resistance data the frequency of the drag oscillation has doubled. One can see that whenever the resistance of the two layer is at maximum, the drag vanishes. At these magnetic field values the Fermi energy lies in the center of the Landau levels in the two layers which are not yet spin split up to fields of about one Tesla. This vanishing of the drag is surprising because the phase space for the exchange of excitations should be largest at these fields. Actually, in the most naive theoretical description of drag one would expect maxima in the drag whenever the resistance of the single layers are maximal. Deviations of this simple assumptions had already been observed earlier and were attributed to screening in the 2DEGs which was said to overcompensate the effect of the large phase space for electron scattering in the center of the Landau levels.

In other experiments the drag was studied with different densities in the two layers. Results are shown in Fig. 24(b). In the top part one sees again the oscillating longitudinal resistances which are now out of phase due to the different electronic densities. The drag signal, bottom, shows a rather surprising behavior. There is still a rather rapid oscillation which is now, however, superimposed on another one which periodically reverses sign. In the magnetic field regions where the drag is negative, the electrons in the drag layer thus move opposite to the direction of the electrons in the drive layer.

It turns out that one can give a good phenomenological description of this very unusual behavior of the drag by assuming that the drag is proportional to the product of the differences in spin population in the two layers at the Fermi

energy. This formula describes the drag excellently both for equal and unequal densities, at least until the spin splitting becomes complete, in that case the negative drag disappears and the drag is proportional to the product of the densities as the standard theory had predicted.

Despite of the successful use of the phenomenological formula, the negative drag and its field dependence is far from being understood. The formula implies that the drag is dependent on the spin of the electrons in the two 2DEGs. There is, however, no theoretical mechanism which would lead to spin-dependence of the drag, let alone to have the sign of the drag reversed.

A straightforward interpretation which had been forwarded by another group is that electrons in one half of the Landau level acquire a hole like dispersion due to impurity effects. A hole-like dispersion would indeed explain the effects, but it should hold also at higher magnetic fields where the spin splitting is complete and where impurity effects would be the same. In the high field regime, however, the negative drag vanishes nearly completely.

More recently another theory has been published which considers the response to current fluctuations between the layers. This theory leads indeed to negative drag under certain conditions. The conditions are, however, not the ones where negative drag is observed.

More recently, the experimental studies at the institute concentrate on effects like the question if the two layers are equivalent with respect to exchanging the number of filled spin levels. They are not. Exchange of drag and drive layers leads, however, to identical results, as it should. Other little understood data concern the role of edges which are studied by gates covering the sample only partially. With these and other experiments it is hoped to solve the puzzle of the electrons moving into the wrong directions.

The cathodic polarization in solid oxide fuel cells investigated by means of microelectrodes

V. Brichzin, J. Fleig, H.-U. Habermeier, and J. Maier

Solid oxide fuel cells (SOFCs) are highly efficient energy conversion devices that transform chemical into electrical energy by an electrochemical reaction at high temperatures. Since the detour of involving thermal processes is avoided, electrochemical conversion is not restricted by Carnot's efficiency. Commercial SOFC prototype systems for electrical power generation are based on Y-doped ZrO_2 electrolytes, Sr-doped $LaMnO_3$ cathodes and Ni/ZrO_2 cermet anodes and are mostly operated at temperatures of about 850–1000°C. Numerous activities are going on to lower this operation temperature in order to gain more flexibility with respect to the materials choice. However, a temperature decrease results in an increase of the internal resistance of the SOFC. In particular the polarization due to the electrochemical oxygen reduction reaction at the cathode becomes very problematic at reduced temperatures. Many attempts have been made to clarify the polarization mechanism of the corresponding reaction

$$\frac{1}{2}O_2\,(\text{gas}) + 2e^-\,(\text{cathode}) \rightleftharpoons O^{2-}\,(\text{electrolyte}) \quad (10)$$

at the cathode side but the nature and location of the rate-determining step is still under discussion: On the one hand oxygen can be dissociatively adsorbed and possibly partly reduced on the surface of a Sr-doped $LaMnO_3$ (LMS)

grain and can diffuse along the LSM surface to the three-phase boundary LSM, air/electrolyte where it becomes fully reduced and gets incorporated into the yttria-doped zirconia (YSZ) (see Fig. 25). Many researchers favor this surface path for the oxygen reduction at LSM cathodes. On the other hand oxygen adsorbed on the surface of an LSM particle can also be incorporated as O^{2-} into the LSM. Under electrical load the oxygen ions would then diffuse through the LSM grain and be incorporated into the YSZ at the LSM/YSZ interface (bulk path, Fig. 25).

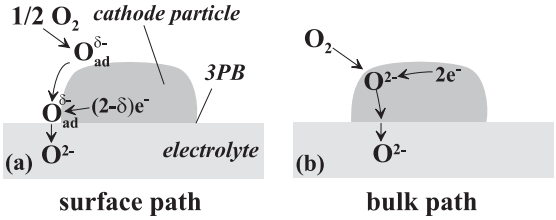

Figure 25: *Schematic illustration of the two possible oxygen incorporation paths.*

As the location of the rate-determining step of the cathodic reaction is reflected in the geometry dependence of the electrode resistance, experiments are desired in which the geometrical parameters (length of the three phase boundary, surface area, area of the electrode / electrolyte interface) are varied in a very controlled manner. This can been achieved by well-defined LSM microelectrodes: Pulsed Laser Deposition (PLD) has been used to grow thin films of A-site deficient LSM ($(La_{0.8}Sr_{0.2})_{0.92}MnO_3$) on 9.5 mole% Y_2O_3-doped ZrO_2 single crystals. Circular microelectrodes with diameters d_{me} ranging from ca. 20 μm to 200 μm and nominal thicknesses of 100–800 nm were patterned into the films by using photo-lithographic techniques and ion-beam etching. The circular microelectrodes were contacted with tungsten carbide tips (Fig. 26) and bias-dependent impedance spectra and I-V characteristics were measured between a microelectrode and an extended Pt counterelectrode on the back of the sample at ca. 800°C.

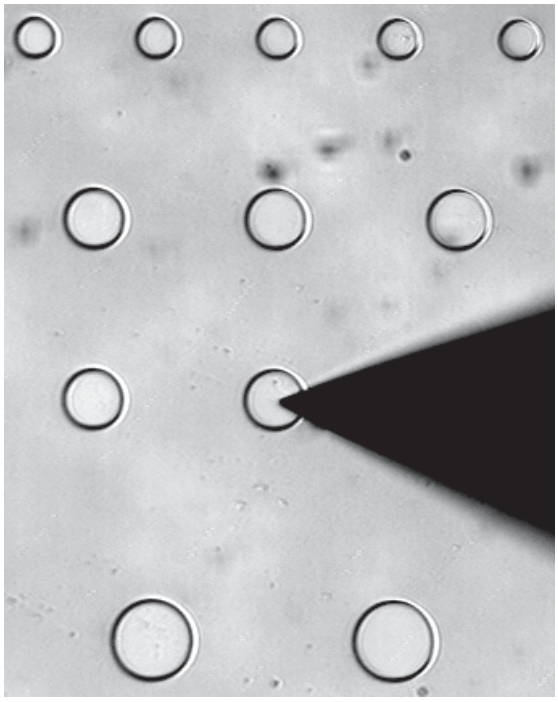

Figure 26: *Optical-microscope view at the sample's top. A tungsten-carbide tip of 2 µm nominal radius is contacting a 60 µm circular LSM microelectrode. The microelectrode diameters are 40 µm, 60 µm, and 80 µm, respectively.*

Several series of experiments with different electrode thicknesses consistently revealed that without bias as well as under cathodic bias ($U_{bias} < 0$) the resistance due to the electrochemical oxygen reduction reaction R_{el} is approximately proportional to d_{me}^{-2} and hence to the inverse electrode area (Fig. 27(a)). From this observation it can be concluded that the rate determining process directly involves the electrode area, i.e., occurs i) at the surface of the LSM or ii) in the bulk of the thin LSM electrodes or iii) at the LSM/YSZ interface. From thickness-dependent measurements further information with respect to the rate determining step can be expected since a predominant bulk path with transport of oxide ions through LSM being rate limiting should yield $R_{el} \propto t_{me}$ (t_{me} = microelectrode thickness). Hence a sample with 60 μm microelectrodes of two different thicknesses (100 nm and 250 nm) was examined.

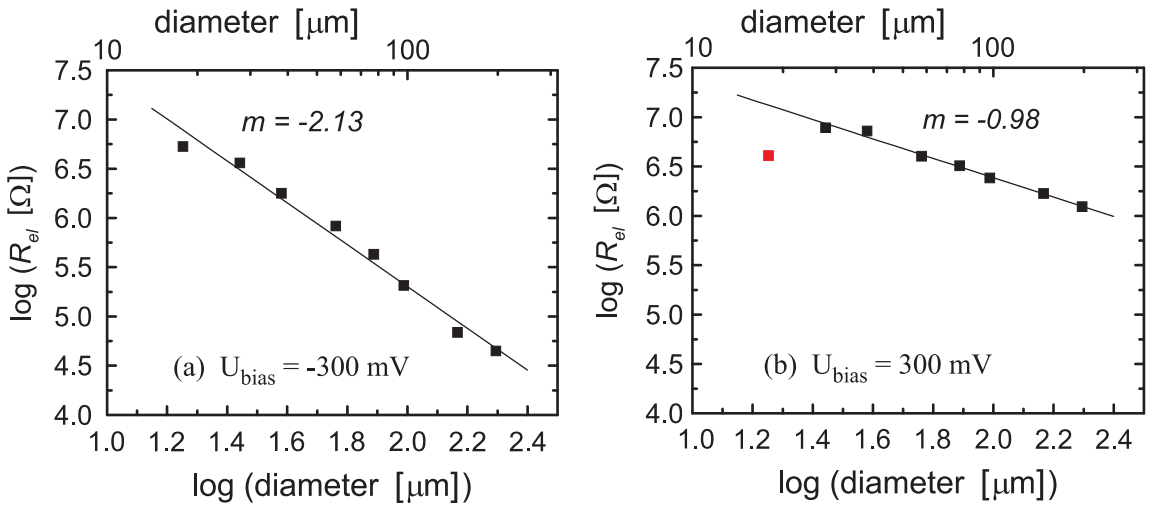

Figure 27: *Double-logarithmic plots of the electrode polarization resistance R_{el} versus the microelectrode diameter d_{me} (a) at a cathodic DC-bias of –300 mV. The slope m of the linear regression of the data is –2.13; (b) at an anodic DC-bias of +300 mV. The slope m of the linear regression (–0.98) is calculated without the first data point of the 20 μm microelectrode.*

The data extracted from measurements on 60 microelectrodes showed that the electrode polarization resistance R_{el} scales almost linearly with the thickness. This is a strong indication in favor of a bulk path determining the oxygen reduction rate with transport of oxide ions in LSM being the rate determining step.

However, going to the anodic regime, the slopes in the $\log(R_{\mathrm{el}}) - \log(d_{\mathrm{me}})$ plot change from about –2 to roughly –1 (Fig. 27(b)). This finding is supported by I-V measurements on LSM microelectrodes with diameters ranging from 30–80 μm: the differential resistance is proportional to the inverse microelectrode area in the cathodic regime and comes close to an inverse linear relationship with the three phase boundary (3PB) length in the anodic regime. It can therefore be deduced that in the anodic regime the surface path determines the overall current since all steps of the bulk path involve the area of the microelectrodes used. This mechanism change can be understood from the partial pressure dependence of the defect concentrations in ionic solids: according to Nernst's equation an anodic bias corresponds to an enhancement of the oxygen activity at the YSZ/LSM interface and hence further decreases the already low oxygen vacancy concentration in doped $LaMnO_3$. A strong anodic bias therefore completely blocks the bulk path and only a reaction via the surface path is possible.

It is finally important to note that both the bulk path and the surface path run in parallel and that it depends on the geometrical parameters how they are 'weighted', i.e., how much they contribute to the overall current. Other electrode aspect ratios, for example, can lead to a shift of the voltage at which the mechanism changes from the bulk to the surface path. In the case of the thin, broad microelectrodes considered here the current via the bulk path is predominant at $U_{\mathrm{bias}} = 0$ and in the cathodic regime. For an increasing three phase boundary length the weight of the surface path increases and in porous cathodes used in fuel cells a situation might result in which the bulk path is relevant only under significant cathodic bias while without bias the surface path is dominating. It is the great advantage of the microelectrode measurements presented here that they yield experimental data for both the surface and the bulk path. These experimental parameters are currently used in numerical simulations of the electrochemical performance of porous LSM cathodes.

Interfacial charge carrier chemistry in electroceramics

I: Separation of ionic and electronic conductivity contributions in bulk and space charge regions of $SrTiO_3$

X. Guo, J. Fleig, and J. Maier

Transport studies of $SrTiO_3$ are not only important with respect to the significance of this specific oxide (e.g., sensor, varistor, photoelectrode) but also, and more importantly, for its representative role as an electro-ceramic material. The same defect chemistry being characterized by oxygen vacancies as ionic and conduction electrons as well as holes as electronic carriers is found in other oxides of electrochemical relevance such as ZrO_2 (sensor, electrolyte) or CeO_2 (electrolyte, catalyst) which we also studied in this context. Of special interest and significance, but nevertheless largely terra incognita, is the defect chemistry at grain boundaries.

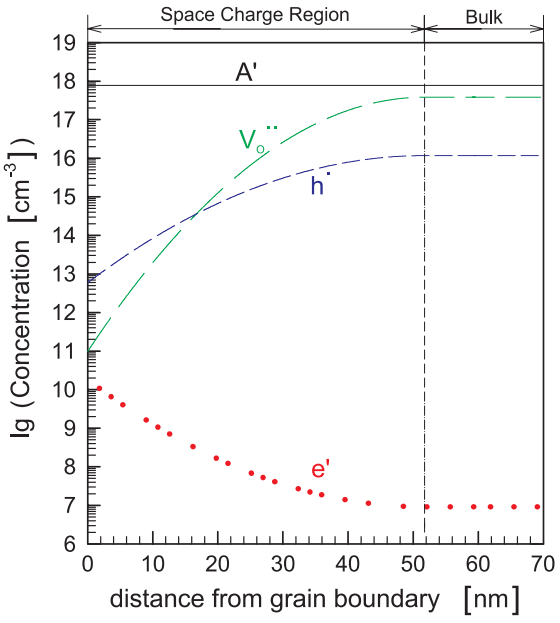

Figure 28: *Charge carrier defect chemistry at a Σ5-grain boundary of iron-doped $SrTiO_3$ ($A' = Fe^{3+}$ on Ti^{4+}-sites at a temperature of 750 K, at an oxygen partial pressure of 10^5 Pa, and a total iron content of $4.62 \cdot 10^{18}$ cm^{-3}) as obtained from the experiments and computations. The space charge potential is 0.5 eV.*

A typical result of our experimental and theoretical research on $SrTiO_3$ is given in Fig. 28. Qualitatively, it is also representative for other parameter sets and acceptor doped oxides. Figure 28 displays the situation near grain boundaries in acceptor doped oxides. Essentially owing to the dopant segregation a positive space charge potential is caused which leads to a depletion of the effectively positively charged carriers (electron holes $h^\bullet$, oxygen vacancies $V_O^{\bullet\bullet}$ as ionic carriers) and an accumulation of the effectively negatively charged carriers (excess electrons e'). Depending on the fact whether the dopant itself is mobile or not (this then depends on temperature), profiles of Gouy-Chapman type or of Mott-Schottky type are obtained, the latter leading to a deeper penetration of the field due to a lack of screening. A key problem is to separate ionic and electronic contributions to the conductivity.

We investigated $SrTiO_3$ bicrystals with electrodes attached parallel to the grain boundary. Under the conditions of interest the influence of the conduction electrons is negligible in Fe-doped $SrTiO_3$ (but see contribution II). By using electrodes which are reversible for ionic and electronic carriers ($YBa_2Cu_3O_{6+x}$ is most appropriate) as well as electrodes which are blocking for ions, we are able to separate ionic and electronic contributions. The detailed consideration of the current voltage characteristic allows to de-convolute n- and p-type (Wagner-Hebb technique).

Theoretically and methodically two points are worth being pronounced. (i) A thorough analysis allows us to extend the blocking electrode technique to materials in which internal ionization equilibria are active. (ii) The comparison

between dc- and ac-measurements and in particular the comparison between single and bicrystal experiments permit also the discrimination between electronic and ionic effects as far as the grain boundary contribution is concerned. In this way a full confirmation of the space charge picture was possible. We want to particularly stress the following:

(1) The local electronic conductivity (hole contribution) is significantly depressed near the core of the grain boundaries.

(2) Also the ionic conductivity is significantly lowered in the space charge region.

(3) The decrease of the ionic conductivity is much more severe, i.e., the ionic transport number decreases when the grain boundary is approached. This is due to the double charge of the oxygen vacancy which feels the electronic field much more strongly (quadratic in terms of relative concentration ratio).

II: Why is the electronic conductivity increased in nanocrystalline ceria?

S. Kim and J. Maier

Nanocrystalline ceria is the most intensively studied nanocrystalline mixed conductor (electrons and oxygen ions). All authors involved in this research agree in observing a pronounced increase in the conductivity of pure nanocrystalline CeO_2 compared to a microcrystalline material. The decrease of that value with increasing oxygen partial pressure leads to generally attributing this phenomenon to the contribution of conduction electrons rather than to ion conduction. Contradictory explanations are proposed in the literature. In what may be called the *neutral layer model*, the interfacial core (proper grain boundary) is treated as an electrically neutral layer in which the carrier contributions can be calculated as in the bulk, however, with modified formation energies leading to higher carrier densities. The alternative model is based on our *space charge considerations* and uses the fact that in space charge zones of positive electrical potential (as found in ZrO_2, CeO_2, $SrTiO_3$, see Fig. 29(a), adjacent to the interfacial core, being a part of the bulk, not only the positive charge carriers (oxygen vacancies, holes) are depleted in the boundary zones but also the negatively charged conduction electrons are enhanced.

While this effect is not of significance for, e.g., $SrTiO_3$ or even CeO_2 with a usual grain size of several micrometers (in particular if acceptor doped), in nanocrystalline CeO_2 with its comparatively high electronic bulk contribution and the enormous density of grain boundaries, the grain boundary can become electronically conducting and dominating the mean overall behavior.

How to distinguish between both mechanisms? In the neutral layer model an enhancement of both vacancy and electron concentration is proposed due to lower defect formation energy at the interface such that we expect both carriers to essentially flow along the core.

In the space charge model, however, only electrons flow along the boundaries whereas the ions are so severely depleted there that ion transport occurs only in the bulk. In addition, the ionic grain-to-grain transport is then interrupted by the depletion layers (see Fig. 29(b)). We tackled this problem by performing careful impedance measurements on nanocrystalline CeO_2 as a function of temperature, oxygen partial pressure and doping content. In addition,

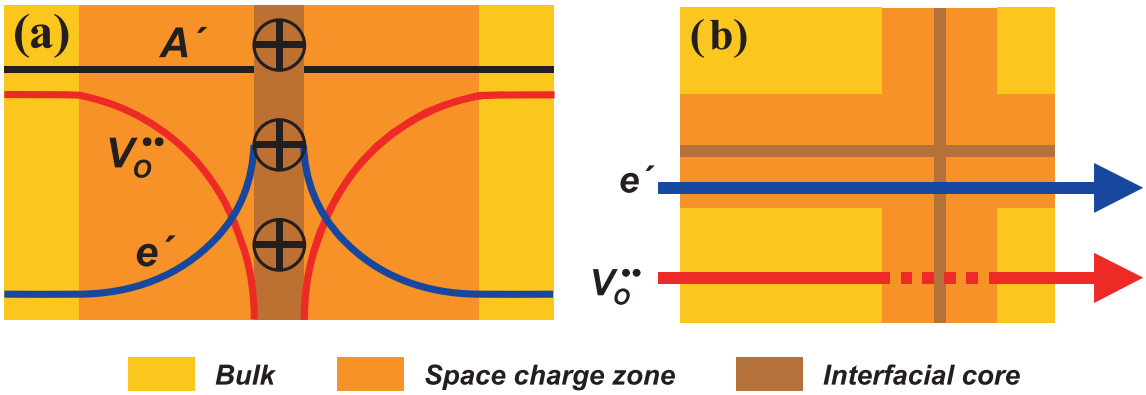

Figure 29: *(a) Concentration profile of the charge carriers in the space charge zone and (b) conduction path for each charge carrier according to the space charge model. A', $V_O^{\bullet\bullet}$ and e' denote the acceptor dopant, oxygen vacancy and electron, respectively.*

and this is the key to the solution, we were able to separately determine electronic and ionic contributions in the nanocrystalline samples by using electron-blocking ZrO_2 electrodes. We could show that the space charge picture explains – unlike the neutral layer model – all the experimental features in detail.

Let us only mention the most important points:

(1) In acceptor doped nanocrystalline CeO_2 with its low level of electronic conductivity in the bulk, only ionic conductivity is observed which indeed is blocked by grain boundaries manifesting itself in a low frequency semicircle in the impedance spectrum. Both temperature and partial pressure dependencies of the depletion effect are in agreement with a space charge potential of 300 mV, measured also for microcrystalline CeO_2.

(2) In nominally pure nanocrystalline CeO_2 the conductivity is of mixed (electronic and ionic contribution) nature and much larger than for macrocrystalline CeO_2. A second low frequency impedance arc is absent. Taking the 300 mV space charge potential and calculating the respective enhancement effect of the electronic carriers we obtain a quantitative agreement with the experimental conductivities as a function of partial pressure and temperature.

(3) Thus, we independently measured the effect of the ionic resistance due to the boundaries blocking the inter-grain transport according to ion depletion (1) as well as the increased conductance of short-circuiting boundaries owing to electron accumulation (2). Since both effects refer to the same space charge situation the parameters obtained must be consistent with each other in terms of local equilibrium. All this is impressively fulfilled with regard to both oxygen partial pressure dependence and temperature dependence.

(4) Beyond the mechanistic details, the result do not only show the significance of ionic space charge effects, they also highlight the importance of the *spacing of interfaces* as a practical ‘degree of freedom’ in tuning to individual transport properties.

Frequency and temperature dependence of the TO phonon-polariton decay in GaP

J. Kuhl; A.G. Stepanov (Institute of Spectroscopy, Troitsk, Russia);
J. Hebling (University of Pecs, Hungary)

The advent of reliable mode-locked laser systems routinely providing now optical pulses as short as 10 fs has made possible the development of powerful novel Raman spectroscopy techniques which allow direct observation of phonon generation and decay dynamics in the time domain. Applying such time-resolved Raman spectroscopy, we are able to explain the anomalous line shape of optic phonons in GaP which has puzzled people over several decades.

The transverse optic (TO) phonon Raman line of GaP reveals very unusual properties. Its width is much broader than that of the longitudinal optic (LO) phonon line and the optical phonon lines in many other III-V semiconductors, the line shape is highly asymmetric, and the linewidth reveals little change with temperature. The asymmetric shape has been attributed to frequency-dependent phonon damping caused by acoincidence of the TO phonon energy with the sum of the transverse acoustic (TA) and longitudinal acoustic (LA) phonon energy at the X-point, TA(X) + LA(X). Recently Widulle *et al.* have shown that the phonon line shape distinctly varies with isotope composition of the sample since a kink in the two-phonon density of states (DOS) in the vicinity of the TO phonon frequency is shifting with isotope substitution thus strongly influencing the 3rd-order anharmonic phonon decay. The deviations between measured phonon linewidths and the theoretical temperature dependence predicted for the 3rd-order anharmonic decay have been attributed to either four-phonon interactions or sample disorder.

Here, we present investigations of the TO phonon-polariton decay time $T_2(\omega, T)$ in GaP as a function of temperature T and polariton frequency ω measured directly in the time domain by impulsive stimulated Raman scattering (ISRS). $T_2(\omega, T)$ as a function of T changes drastically if ω is tuned from 361 to 365 cm^{-1}.

The experiment utilizes four-wave mixing with two pump pulses and one probe pulse at 810 nm with 25 fs duration (bandwidth 500 cm^{-1}, repetition rate 76 MHz). The diffracted probe is detected as a function of the delay $\Delta\tau$ between the pump and probe pulses, which is periodically varied by a 70 Hz rapid scan system. The signal is efficiently averaged and fed in a computer. The signal-to-noise ratio is $> 10^6$. The measurements are performed on a high-purity $\langle 110 \rangle$ oriented 200 μm thick GaP crystal mounted on the cold finger of a variable temperature cryostat.

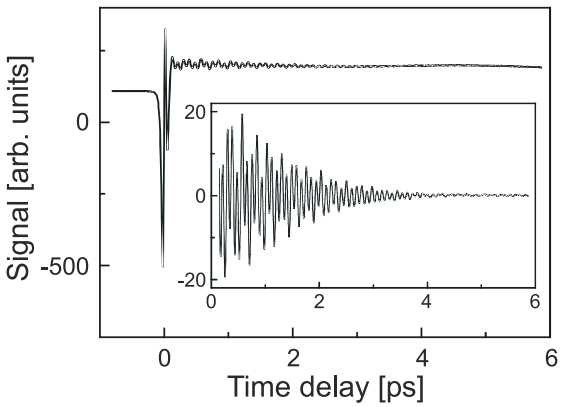

Figure 30: *Experimental signal for a $\langle 110 \rangle$ GaP crystal at room temperature as a function of $\Delta\tau$. The angle between the pump beams in free space is 14°. The inset shows the oscillatory part of the signal on an enhanced scale and for a baseline straightened by Fourier filtering.*

Coherent TO phonon-polaritons were excited by difference-frequency mixing of appropriately separated spectral components of the pump pulses. The polariton wave vector and

central frequency were tuned from $q = 16{,}000$ to $45{,}800\,\mathrm{cm}^{-1}$ and $\omega = 357.3$ to $365.1\,\mathrm{cm}^{-1}$, respectively, by varying the angle Θ between the pump pulses.

Figure 30 illustrates a typical signal measured as a function of $\Delta\tau$ at 300 K. The strong oscillation near $\Delta\tau = 0$ is due to the electronic Kerr non-linearity. The inset of Fig. 30 depicts the signal after rejection of this peak on an enhanced scale and for a baseline straightened by Fourier transform filtering. The decay time of the oscillation amplitude is equal to T_2.

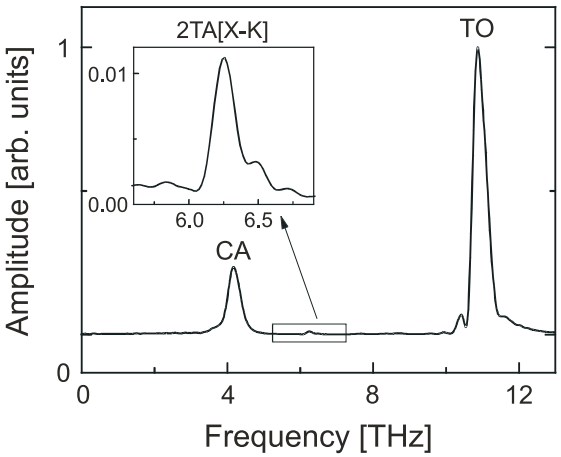

Figure 31: *Normalized Fourier power spectrum of the time domain data in the inset of Fig. 30. TO labels the phonon-polariton line. CA is a line attributed to a coherent artifact. The 2TA(X-K) line is due to a two-phonon state excited in a second order Raman process.*

The strong peak at 10.9 THz in the Fourier power spectrum of the time domain data (Fig. 31) presents the coherent TO phonon-polariton. Since the finite resolution of the Fourier spectrum inhibits accurate determination of the polariton mode frequency, we have first calculated the polariton wave vector q

$$q = (k_\mathrm{L}^2 + k_\mathrm{S}^2 - 2k_\mathrm{L}k_\mathrm{S}\cos\Theta)^{1/2} \qquad (11)$$

(k_L and k_S are the wave vectors of the two pump beams). The frequency was determined using the temperature dependent polariton dispersion in GaP. The peak at 4.1 THz is due to an artifact caused by interaction of the probe with pump pulses reflected from the backside of the sample. The weak line at 6.3 THz presents a two-phonon state excited by 2[rd]-order Raman scattering.

T_2 can be evaluated from our experimental data by fitting of the time-domain data (Fig. 30) after Fourier filtering of the CA line with exponentially decaying oscillatory functions. T_2 has been measured for several modes in the frequency range from 357 to $365\,\mathrm{cm}^{-1}$ at temperatures between 10 and 250 K. Figure 32 presents plots of the dephasing rate $\Gamma = (T_2)^{-1}$ measured at $q = 45{,}800\,\mathrm{cm}^{-1}$ (squares), $25{,}000\,\mathrm{cm}^{-1}$ (crosses) and $20{,}500\,\mathrm{cm}^{-1}$ (triangles) vs. temperature. The TO phonon polariton in the investigated frequency range can decay into a TA (upper branch) plus a LA phonon at the K point of the Brillouin zone. Slight tuning of ω near the TO phonon frequency leads to drastic changes of the temperature dependence of Γ.

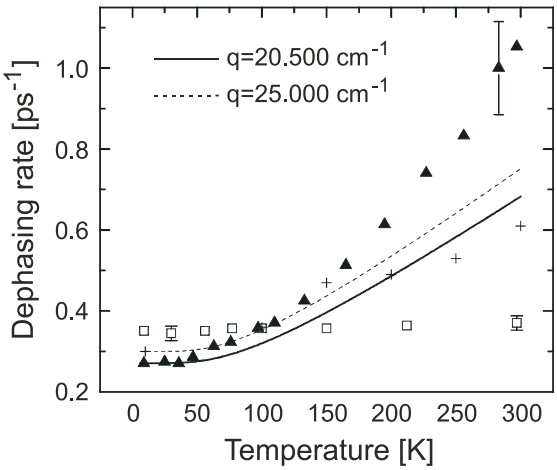

Figure 32: *Temperature dependence of the TO phonon-polariton dephasing rate in pure GaP at $q = 20{,}500\,cm^{-1}$ (triangles), $25{,}000\,cm^{-1}$ (crosses), and $45{,}800\,cm^{-1}$ (squares). The solid and dashed lines are fits using the usual expression for third order anharmonic decay (details are given in the text).*

The solid and dashed line in Fig. 32 represent theoretical curves for the modes at $20{,}500\,\mathrm{cm}^{-1}$ and $25{,}000\,\mathrm{cm}^{-1}$, respectively, obtained from the usual expression for the 3[rd]-order anharmonic decay of an optical phonon into two acoustic phonons:

$$\Gamma(\omega, T) = |V_3|^2 \rho(\omega)\,[1 + \mathrm{n}(\omega_1, T) + \mathrm{n}(\omega_2, T)], \qquad (12)$$

where $\Gamma(\omega, T)$ is the inverse lifetime of the initially excited optical phonon, $|V_3|$ is the effective 3rd-order anharmonic coupling constant, $\mathrm{n}(\omega_{1,2}, T) = [\exp(h\omega_{1,2}/k_\mathrm{B}T - 1]^{-1}$ are the Bose-Einstein occupation numbers of the acoustic phonons with frequencies $\omega_{1,2}$ ($\omega = \omega_1 + \omega_2$), $\rho(\omega)$ is the two-phonon DOS at $\omega = \omega_1 + \omega_2$. The term $|V_3|^2 \cdot \rho(\omega)$ was used as a temperature independent fitting parameter. The experimental data for the $q = 20{,}500\,\mathrm{cm}^{-1}$ and the $25{,}000\,\mathrm{cm}^{-1}$ mode exhibit either a systematically higher ($20{,}500\,\mathrm{cm}^{-1}$) or lower ($25{,}500\,\mathrm{cm}^{-1}$) dephasing rate than calculated by Eq. (12).

Finally the decay time of the polariton mode at $q = 45{,}800\,\mathrm{cm}^{-1}$ exhibits no significant temperature dependence between 4 K and 300 K in accordance with previous Raman linewidth data $\sigma_\omega = (\pi \cdot T_2)^{-1}$. This extraordinary behavior can be attributed to a temperature dependent shift of a narrow (width of a few cm^{-1}) peak (a so-called van Hove singularity) in the two-phonon DOS. For natural GaP, a kink at $366\,\mathrm{cm}^{-1}$ has been detected at 10 K. If this kink shifts to lower frequencies with rising temperature $\rho(\omega)$ becomes considerably temperature dependent.

A plot of the frequency dependence of $\Gamma = (T_2)^{-1}$ experimentally determined for various temperatures in the range between 10 K and 250 K (see Fig. 33) shows a pronounced peak of $\Gamma(\omega)$ which moves from $365\,\mathrm{cm}^{-1}$ to $361\,\mathrm{cm}^{-1}$ with increasing temperature. This peak has to be attributed to $\rho(\omega)$ if we assume that the frequency dependence of $|V_3|^2$ and $[1 + \mathrm{n}(\omega_1, T) + \mathrm{n}(\omega_2, T)]$ is negligible in the region 357–366 cm^{-1}.

Figure 33 clearly demonstrates that the shift of the peak in $\rho(\omega)$ with T can result in a dramatically different temperature dependence of the dephasing time of polaritons with only slightly different frequencies (see Fig. 33). Let us consider for example the polariton at $365\,\mathrm{cm}^{-1}$. At low temperature the peak of $\rho(\omega)$ appears at this frequency. For increasing temperature the phonon occupation numbers increase. According to Eq. (12) this should imply an increase of $\Gamma(\omega)$. However this increase is compensated by a decrease of $\rho(\omega)$ associated with the shift of the peak to lower frequency. This leads to an almost temperature independent dephasing rate (see Fig. 33).

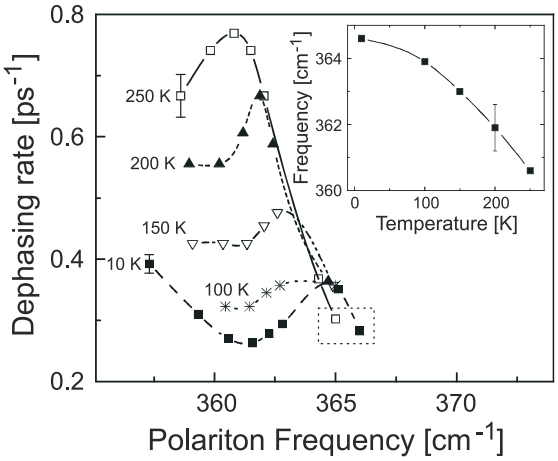

Figure 33: *Frequency dependence of the TO phonon-polariton dephasing rate in GaP measured at 10, 100, 150, 200, and 250 K. Two points in the dashed square at the bottom-right corner have been determined from TO-phonon linewidths measured by spontaneous Raman scattering. The lines are guides to the eye. The inset shows the shift of the maximum in the dephasing rate (related to the peak in ρ(ω,T)) with temperature.*

The peak of $\rho(\omega)$ moves below $363\,\mathrm{cm}^{-1}$ only for temperatures higher than 150 K. As a result (see Fig. 33) the decay rate of the polariton at $363\,\mathrm{cm}^{-1}$ approximately follows Eq. (12) in the 10–150 K range, but deviates to values smaller than predicted for temperatures above 150 K. Finally, the mode at $361\,\mathrm{cm}^{-1}$ exhibits a minimum in the dephasing rate (see Fig. 33) and accordingly in $\rho(\omega)$ at low temperature. The shift of the peak in $\rho(\omega)$ to this position causes a considerably stronger (up to 50%) rise of the dephasing rate than expected for the change in the occupation numbers (see solid line in Fig. 33).

The unusual temperature dependence of $\Gamma(\omega)$ for polariton modes with slightly different frequencies (see Fig. 32) can be satisfactorily explained if the temperature dependence of both the acoustic phonon occupation numbers and the position of the peak in $\rho(\omega, T)$ are taken into account. There is no need to consider higher order anharmonic decay process. The inset of Fig. 33 displays the measured temperature dependence of the relative maximum of the dephasing rate caused by a shift of the peak of $\rho(\omega, T)$. The shift of $4\,\mathrm{cm}^{-1}$ (equivalent to approximately 1% change) is at least two times larger than measured values for the shift of the TO frequency in the same temperature range. This faster shift of the peak in the two-phonon DOS as compared to the TO-phonon frequency is the origin of the extraordinary variation of $\Gamma(\omega)$ with T.

In summary, the temperature and frequency dependence of the (TO) phonon-polariton decay time T_2 in GaP has been measured by ISRS spectroscopy. The experimental data clearly show a shift of a van Hove singularity in the two phonon DOS at $(\mathrm{TA}+\mathrm{LA})_\mathrm{K}$ corresponding to acoustic phonons from $365\,\mathrm{cm}^{-1}$ to $361\,\mathrm{cm}^{-1}$ if T is raised from 10 to 250 K. If this shift is taken into account, the puzzling temperature dependence of T_2 can be well described by a 3^{rd}-order anharmonic decay.

Strongly correlated systems

The fascinating property of strongly correlated systems is the evolution of new elementary excitations as a result of strong interactions. This is studied in a variety of systems. In transition metal oxides orbital degeneracy may lead to collective orbital excitations and the spin structure and excitations are controlled by the orbital degree of freedom. In fractional quantum Hall systems composite fermions appear as new elementary excitations and provide a useful description of cyclotron resonance in 2D electron systems. Interacting 1D metals show properties of a Luttinger liquid. Renormalization group methods are employed to explore the singular low-energy behavior of Luttinger liquids in presence of impurities. Scanning tunneling spectroscopy provides a powerful tool to investigate the changes in electronic structure in the vicinity of Kondo impurities.

Interplay between spin and orbital dynamics in cubic vanadates

C. Ulrich, G. Khaliullin, H. He, P. Horsch, A.M. Oleś, and B. Keimer;
M. Reehuis (Hahn-Meitner-Institut, Berlin); M. Ohl (Institut Laue-Langevin, Grenoble);
S. Miyasaka and Y. Tokura (University of Tokyo)

The interplay between spin and orbital degrees of freedom in transition metal oxides has been a subject of investigation since the 1950's. As one of the salient outcomes of this effort, the 'Goodenough-Kanamori rules' provide a description of the exchange interactions between magnetic atoms, and hence the magnetic ordering pattern, in terms of the relative orientation of valence orbitals on neighboring lattice sites. This field has recently moved back into the center of attention in solid state physics, as advances in materials preparation have made it possible to investigate not only the *static* spin and orbital arrangements, but also the spin and orbital *dynamics* in a variety of *d*-electron systems. In cubic manganites, the focus of much of the recent attention, the spin-wave excitations have been studied extensively, and excitations associated with the *d*-orbital degrees of freedom have recently also been detected.

In transition metal oxides with perovskite structure, such as the manganites, the cubic crystal field splits the *d*-orbital manifold of a free transition metal atom into a lower-lying triplet of t_{2g} symmetry and a higher-lying e_g doublet. In the manganites, where the e_g doublet is partially occupied, coupling to the lattice through the Jahn-Teller effect lifts the orbital degeneracy and generally pushes the orbital excitations to energies much larger than the magnon band width. The spin and orbital dynamics are thus largely decoupled in these materials. A dynamical coupling between both sectors only occurs in special situations, in particular near phase boundaries separating states with different orbital ordering patterns where soft orbital excitations can induce anomalies in the spin excitation spectra. For t_{2g} orbitals, on the other hand, the higher degeneracy and the more isotropic, less bond-directional charge distribution reduces the lattice coupling, and one may expect a more dramatic interplay between the orbital and the spin dynamics. Apart from some experimental and theoretical work on cubic titanates, however, the spin and orbital excitations in transition metal oxides with t_{2g} valence electrons remain largely unexplored to-date.

Here we report elastic and inelastic magnetic neutron scattering experiments on the spin dynamics of the Mott insulators $LaVO_3$ and YVO_3, each of which has two *d*-electrons partially occupying the t_{2g} orbitals of the V^{3+} ion. Prior experiments on these materials provide ample, albeit indirect, evidence of a soft orbital sector. In particular, YVO_3 undergoes a sequence of transitions between states with different orbital and spin ordering patterns as a function of temperature [Y. Ren *et al.*, Nature **396**, 441 (1998)]. Elastic neutron scattering data, measured on the four circle neutron diffractometer E5 at the Hahn-Meitner Institute in Berlin, on a large single crystal grown by the floating zone technique, are shown in Fig. 34.

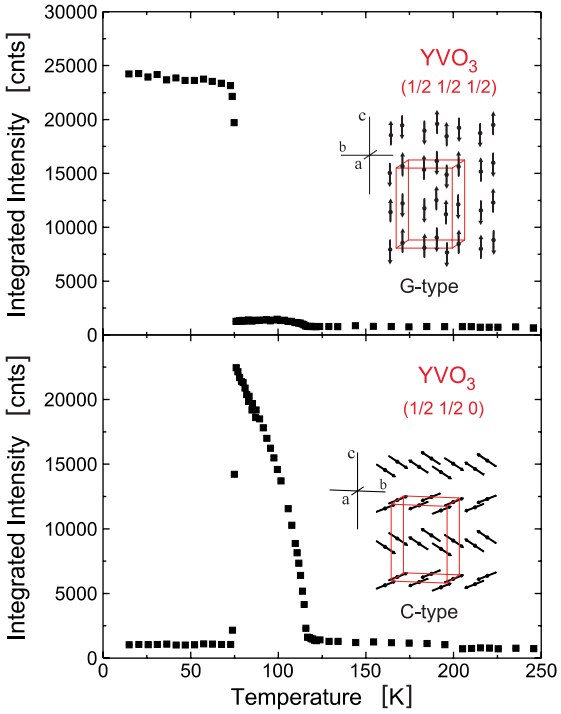

Figure 34: *Integrated intensities of two magnetic Bragg reflections of YVO_3 as a function of temperature. The Bragg peaks (0.5 0.5 0) and (0.5 0.5 0.5) correspond to the C-type and the G-type spin arrangements, respectively. The sketches (inset) show the spin ordering patterns in the low temperature and intermediate temperature phase, respectively.*

At low temperatures, the spin structure is G-type, that is, antiferromagnetic in all three spatial directions. At 77 K, a transition into a C-type spin structure takes place, that is, the exchange coupling along the *c*-axis becomes ferromagnetic while it remains antiferromagnetic in the *ab*-plane. The magnetic transition is accompanied by a structural transition that has been interpreted in prior work [Y. Ren *et al.*, Nature **396**, 441 (1998)] as evidence of orbital reordering from a C-type to a G-type arrangement of the *xz* and *yz* valence orbitals occupied by one of the two *d*-electrons; the other *d*-electron is assumed to remain in the *xy*-orbital. Upon further heating, the C-type antiferromagnetic order disappears at 114 K, and the G-type orbital order at 200 K.

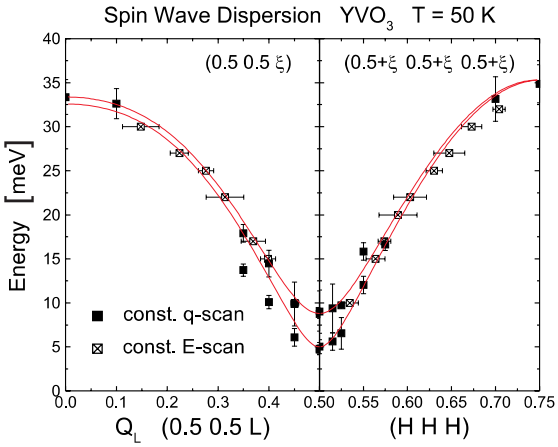

Figure 35: *Spin wave dispersion relations of YVO_3 in the G-type low temperature phase ($T = 50$ K). The lines are results of a fit to a standard magnon dispersion as described in the text.*

The elastic neutron scattering data in the intermediate phase already provide some indication of the unusual nature of this phase. First, the ordered magnetic moment, 1.05 μ_B, must be regarded as anomalously small, as one would expect only a slight reduction of the full 2 μ_B moment of the two electrons by zero-point and thermal fluctuations at these temperatures. Second, the full magnetic structure in the intermediate phase, though predominantly C-type, turns out to be highly non-collinear. The non-vanishing intensity of the $(\frac{1}{2}, \frac{1}{2}, \frac{1}{2})$ reflection for $77\,\mathrm{K} < T < 114\,\mathrm{K}$ (Fig. 34) is a manifestation of this non-collinearity. (For simplicity we neglect tilting distortions of the VO_6 octahedra

and use a pseudocubic unit cell to index the reflections.) A detailed crystallographic analysis shows that the G-type component of the non-collinear structure is oriented along the *c*-axis (not shown in Fig. 34). Its amplitude is about 30% of the total sublattice magnetization.

The unconventional nature of the intermediate phase is further highlighted by an inelastic neutron scattering study of the spin dynamics performed at the triple axis neutron spectrometer IN22 at the Institut Laue-Langevin in Grenoble, France. The dispersion curve in the low temperature phase ($T < 77\,\mathrm{K}$) extracted from the inelastic scattering data is shown in Fig. 35. The spectra are well described by a Heisenberg Hamiltonian with antiferromagnetic exchange parameter $J_c \sim J_{ab} \sim 5.5\,\mathrm{meV}$ and moderate single-ion and exchange anisotropy terms. These parameters are within the normal range expected for a $S = 1$ system. In contrast, the spin wave dispersions in the intermediate phase are very unusual, in particular along the *c*-axis where the exchange coupling is ferromagnetic. The measured magnetic intensity and spin wave dispersions are plotted in Fig. 36. Several anomalies are apparent. First, the exchange constants extracted from a fit to the magnon dispersions, $J_c = -3.1\,\mathrm{meV}$ and $J_{ab} = 2.6\,\mathrm{meV}$, are about a factor of two smaller than in the low temperature phase (Fig. 35). This overall collapse of the magnon spectrum is not in accord with the conventional superexchange models. In addition, $|J_c|$ is actually larger than $|J_{ab}|$, in striking contrast to the Goodenough-Kanamori rules according to which ferromagnetic superexchange interactions are generally significantly smaller than antiferromagnetic interactions. Finally, the splitting of the magnon spectrum into acoustic and optical branches along *c* is completely unexpected. In particular, detailed spin wave calculations show that it is not a simple consequence of the non-collinear spin structure.

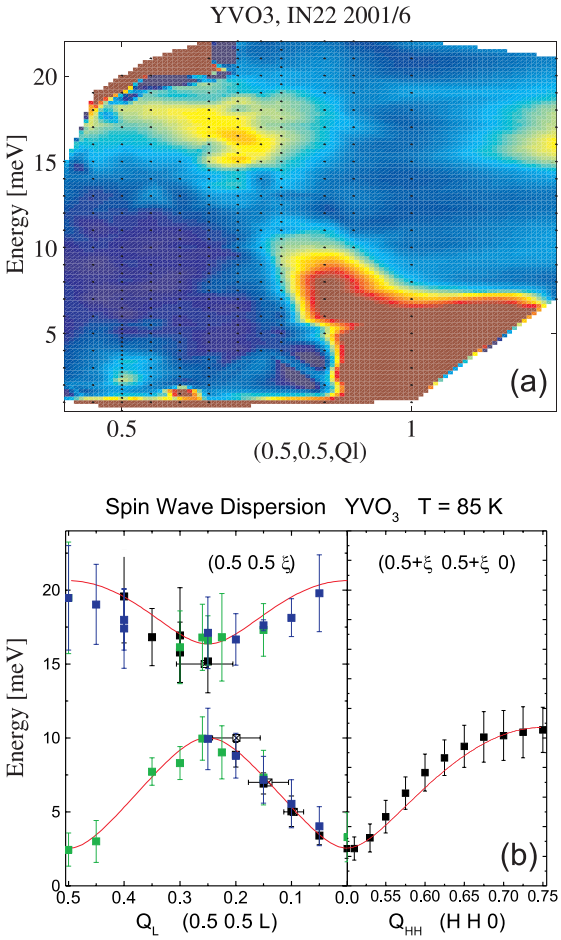

Figure 36: *(a) Magnetic intensity measured in the C-type intermediate temperature phase ($T = 85\,K$) of YVO_3 along $(\frac{1}{2},\frac{1}{2},\xi)$. (b) Spin wave dispersion relations of YVO_3 in the C-type phase at the same temperature. The lines are results of a fit to the orbital dimer model described in the text.*

For comparison, we have carried out an inelastic neutron scattering experiment of $LaVO_3$, which also has a C-type spin structure in its magnetically ordered phase. The spin wave spectrum extracted from these data is shown in Fig. 37, together with a fit to a standard spin wave dispersion. None of the unusual features characterizing the intermediate phase of YVO_3 are present: The exchange parameters ($J_c = -4.0\,\mathrm{meV}$, $J_{ab} = 6.5\,\mathrm{meV}$) are comparable to those of YVO_3 at low temperatures; their magnitudes are close to the expected ratio; and neither a non-collinearity of the spin structure nor an optical-acoustic splitting of the magnon dispersions are found.

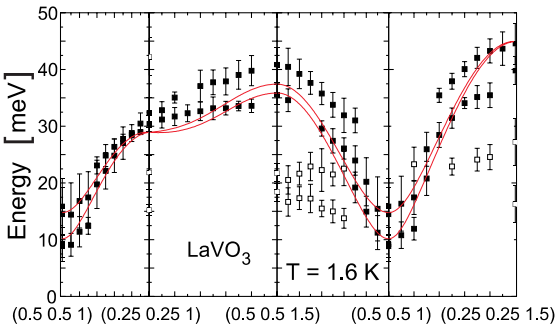

Figure 37: *Spin wave dispersion relations of $LaVO_3$ in the C-type antiferromagnetic phase. The lines are results of a fit to a standard magnon dispersion as described in the text. The open symbols indicate phonons.*

In order to explain the unusual magnetism of YVO_3 in the intermediate phase, we follow a model suggested earlier by Ren *et al.* and assume that the *xy*-orbital dominates the antiferromagnetic coupling within the layers. Along the *c*-axis, the superexchange Hamiltonian can be written to first order as

$$H = \frac{t^2}{U} \sum_{<ij>} (\vec{S}_i \cdot \vec{S}_j + 1)(2\vec{\tau}_i \cdot \vec{\tau}_i + \frac{1}{2})$$

where t is the hopping parameter, U is the intra-atomic Coulomb repulsion, $\vec{S}$ is a spin-1 operator and $\vec{\tau}$ a pseudospin-$\frac{1}{2}$ operator acting in the subspace spanned by the *xz* and *yz* orbitals responsible for the superexchange along the *c*-axis direction. The standard ferromagnetic superexchange in a state with classical orbital order arises from additional terms in the Hamiltonian that are reduced in magnitude by a factor of J_H/U, where J_H is the intra-atomic Hund's rule interaction. A novel mechanism for ferromagnetic superexchange arises if orbital fluctuations are present. An easy way to see this is to consider a pair of vanadium ions along *c*: An orbital singlet with $2\langle\vec{\tau}_i \cdot \vec{\tau}_j\rangle = -\frac{3}{2}$ gives a large ferromagnetic exchange coupling. A full many body theory incorporating orbital singlets appears capable of explaining many of the experimentally observed features of the intermediate phase, including in particular the non-collinear spin structure and the optical-acoustic splitting. The latter could arise from dimerization of the pseudospin-$\frac{1}{2}$ orbital chain, analogous to the spin-Peierls instability. Possible crystallographic manifestations of this instability are currently under investigation.

In summary, our experiments have established the insulating cubic vanadates as an interesting model system to explore the interplay between spin and orbital dynamics. The spin excitations probed by neutron scattering are highly sensitive to the details of the orbital state. The next step will be an attempt to explore the orbital excitations directly over the entire Brillouin zone by neutron scattering, as has been done recently by Raman scattering at the zone center. Detailed predictions for the 'orbiton' dispersions were made on the basis of the model discussed above. Further, it will be interesting to continue these investigations in doped systems, as both $LaVO_3$ and YVO_3 are known to undergo insulator-to-metal transitions when the number of *d*-electrons is changed by chemical substitution.

Spin order due to orbital fluctuations: cubic vanadates

P. Horsch, G. Khaliullin, and A.M. Oleś

Large Coulomb interactions play a crucial role in transition metal oxides, and are responsible for the collective behavior of strongly correlated *d* electrons which localize in Mott-Hubbard insulators. Such localized electrons may occupy degenerate orbital states which makes it necessary to consider orbital degrees of freedom on equal footing with electron spins, and leads to effective (superexchange) spin-orbital models to describe the low-energy physics. A remarkable feature of these models is that the superexchange interaction is *highly frustrated* on a cubic lattice, which was recognized as the origin of novel quantum effects in transition metal oxides. In the case of e_g systems, however, quantum fluctuations of orbitals are largely suppressed by the Jahn-Teller (JT) effect, which together with superexchange often leads to structural phase transitions accompanied by a classical ordering of occupied orbitals.

The transition metal oxides with partly filled t_{2g} orbitals, like the titanates and vanadates, exhibit different and more interesting phenomena due to the stronger quantum fluctuations among orbitals. This occurs because of the relative weakness of the JT coupling in this case and due to the higher degeneracy of t_{2g} states.

We derived the spin-orbital superexchange model for cubic vanadates, and investigated the low-temperature phases of $LaVO_3$ and YVO_3. The magnetic order in $LaVO_3$ is C-type (ferromagnetic chains along *c*-axis which stagger within (a,b) planes), with a Néel temperature $T_N = 143\,K$, whereas the magnetic order is staggered in all three directions (G-type) in YVO_3 for $T < 77\,K$ and C-type at higher temperatures $77 < T < 118\,K$ (Fig. 38). The C-phase is particularly surprising in the practically undistorted structure of $LaVO_3$ at $T > T_N$.

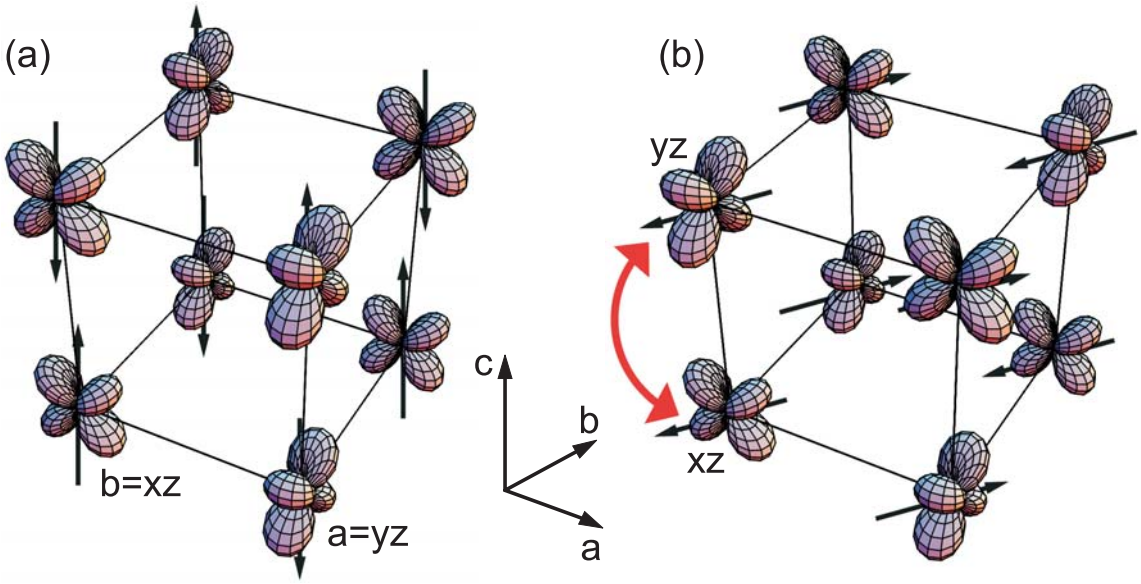

Figure 38: *Magnetic G- (a) and C-structures (b) with $S = 1$ spins indicated by black arrows. For the C-phase a red arrow indicates the fluctuating orbital occupation between $a = yz$ and $b = xz$ orbitals along the c-direction, while the second t_{2g} electron occupies the xy orbital ($n_c = 1$) at each vanadium ion, which is not shown.*

In order to understand the microscopic origin of the competition of C- and G-phases we address the following questions: (i) can the superexchange interactions *alone* explain why the ferromagnetic (FM) and antiferromagnetic (AF) interactions coexist in $LaVO_3$ in spite of a practically ideal cubic structure at $T > T_N$ with almost equal V–V bonds; (ii) why does the structural transition in $LaVO_3$ occur only *below* the magnetic transition; and (iii) why is the G-type AF order stable in the low-temperature phase of YVO_3, while the C-type order *wins* at higher temperatures?

We start with a Mott-insulator picture of cubic vanadites. Due to the large Hund coupling J_H the V^{3+} ions are in a triplet configuration. The t_{2g} superexchange interactions between $S = 1$ spins arise from the virtual excitations $d_i^2 d_j^2 \rightarrow d_i^3 d_j^1$ on a given bond $\langle ij \rangle$, with the hopping t allowed only between two out of three t_{2g} orbitals: *yz*, *zx*, and *xy*, depending on the bond direction. These orbitals are perpendicular to three cubic directions, and will be labeled by $\gamma = a, b$, and c, respectively.

It is instructive to consider first the spin-orbital Hamiltonian in the absence of Hund and Jahn-Teller coupling:

$$H_0 = \frac{1}{2} J \sum_{\langle ij \rangle_\gamma} (\vec{S}_i \cdot \vec{S}_j + 1) \left(\vec{\tau}_i \cdot \vec{\tau}_j + \frac{1}{4} n_i n_j \right)^{(\gamma)}, \quad (13)$$

where the first factor represents the Heisenberg interaction between spins, while the second factor is an operator which acts in the pseudospin space of orbitals. A remarkable feature of the t_{2g} superexchange in Eq. (13) is that every bond is represented by two equivalent orbitals giving a SU(2) symmetric structure $(\vec{\tau}_i \cdot \vec{\tau}_j + \frac{1}{4} n_i n_j)^{(\gamma)}$ of the orbital part. Here $\vec{\tau}_i$ are Pauli-matrices in the space of the (two) active orbitals, whose selection depends on the direction γ. Depending on the type of orbital correlations this may result in a spin coupling constant of either sign. This important property resembles that of the one-dimensional (1D) SU(4) model. The present problem is however more involved since there are *three* t_{2g} *flavors* in a cubic crystal, and SU(2) orbital correlations among two of them along a particular direction will necessarily frustrate those correlations in the other directions. We argue that orbital singlets (with $n_{ia} + n_{ib} = 1$) may form on the bonds parallel to c axis, thereby exploiting fully the SU(2) symmetry of the orbital interactions in one direction. The second electron occupies the third t_{2g} orbital ($n_{ic} = 1$), and controls the spin interactions in the (a, b) planes.

In order to understand why orbital fluctuations support the C-AF type spin order, it is instructive to consider first a single bond along c-axis. A crucial observation is that the lowest energy of $-J/2$ is obtained when the spins are *ferromagnetic*, and the orbitals a and b form a singlet, with $\langle \vec{\tau}_i \cdot \vec{\tau}_j \rangle^{(c)} = -\frac{3}{4}$. Thus, one finds a *novel mechanism of ferromagnetic interactions* which operates due to local fluctuations of a and b orbitals. At the same time, the orbital resonance on the bonds in (a, b) planes is blocked, as $n_{ic} = n_{jc} = 1$, leading to antiferromagnetic interactions along these directions. Such an electron distribution and the formation of quasi one-dimensional orbital pseudospin chains supports FM spin order along c-axis, and breaks the cubic symmetry in the orbital space as well. This explains why the magnetic transition into the C-phase in $LaVO_3$ is accompanied by a weak structural distortion.

Based on the full Hamiltonian $H = H_0 + H_\eta + H_{JT}$, which accounts in addition for the Hund interaction $\eta = J_H/U$ and the Jahn-Teller coupling, we calculated the magnetic exchange constants in the different phases. Taking realistic parameters for the model, i.e., $t = 0.2$, $U = 4.5$ and $J_H = 0.68$ eV which results in $J = 35.6$ meV, we obtain for the exchange constants in the C-phase $J_{ab} \simeq 7.1$ and $J_c \simeq -9.3$ meV. We emphasize that the orbital quantum fluctuations play here a dominant role and the well known Hund's mechanism due to J_H alone *would not suffice* to obtain $|J_c| > J_{ab}$ as suggested by experiment (Keimer *et al.*), and would give instead $J_c \simeq -4.4$ meV.

On the other hand we find $J_{ab} \simeq 5.9$ and $J_c \simeq 6.9\,$meV for the G-phase of YVO_3. This demonstrates that the magnetic structure depends sensitively on the orbital state – the exchange constant J_c which is FM in $LaVO_3$ changes into the *strongest* AF bond in the G-phase of YVO_3.

Next we consider the reasons for the stability of the G-phase in YVO_3. Unlike $LaVO_3$ with almost equal V–V bonds, this compound crystalizes in a distorted structure, indicating that the JT effect plays a significant role. It was suggested that energy may be gained due to C-type *orbital ordering*, with *a* and *b* orbitals staggered in (a,b) planes and repeated along *c*-axis, while $n_{ic} = 1$. Such ordering can be promoted by

$$H_{JT} = -2V \sum_{\langle ij\rangle \| c} \tau_i^z \tau_j^z + V \sum_{\langle ij\rangle \| (a,b)} \tau_i^z \tau_j^z , \quad (14)$$

and *competes with the orbital disorder*. This behavior is remarkably different from the e_g systems, where the JT effect and superexchange support each other, inducing orbital ordering. While $V > 0$ causes orbital splitting by $4V$ and thus lowers the energy of the G-phase, it has little effect on the energy of the C-phase.

Orbital excitations are quite different in both AF phases: while the orbital excitation gap is small and grows $\propto \sqrt{\eta}$ in C-phase, a large gap $\approx 4V$ opens in the orbital wave spectrum of G-phase. Thus, both the larger quantum fluctuations and additional (classical) energy gain due to finite J_H in the C-phase have to be overbalanced by the JT energy $\propto V$ in order to stabilize the G-AF order at $T \to 0$. However, the G-phase may be destabilized at finite T by larger orbital entropy of the C-phase. Indeed, taking $V = 0.65\,J$ and $\eta = 0.15$, the free energy gives a transition from G- to C-phase around $T^* \simeq 0.8\,J$ (Fig. 39). While this behavior reproduces qualitatively the first order phase transition observed in YVO_3, its quantitative description requires a careful consideration of lattice and spin entropy contributions to the free energy. These effects are expected to reduce the transition temperature T^* down to experimental values.

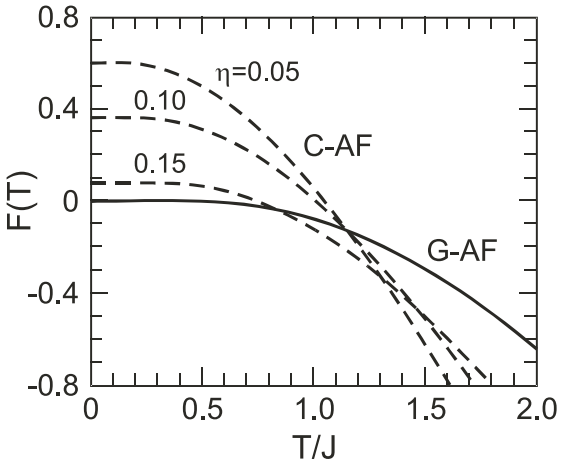

Figure 39: *Free energies for YVO_3 (in units of J) as a function of temperature T/J for the G-phase ($V = 0.65\,J$) which is stable at low temperature, and for the C-phase calculated for different Hund coupling parameters $\eta = J_H/U$.*

Summarizing, strong t_{2g} orbital fluctuations in cubic vanadites lead to a new mechanism of ferromagnetic superexchange which stabilizes the C-phase in first undistorted $LaVO_3$, and the structural transition follows. The JT effect opposes the superexchange and can stabilize the G-phase with orbital ordering but only at low temperatures, as the fluctuations of t_{2g} orbitals release high entropy, and are thus responsible for the transition from the orbital ordered G-phase into the orbital disordered C-phase in YVO_3.

Epitaxial strain as an experimental tool to tailor the properties of perovskite-type transition metal oxides

X.-J. Chen, H. Zhang, S. Soltan, G. Cristiani, and H.-U. Habermeier

Currently, the investigation of transition metal oxides has gained enormous interest, mainly stimulated by the discovery of superconductivity at high temperatures in cuprates and a colossal magnetoresistance in manganites. Both classes of material have in common that their crystal structure is perovskite-type and their electronic ground state for the undoped parent compounds La_2CuO_4 and $LaMnO_3$, respectively, is an antiferromagnetic insulator. The physical properties of both, the cuprates and the manganites are determined by strong electron correlation effects which in turn sensitively depend on the bond length and bond distance of the transition metal-oxygen structural unit. In order to artificially modify the bond length and/or bond angle thin film technology offers an alternative to conventional solid state chemical approaches where dedicated substitutions of ions with different radii are used. Selecting an appropriate substrate with a lattice constant slightly different from the cuprate or manganite bulk material and choosing deposition conditions suitable for epitaxial growth is an experimental concept to directly tailor the geometry of the structural units and thus the physical properties. When a film is grown on a substrate whose lattice parameter is slightly smaller or larger than that of the bulk, the epitaxial strain is expected to be compressive or tensile, respectively.

Strain effects have been observed so far in cuprates and manganites as well. In the case of manganite thin films tensile strain generally suppresses ferromagnetism and reduces the Curie temperature T_C, whereas compressive strain reduces resistivity and shifts T_C to higher values. The observed strain effects have been interpreted qualitatively within the frame of the Zener double exchange model. In this model the hopping matrix element, t_{ij}, for the Mn-O-Mn electron transfer depends on the spatial wavefunction which can be altered by changing bond length and bond distance of the Mn-O-Mn unit.

We have chosen $La_{0.9}Sr_{0.1}MnO_3$ for our experiments because the lightly doped materials show a great variety of intriguing phenomena (such as charge order, orbital order and phase separation) originating from a delicate interplay of charge, spin, orbital and lattice degrees of freedom. Thin films of $La_{0.9}Sr_{0.1}MnO_3$ with various thickness d, in the range from 20 nm to 200 nm have been deposited by the pulsed laser deposition technique onto $SrTiO_3$ (100)-oriented single crystals and their structure, transport and magnetic properties have been measured. X-ray diffraction and cross-sectional TEM reveals single phase, epitaxially grown material and chemical analysis of inductively coupled plasma (ICP) shows a (La,Sr)/Mn ratio of 1:1 with a Sr content of 0.1 ± 0.005. Figure 40 shows the temperature dependence of the magnetization of the films (measured in 0.5 T) of various values for d after zero field cooling. The curves are characteristic for a ferromagnetic transition. Both, T_C as well as M(0) increase with decreasing d.

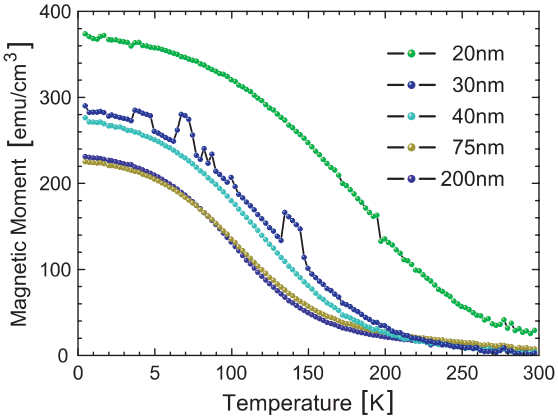

Figure 40: *Magnetization as a function of temperature (measured in a field of 0.5 T) of $La_{0.9}Sr_{0.1}MnO_3$ films with various thicknesses.*

We have not observed a magnetization jump occurring at a characteristic temperature T_{CA} typical for single crystal $La_{0.9}Sr_{0.1}MnO_3$ which is ascribed to a canted antiferromagnetic state. The corresponding data for the resistivity are shown in Fig. 41. The films display at high temperatures a semiconductor-like behavior followed by a metallic one in the temperature range $T_{CA} < T < T_{MI}$ where the metal insulator transition temperature T_{MI} is defined as the temperature where the temperature derivative of resistivity changes sign. For lower temperatures an upturn is observed corresponding to a certain T_{CA}. There are three main results to be mentioned from this measurement. 1.) The resistivity in our films is much smaller compared to single crystals; at $T = 100$ K single crystals have $\rho = 1000\,\Omega$ cm whereas the 200 nm film shows $84\,\Omega$ cm, only. 2.) T_{MI} shifts to smaller values with decreasing film thickness and 3.) T_{CA} decreases with decreasing film thickness.

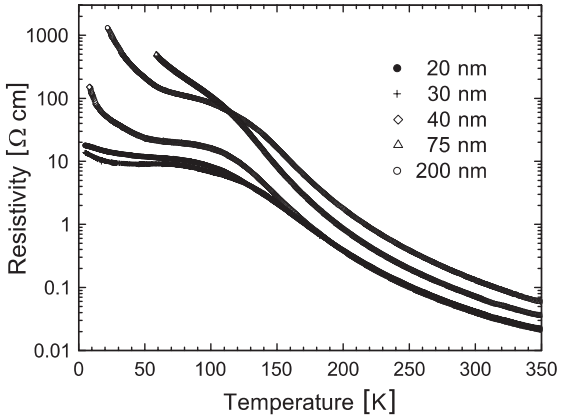

Figure 41: *Temperature dependence of the resistivity of $La_{0.9}Sr_{0.1}MnO_3$ films with various thicknesses.*

Qualitatively, these findings are consistent with the model of strain induced changes of the transport and magnetic properties. The films are under compressive strain given by the in-plane lattice mismatch between film and substrate of $\approx 0.6\%$, this causes a reduced Mn-O-Mn bond distance and thus an enhanced hopping matrix element for Mn-O-Mn transfer. Beyond these qualitative arguments our measurements allow some deeper insight into the coupling of the electronic and phononic system of the manganites. It is well known, that the double-exchange mechanism is not able to quantitatively describe the system. The calculated resistivities have the wrong magnitude, a too slow doping dependence and an incorrect behavior for $T < T_C$ or in a magnetic field. Millis therefore suggested a polaron effect to lift these discrepancies. It is argued that the Jahn-Teller splitting from the Mn^{3+} ions generates a strong electron-phonon coupling. If the preconditions for polaron formation, namely a large electron-phonon coupling and low electronic hopping rates, are fulfilled, the temperature dependence of resistivity is a result of hopping of adiabatic small polarons. Within the model for adiabatic small polaron hopping as developed by Emin and Holstein the resistivity ρ is given by

$$\rho = A \cdot T \cdot exp\left(\frac{E_A}{k_B T}\right), \qquad (15)$$

where A depends on the polaron density, the hopping distance and the frequency of the longitudinal optical phonon. The activation energy has the form $E_A = E_P/2 + \varepsilon_0 - J$, where E_P denotes the polaron formation energy, ε_0 the energy required to generate intrinsic carriers, and J the transfer integral. Figure 42 shows the excellent agreement of our data to Eq. (15) for the temperature range $165\,K < T < 350\,K$ from which the values for A and E_A can be derived. In the adiabatic limit and for high temperatures the contributions ε_0 and J can be neglected, consequently, $E_P = 2E_A$.

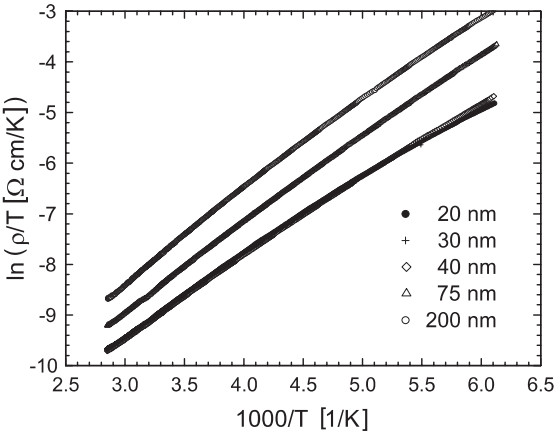

Figure 42: *Plot of ln(ρ/T) versus 1000/T of $La_{0.9}Sr_{0.1}MnO_3$ films of various thicknesses.*

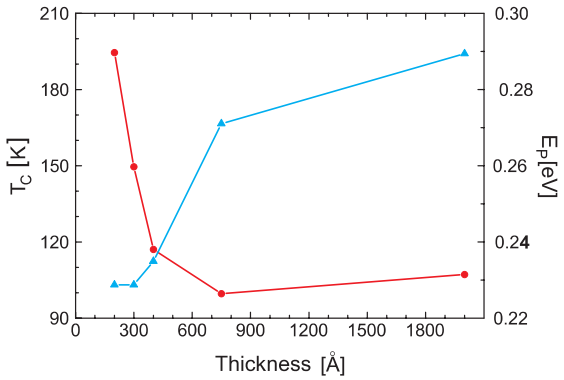

Figure 43: *Thickness dependence of T_C (circles) and polaron formation energy E_P (triangles) in $La_{0.9}Sr_{0.1}MnO_3$ films.*

Plotting T_C and E_P as a function of film thickness (Fig. 43) we find an interesting correlation of both quantities with d. For films with a thickness $d > 75$ nm, where the strain is relaxed, both T_C and E_P scarcely change with d whereas for $d < 75$ nm, i.e., in the case of strained films, E_P decreases and T_C increases with decreasing d. This indicates that electron-phonon coupling possibly dominates the strain effect on T_C. Contributions arising from the strain dependence of electronic bandwidth could be estimated to be much smaller compared to the electron-phonon coupling.

In conclusion, we used $La_{0.9}Sr_{0.1}MnO_3$ thin films to demonstrate the possibility to artificially modify the physical properties of perovskite-type transition metal oxide thin films by epitaxial strain. The compressive epitaxial strain reduces resistivity and enlarges the Curie temperature. The high temperature resistivity of the films with various thickness can be described within the frame of small polaron hopping in the adiabatic limit.

Cyclotron resonance of composite fermions

I.V. Kukushkin, J.H. Smet, and K. v. Klitzing; W. Wegscheider (Universität Regensburg)

The introduction of suitable fictitious entities, quasi-particles, occasionally permits to cast otherwise difficult strongly interacting many-body systems in a single particle form. We can then take the customary physical approach, using concepts and representations, which formerly could only be applied to systems with weak interactions, and yet still capture the essential physics. A notable recent example occurs in the conduction properties of a two-dimensional electron system (2DES), when exposed to a strong perpendicular magnetic field B. They are governed by electron-electron interactions, that at low temperatures bring about the Nobel prize awarded fractional quantum Hall effect (FQHE). Composite fermions [O. Heinonen, Editor, *'Composite Fermions'*, World Scientific Publishing, 1998], each assembled from one electron and two (or more generally, an even number) magnetic flux quanta, were identified as apposite quasi-particles that simplify considerably our understanding of the FQHE. The flux attachment is a natural way to minimize the energy of the 2DES, since the associated vortex expels other electrons from its neighborhood and decreases the repulsive Coulomb interaction between adjacent electrons. In many experiments, composite fermions may be viewed as non-interacting.

These composite fermions (CFs) behave as legitimate particles with well-defined charge, spin and statistics. They do not experience the external magnetic field B, but a drastically reduced effective magnetic field B^*, that vanishes exactly when two flux quanta penetrate the sample per electron in the system (filling $\nu = 1/2$). They precess, like electrons, along circular cyclotron orbits, but with a diameter determined

by B^* rather than B. The Landau quantization of this cyclotron motion gives rise to the integer quantum Hall effect of CFs and is equivalent to the FQHE of the original electrons. The frequency of their cyclotron motion remained hitherto enigmatic, since the effective mass is no longer related to the band mass of the original electrons and is entirely generated from electron-electron interactions. Here, we look for the enhanced absorption of a microwave field when it is in resonance with the frequency of the CF circular motion in order to determine their effective mass [I.V. Kukushkin *et al.*, Nature **415**, 409 (2002)].

The search of the CF cyclotron resonance requires substantial sophistication over conventional methods, used to detect the electron cyclotron resonance, since the consequences of Kohn's theorem must be circumvented. This theorem states that in a translationally invariant system homogeneous radiation can only couple to the center-of-mass coordinate.

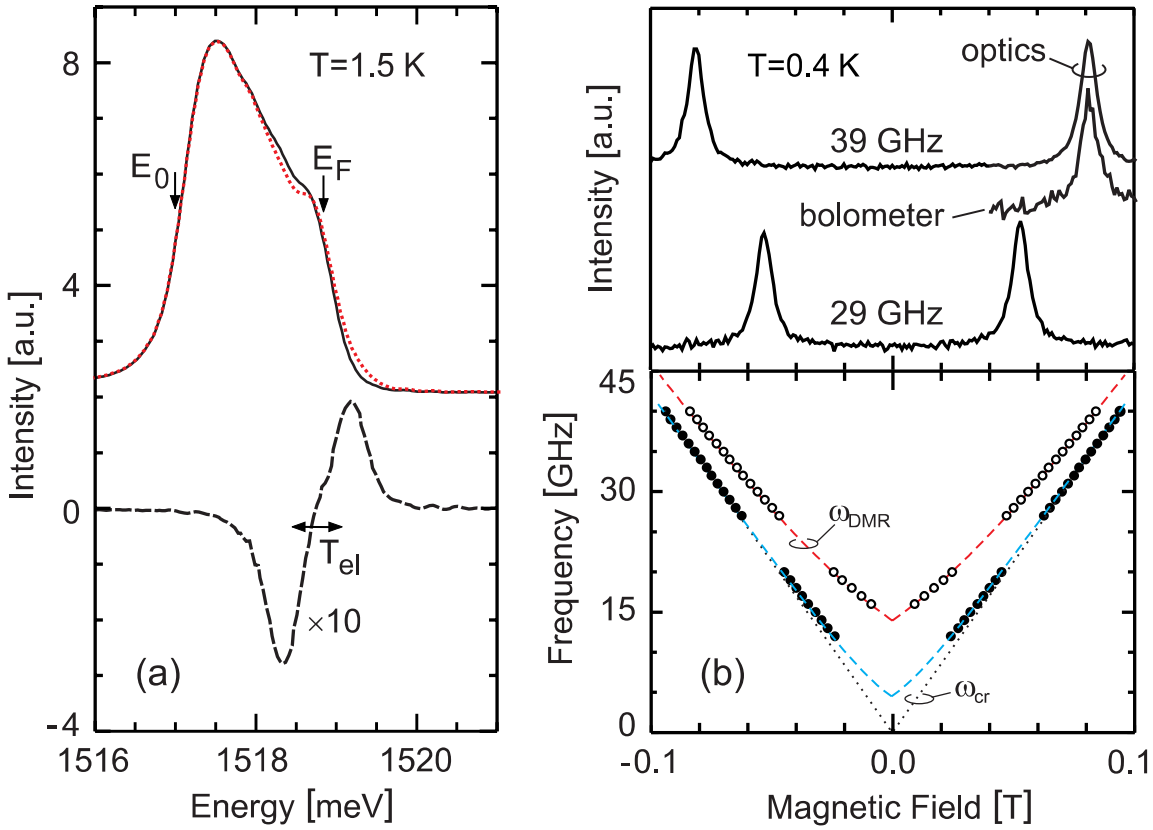

Figure 44: *Illustration of the optical scheme to detect resonant microwave absorption for the electron cyclotron-magnetoplasmon hybrid mode at low B-fields. (a) Luminescence spectrum in the presence of (dotted line) and without (solid line) a 50 μW microwave excitation of 18 GHz obtained on a disk-shaped 2DES with carrier density $n_{2D} = 5.8 \cdot 10^{10}$ cm^{-2} at a fixed magnetic field $B = 22$ mT. The difference reflects the increased electron temperature T_{el} due to resonant microwave absorption for the spectrum obtained in the presence of microwaves. The bottom dashed curve is the differential spectrum obtained by subtracting both curves. (b) Top panel: The microwave absorption amplitude at 29 GHz and 39 GHz as a function of B. The peaks are identified as the dimensional magnetoplasma-cyclotron hybrid mode. The inset shows a conventional bolometer measurement. Bottom panel: Resonance position for $n_{2D} = 1.09 \cdot 10^{11}$ (open circles) and $1.1 \cdot 10^{10}$ cm^{-2} (solid circles) as a function of incident microwave frequency. The dashed lines represents the theoretical dependence of the hybrid dimensional magnetoplasma-cyclotron resonance. The dotted line corresponds to the cyclotron mode only.*

Phenomena originating from electron-electron interactions will thus not be reflected in the absorption spectrum. An elegant way to bypass this theorem is to impose a periodic density modulation to break translational invariance. The non-zero wavevectors defined by the appropriately chosen modulation may then offer access to the cyclotron transitions of CFs, even though they are likely to remain very weak. Therefore, the development of an optical detection scheme, that boosts the sensitivity to resonant microwave absorption by up to two orders of magnitude in comparison with traditional techniques, was a prerequisite for our studies. Furthermore, we exploited to our benefit the accidental discovery that microwaves, already incident on the sample, set up a periodic modulation through the excitation of surface acoustic waves (SAW).

The 2DES, patterned into a 1 mm diameter disk, is placed in a short-circuited microwave waveguide in the electric field maximum of the microwave excitation inside a He3-cryostat. At a fixed *B*-field, luminescence spectra with and without microwave excitation were recorded consecutively. Under resonant conditions heating causes a significate difference between both spectra. This can be highlighted by integrating the absolute value of the difference across the entire energy range. This quantity is considered a measure of the microwave absorption amplitude. The same procedure is then repeated for different values of *B*.

To establish trustworthiness in this unconventional detection scheme, we apply it in Fig. 44 to the well-known case of the electron cyclotron resonance $\omega_{cr} = eB/m^*$, with m^* the effective mass of GaAs ($0.067\,m_0$). Due to its limited size, the sample also supports a dimensional plasma mode that depends on both the density and diameter of the sample. The plasma and cyclotron mode hybridize. The optical method indeed recovers this well-known hybrid mode ω_{DMR}. Additional support for the validity of the detection method comes from a comparison with measurements using a bolometer (Fig. 44(b), top panel). Not only does one find the same resonance position, but also the same line shape. The only difference is the improved signal to noise ratio (30–100 times) for the optical scheme.

Disorder and the finite dimensions of the sample in principle suffice to break translational invariance and outwit Kohn's theorem, as attested by the interaction of the cyclotron and dimensional plasma mode. However, they provide access to internal degrees of freedom either at poorly defined wavevectors or too small a wavevector for appropriate sample sizes. Therefore, the imposition of a periodic density modulation, that introduces larger and well-defined wavevectors, is desirable. Transport experiments in the Hall bar geometry disclosed that additional processing is not required, since the microwaves, already incident on the sample, concomitantly induce a periodic modulation at sufficiently high power. A clear signature is the appearance of commensurability oscillations in the magnetoresistance due to the interplay between the *B*-dependent cyclotron radius of electrons and the length scale of the modulation.

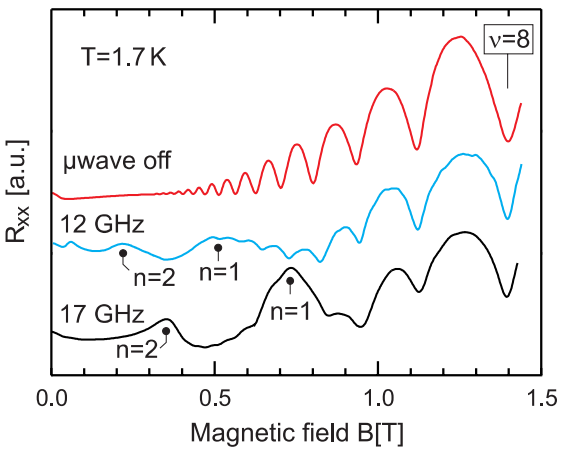

Figure 45: *Magnetotransport data in a Hall bar geometry without (top curve) and under 100 μW of microwave radiation at 12 (middle curve) and 17 GHz (bottom curve). Curves are offset for clarity. Besides the well-known Shubnikov-de Haas oscillations, additional magnetoresistance oscillations appear under microwave radiation. They are commonly observed in 2DESs on which a static periodic modulation of the density has been imposed.*

Examples are displayed in Fig. 45. The following scenario is conceivable: Owing to the piezoelectric properties of the $Al_xGa_{1-x}As$-crystal, the radiation is partly transformed into SAWs with opposite momentum, so that both energy and momentum are conserved. Reflection from cleaved boundaries of the sample then produces a standing wave with a periodicity determined by the sound wavelength. The involvement of sound waves can be deduced from the transport data, since from the minima we can extract the modulation period. The ratio of this period to the sound wavelength at these frequencies is about 1.1.

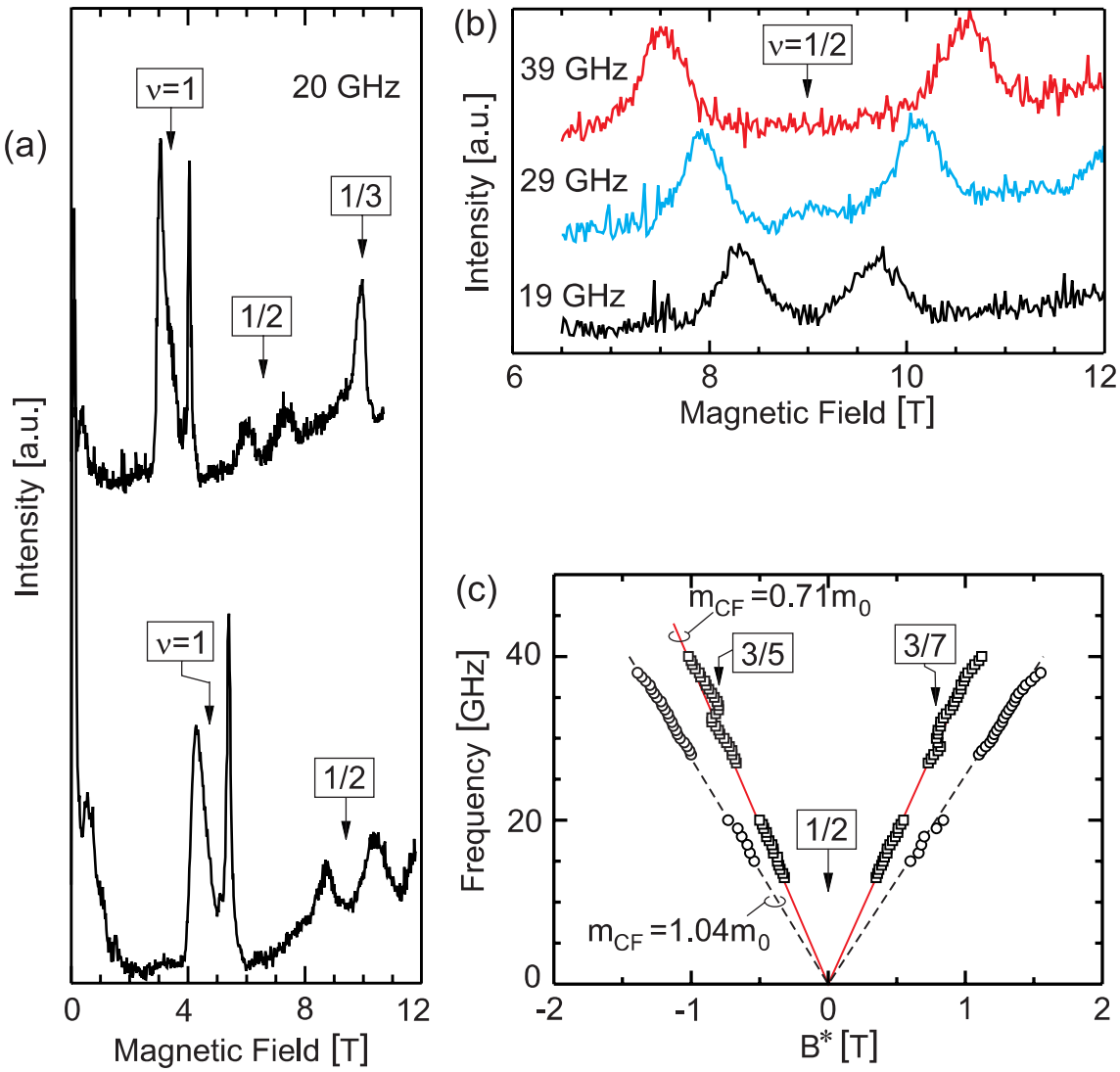

Figure 46: *(a) Microwave absorption amplitude for $n_{2D} = 0.81 \cdot 10^{11}$ and $1.15 \cdot 10^{11}$ cm^{-2} and a frequency of 20 GHz. The response near $\nu = 1$ and 1/3 does not shift with frequency. (b) Microwave absorption amplitude in the vicinity of $\nu = 1/2$ at three different frequencies and $n_{2D} = 1.09 \cdot 10^{11}$ cm^{-2}. (c) Position of the CF cyclotron mode as a function of $B^* = B - 2\phi_0 n_{2D}$ (ϕ_0 is the elementary flux quantum) for $n_{2D} = 1.09 \cdot 10^{11}$ cm^{-2} (circles) and $0.59 \cdot 10^{11}$ cm^{-2} (squares).*

Figure 46(a) depicts the microwave absorption amplitude up to high *B*-fields. Apart from the strong dimensional magnetoplasma-cyclotron resonance signal at low *B*-field discussed above, several peaks, that scale with a variation of the density, emerge near filling 1, 1/2 and 1/3. Those peak positions associated with $\nu = 1$ and 1/3 remain fixed when tuning the microwave frequency and are ascribed to heating induced by non-resonant absorption of microwave power. In contrast, the weak maxima surrounding filling 1/2 readily respond to a change in frequency as illustrated in Fig. 46(b). They are symmetrically arranged around half filling and their splitting grows with frequency.

The *B*-dependence is summarized in Fig. 46(c) for two densities. To underline the symmetry, B^* was chosen as the abscissa. The linear relationship between frequency and field extrapolates to zero at vanishing B^*. We conclude that the resonance in Fig. 46 is the long searched for cyclotron resonance of CFs, $\omega_{cr}^{CF} = eB^*/m_{cr}^{CF}$. The data, shown in Fig. 47, confirm qualitatively the strong enhancement in comparison with the electron mass (more than 10 times) predicted in theory, however a fit to the square root dependence requires a prefactor that is four times larger.

The slope of the CF cyclotron frequency as a function of B^* in Fig. 46(c) defines the cyclotron mass m_{cr}^{CF}. This mass is set by the electron-electron interaction scale, so that a square root behavior on density or *B*-field is forecasted from a straightforward dimensional analysis. It varies from $0.7\,m_0$ to $1.2\,m_0$ as the density is tuned from $0.6 \cdot 10^{11}\,\mathrm{cm}^{-2}$ to $1.2 \cdot 10^{11}\,\mathrm{cm}^{-2}$ [I.V. Kukushkin *et al.*, Nature **415**, 409 (2002)].

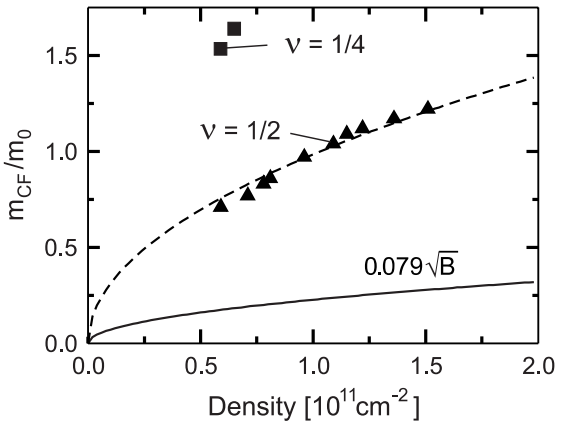

Figure 47: *Dependence of the CF effective mass near $\nu = 1/2$ and 1/4 on the carrier density n_{2D} (solid triangles). The dashed line is a square root fit to the data. The solid curve is a prediction from theory not including finite width of the quasi-two-dimensional electron system and Landau level mixing effects.*

In summary, the fortuitous breaking of translational invariance induced by the microwave irradiation combined with the virtues of an optical detection scheme for resonant absorption has enabled to unveil resonances, symmetrically arranged around $\nu = 1/2$ (and also $\nu = 1/4$), that are most naturally interpreted as the cyclotron resonance of composite fermions.

Impurities in mesoscopic Luttinger liquids

W. Metzner; U. Schollwöck (Universität München);
V. Meden and K. Schönhammer (Universität Göttingen)

The interaction between electrons in one-dimensional metals leads to Luttinger liquid behavior with several singular properties not present in conventional (Fermi liquid) metals. In particular, the low-energy behavior of Luttinger liquids is dramatically affected by impurities – already the presence of a single static impurity leads to striking effects. Carbon nanotubes enable experimentalists nowadays to analyze systems with a single impurity in an otherwise perfectly clean one-dimensional metal. Theoretically such systems are usually mapped onto an effective field theory, where terms which are expected to be irrelevant in the low-energy limit are neglected. From the field theoretical analysis the following physical picture emerged: As a consequence of the electron-electron interaction the backscattering amplitude V_B generated by the impurity grows at low energy scales, such that the impurity acts as an increasingly high barrier.

This behavior can be traced back to the power-law singularity of the $2k_F$ density response function in a Luttinger liquid. On the other hand, a weak hopping amplitude t_w bridging the ends of two semi-infinite chains scales to zero at low energies. It was hence argued that at low energy scales physical observables always behave as if the impurity would split the one-dimensional system in two pieces with open boundary conditions at the end points, even if the (bare) impurity potential is relatively weak. Here we focus on the local density of states $\rho_j(\omega)$ for lattice sites j close to the impurity and energies ω close to the chemical potential. As a consequence of the effective chain splitting, a universal power-law suppression $\rho_j(\omega) \sim |\omega|^{\alpha_B}$, with a boundary exponent α_B which does not depend on the impurity parameters, was predicted.

Recently functional renormalization group (RG) methods have been developed as a new powerful tool in the theory of interacting Fermi systems. With these techniques the low-energy behavior described by an effective field theory can be computed *ab initio* for a concrete microscopic model, by solving a differential flow equation with the energy scale as the flow parameter. Thereby also the non-universal behavior at intermediate energy scales is obtained. We have applied such a functional RG scheme to a spinless fermion model with nearest neighbor interactions on a chain (see Fig. 48), and a single site or hopping impurity.

Figure 48: *Spinless fermion model with nearest neighbor hopping and nearest neighbor interaction.*

The flow equations are *non-perturbative* in the impurity strength while perturbative in the electron-electron interaction. We treat the full functional form of the renormalized impurity potential as generated by the flow, instead of replacing it approximately by the scattering amplitudes at the Fermi level. Computing the local density of states near the impurity we have confirmed the universality of the effective boundary behavior. However, it turned out that very large systems (10^4–10^5 sites) are required to reach the universal regime for intermediate impurity and interaction parameters. Our functional RG results have been checked against exact density-matrix renormalization group (DMRG) data for systems with up to $N = 768$ sites.

The one-dimensional lattice model of spinless fermions with nearest neighbor hopping amplitude $t = -1$ and nearest neighbor interaction U is given by

$$H = -\sum_{j}\left(c_j^{\dagger}c_{j+1} + c_{j+1}^{\dagger}c_j\right) + U\sum_{j} n_j n_{j+1}, \quad (16)$$

in standard second-quantized notation. We consider the half-filled case (fermion density one half) where the model is known to be a Luttinger liquid for all positive $U < 2$. This model is either complemented by a site impurity potential $H_s = Vn_{j_0}$ or provided with a hopping impurity $H_h = t_w(c_{j_0}^{\dagger}c_{j_0+1} + \text{h.c.})$ on one of its bonds.

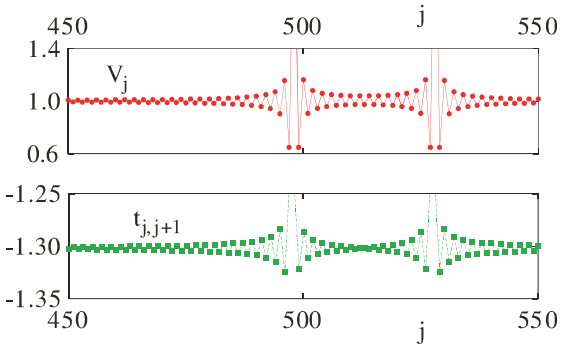

Figure 49: *Effective impurity potential V_j and effective hopping amplitude $t_{j,j+1}$ for a site impurity.*

We have numerically integrated the functional RG equations for finite systems with up to $N = 2^{15} = 32768$ lattice sites. Figure 49 shows typical results for the renormalized effective potential V_j and for the effective hopping amplitude $t_{j,j+1}$ for the case of a site impurity. Both the effective potential and hopping exhibit slowly decaying Friedel oscillations.

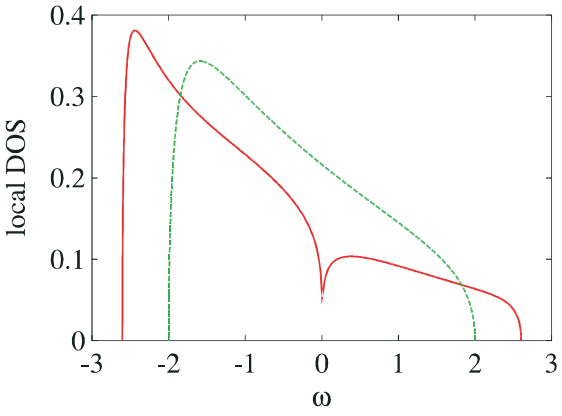

Figure 50: *Local density of states near a site impurity ($V = 1.5$) as a function of the energy ω; red curve: interaction $U = 1$, green curve: non-interacting case ($U = 0$).*

In Fig. 50 the density of states near the impurity, $\rho_{j_0-1}(\omega)$, is presented for a site impurity. The data show a suppression of spectral weight for $|\omega| \to 0$ in the interacting system, as expected. Instead of trying to fit a power-law to the energy dependence of $\rho_{j_0-1}(\omega)$, it is easier to analyze the finite size scaling of the spectral weight at the chemical potential, that is $\rho_{j_0-1}(0)$, which is expected to obey the same power-law as a function of the system size N for sufficiently large N.

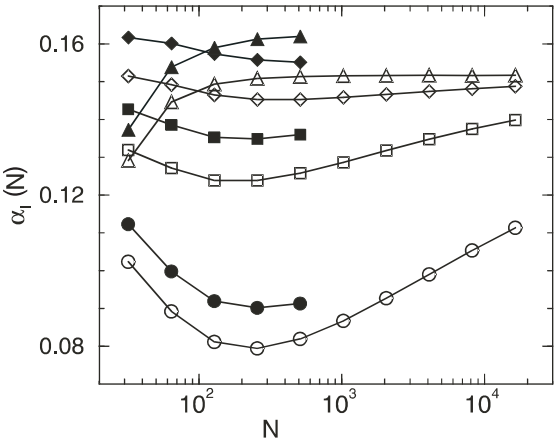

Figure 51: *Exponent $\alpha_I(N)$ as a function of N for $U = 0.5$ and different impurity strengths V: $V = 1$ (circles), $V = 2$ (squares), $V = 4$ (diamonds), and $V = \infty$ (triangles). The filled symbols are DMRG data and the open ones are results from the functional RG.*

In Fig. 51 we show results for the negative logarithmic derivative $\alpha_I(N)$ of the spectral weight as a function of N for $U = 0.5$ and different impurity strengths V, as obtained from the functional RG and from the DMRG. If the spectral weight decays for $N \to \infty$ as a power-law, $\alpha_I(N)$ should converge to the respective exponent. For comparison we also calculated $\alpha_B(N)$ for the lattice site next to a boundary ($V = \infty$). The DMRG and RG data are parallel to each other, which confirms that our fermionic RG captures the essential physics. For $V = \infty$ both methods produce the expected power-law behavior with boundary exponents α_B^{DMRG} and α_B^{RG}, respectively. $\alpha_B^{\mathrm{DMRG}}(N = 512)$ agrees up

to 1% with the exact exponent $\alpha_B^{ex} \approx 0.1609$ (known from a Bethe ansatz solution), while $\alpha_B^{RG}(N = 16384)$ deviates by roughly 6%. The RG curves for finite V suggest that for $N \to \infty$ the $\alpha_I^{RG}(N)$ converge to the universal (V independent) exponent α_B^{RG}. This is in agreement with the field theoretical prediction. However, even for fairly strong impurities ($V = 4$) extremely large systems ($N = 10^4$–10^5) are needed to exclude non-universal (V-dependent) asymptotic behavior with some certainty. Solely relying on DMRG data for a few hundred lattice sites would give no definite result.

In summary, by solving a functional flow equation we have shown that in a one-dimensional lattice electron system with Luttinger liquid behavior an impurity makes observables at low energy scales behave as if the chain is split in two parts with open boundary conditions at the end points. Our functional RG is non-perturbative in the impurity strength and captures also the non-universal behavior at intermediate energy scales. Long-range oscillations in the effective impurity potential provide a simple real-space picture of the splitting mechanism. For realistic parameters very large systems are needed to reach the asymptotic open chain regime. Hence only special mesoscopic systems, such as very long carbon nanotubes, are suitable for experimentally observing the impurity-induced asymptotic open boundary physics. Our method can easily be generalized to the case of several impurities such that also resonance phenomena can be studied.

Scanning tunneling spectroscopy of single Kondo impurities

N. Knorr, M.A. Schneider, L. Diekhöner, P. Wahl, L. Vitali, and K. Kern

The Kondo problem is one of the most widely studied many-body phenomena in physics which deals with the electronic interaction of magnetic impurities with the electron system of a non-magnetic host. Although the 'Kondo effect', i.e., the resistance minimum of metals with magnetic impurities at low temperature is known since the 1930s and theoretically understood since the work of J. Kondo in the 1960s it remains to be an appealing system to theorists and experimentalists alike due to its relevance to other many-body phenomena like high-T_c superconductivity. Recently a new class of experiments has emerged that use the Scanning Tunneling Microscope (STM) to probe the Kondo state of single magnetic atoms adsorbed on metallic surfaces or even carbon nanotubes [J. Li *et al.*, Physical Review Letters **80**, 2893 (1998); V. Madhavan *et al.*, Science **280**, 567 (1998); T.W. Odom *et al.*, Science **290**, 1549 (2000)].

The STM offers an unparalleled insight into the morphological and electronic structure of surfaces and adsorbates on surfaces on the atomic scale. By Scanning Tunneling Spectroscopy (STS), i.e., measuring the differential conductance of the tunneling junction as function of bias voltage and tip position, the local density of states (LDOS) of a molecule or atom adsorbed on a surface can be measured. However, for a correct interpretation of the spectra thus obtained a clear experimental and theoretical understanding of the electronic states involved in the tunneling process has to be achieved. We have demonstrated by local spectroscopy of Co atoms on Cu substrates that the interaction between the magnetic impurities and different electronic states of the substrate can be individually identified.

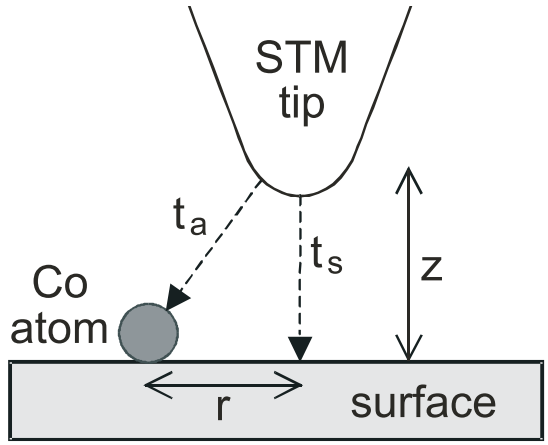

Figure 52: *Principle of probing a (magnetic) adatom with STM. The tip coordinates are given by (r, z). The electron transmission via the direct channel t_a and via the indirect channel t_s contribute to the STM current.*

Our experimental approach is sketched in Fig. 52: the tip of an STM is positioned with sub-pm precision on or near the adsorbate atom and the differential conductance dI/dV of the tunneling junction is recorded as function of tunneling bias. In this situation there are a number of possible channels contributing to the tunneling current that can be classified as the direct channel t_a, i.e., tunneling 'through' the adsorbate, and indirect channels t_s, i.e., tunneling into the electron system of the substrate.

To determine the relative weight of the tunneling channel via the adsorbate resonance and the substrate electronic states we performed tunneling spectroscopy on single Co atoms adsorbed on Cu(111) and Cu(100). STM topographies of these two systems are shown in Fig. 53. In both systems the Co adatoms appear as protrusions (white). Characteristic of the Cu(111) system is the appearance of Friedel oscillations in the surface state electron density which are imaged as circular waves around the adsorbate scatterer.

The tunneling spectra taken directly on the Co atom on the two substrates is shown in Fig. 54(a). The energetically narrow feature at the Fermi energy results from the formation of a Kondo resonance at low temperatures. Although the spectra of Co on Cu(100) and Co on Cu(111) look quite different they belong to the Fano family of line shapes.

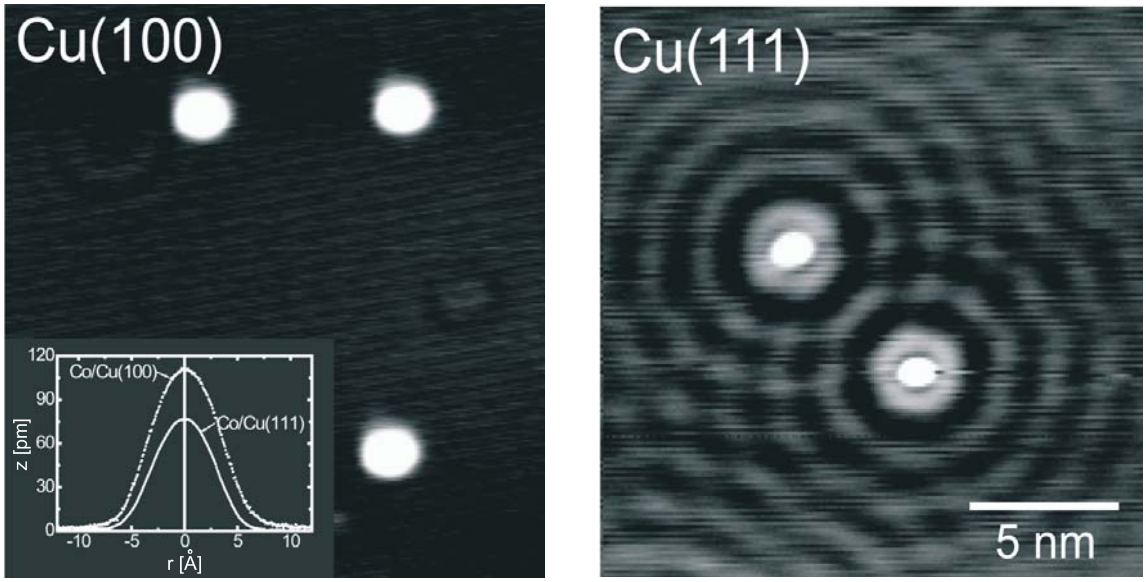

Figure 53: *Constant current STM images (–50 mV bias, I = 2 nA) of Co atoms (bright) on the Cu(100) and the Cu(111) surface. The Friedel oscillations of the surface state electrons on the Cu(111) surface can be seen to extend up to 10 nm. The inset compares the apparent height of the adsorbates for typical STM conditions.*

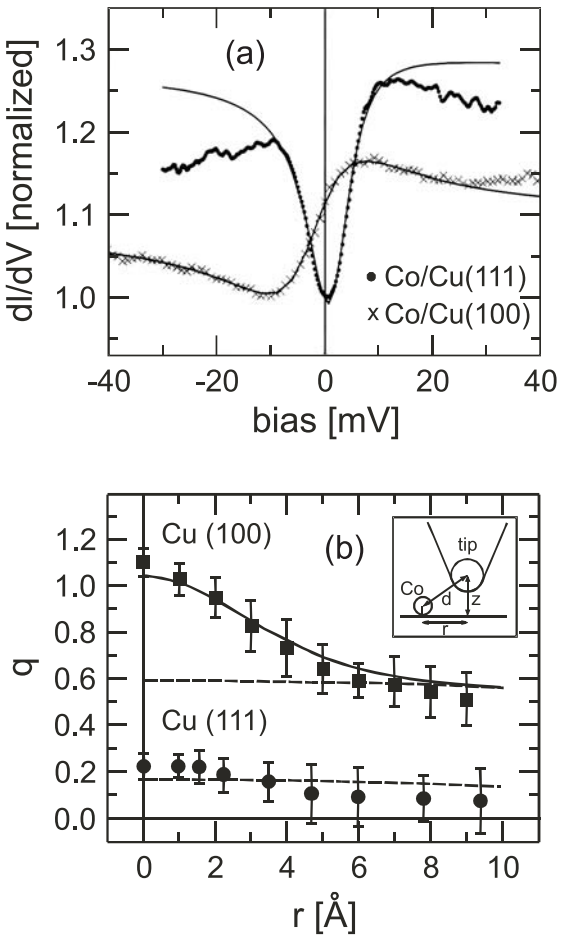

Figure 54: *(a) On atom differential conductance (dI/dV) spectra for Co/Cu(100) and Co/Cu(111). The solid lines are fits of a Fano line to the experimental data. (b) The Fano line shape parameter q as a function of lateral distance r between tip and adatom. The solid line is a fit to the Co/Cu(100) data taking into account the r-dependence of the direct channel t_a. The dashed lines are obtained from calculations with $t_a = 0$.*

This type of line shape was found to be characteristic of all single atom Kondo resonance spectra and was successfully explained by theory [M. Plihal *et al.*, Physical Review B **63**, 085404 (2001)]. The detailed spectral information contained allows to determine some of the underlying physics. Only two parameter determine the actual shape, one is the Kondo temperature T_K, i.e., the width of the resonance and the other is a parameter q that contains information on the weight of contributing tunneling channels. Both parameters reveal interesting physics. The Kondo temperature of Co adsorbed on Cu(111) (54 K) is lower than that for Co on Cu(100) (96K) and both are lower than that found for a diluted alloy of Co in bulk Cu (≈ 500 K). The T_K of a magnetic impurity system depends exponentionally on the product of exchange coupling constant and density of states:

$$T_K = e^{-1/(2J\rho)} \sim e^{-1/n},$$

where J is the exchange coupling integral and ρ is the density of states at the Fermi energy. The observed behavior of T_K can be explained by assuming the product $(J\rho)$ to be proportional to the number of nearest neighbors n of the Co atom which is $n = 3$ in the case of Co on Cu(111), $n = 4$ in the case of Cu(100), and $n = 12$ for a bulk alloy.

The symmetry of the line shapes is governed by the Fano parameter q. A q-value close to zero results from a symmetric line shape and signifies a small contribution from the direct tunneling channel via the adsorbate resonance. For Co on Cu(111) this q-value is close to zero ($q \approx 0.2$) resulting in a slightly asymmetric curve, whereas Co on Cu(100) has the highest value ($q \approx 1.1$) signifying a higher contribution of the direct tunneling channel. This is experimentally proven by determining the q-value as function of lateral distance r between tip and adatom (Fig. 54(b)). For Co on Cu(111) there is hardly a change in the q-value as function of distance showing that the direct tunneling channel which has to decay with increasing distance plays a minor role indeed. On the other hand there is a clear decrease of the q-value at $r > 6$ Å for Co on Cu(100) showing the decay of the direct tunneling channel.

Superconductivity

The current research focuses on high-T_c materials, superconducting fullerenes and the very recently discovered superconductivity in MgB_2. Surprisingly a single optical phonon mode seems to provide the dominant interaction in the two-band superconductor MgB_2. While the traditional concepts of electron-phonon mediated superconductivity seem to apply in the case of MgB_2, questions are raised for the intercalated fullerenes, which exhibit particularly high transition temperatures up to 117 K in $C_{60}{\cdot}2\,CHBr_3$. Neutron scattering experiments using tiny mm^3-size single crystals of $Tl_2Ba_2CuO_{6+\delta}$ provided first evidence for the resonance mode in the spin excitation spectrum of a single layer material. A novel high-resolution neutron spectrometer was successfully tested. Further progress in this field relies on the controlled growth of single crystals of complex multilayer cuprate structures as well as on the synthesis of new superconducting compounds.

Superconductivity and specific heat in MgB_2

Y. Kong, O.V. Dolgov, O. Jepsen, O.K. Andersen, and J. Kortus;
A.A. Golubov (University of Twente, The Netherlands); B.J. Gibson, K. Ahn, and R.K. Kremer

The discovery of superconductivity at 39 K in MgB_2 immediately raised the question if such a relatively high critical temperature could result from the conventional electron-phonon coupling or whether more exotic mechanisms are involved like in the copper-oxide high-T_c superconductors.

In order to answer this question we calculated the electronic structure, the phonon spectrum, and the electron-phonon (e-ph) interaction using the linear-response theory within the full-potential LMTO density functional method. The crystal structure of MgB_2 is hexagonal with graphite-like boron layers stacked on top with Mg in between.

The electronic structure near and below the Fermi level consists of two B p_z π-bands and three quasi-2D B–B bonding σ-bands. The σ and π bands do not hybridize when $k_z = 0$ and π/c. The π-bands lie lower with respect to the σ-bands than in graphite and have more k_z-dispersion due to the influence of Mg, the on-top stacking, and the smaller c/a-ratio. This causes the presence of $p_{\sigma l} = 0.056$ light and $p_{\sigma h} = 0.117$ heavy holes near the doubly-degenerate top along ΓA of the σ-bands. For the density of states at $\varepsilon_F \equiv 0$, we find: $N(0) = N_{\sigma l}(0) + N_{\sigma h}(0) + N_{\pi}(0) = 0.048 + 0.102 + 0.205 = 0.355$ states / (MgB_2·eV·spin). Along ΓA there is a doubly-degenerate σ-band of symmetry E which is slightly above the Fermi level and its eigenvectors are given in the two insets at the bottom of Fig. 55. The corresponding Fermi surface sheets are warped cylinders.

The phonon dispersions $\omega_m(\mathbf{q})$ and density of states $F(\omega)$ are shown in Fig. 55. The agreement between our $F(\omega)$ and those obtained from inelastic neutron scattering is excellent; our peaks at 260 and 730 cm^{-1} (32 and 90 meV) are seen in the experiments at 32 and 88 meV. For the frequencies of the optical Γ-modes we get: 335 cm^{-1} (E_{1u}), 401 cm^{-1} (A_{2u}), 585 cm^{-1} (E_{2g}), and 692 cm^{-1} (B_{1g}). The all-important E_{2g} modes are doubly degenerate optical B–B bond-stretching modes (obs).

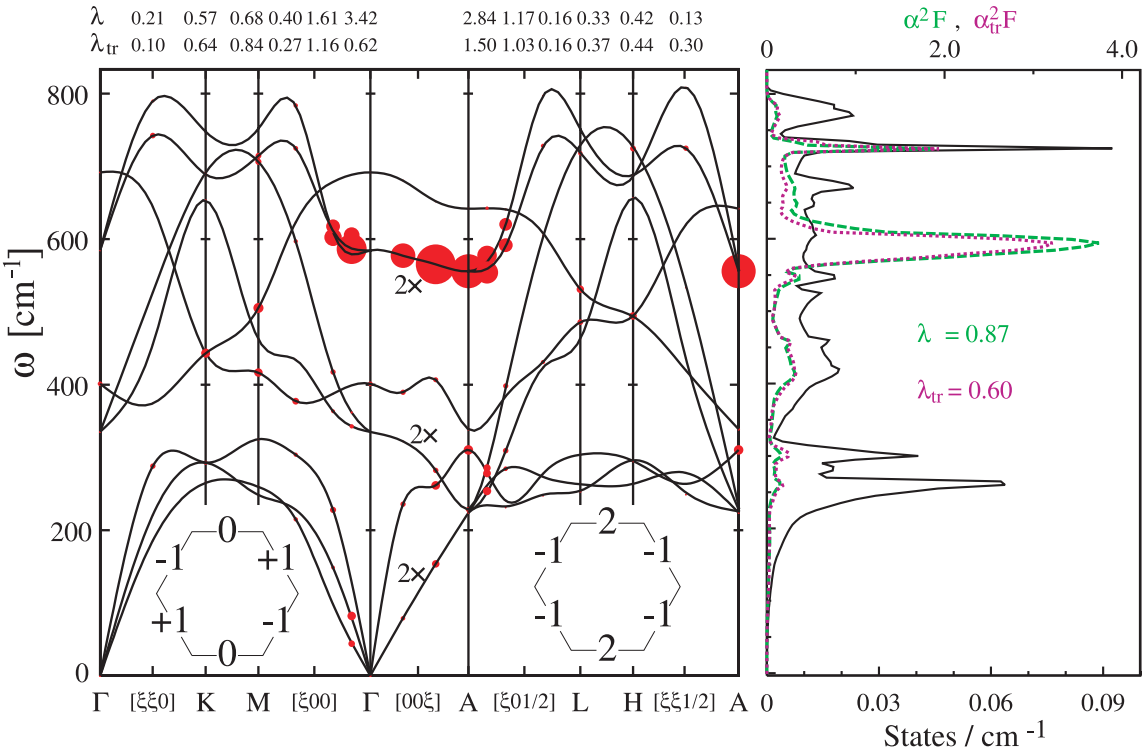

Figure 55: *Left: Calculated phonon dispersion curves in MgB_2. The area of a circle is proportional to the contribution to the electron-phonon coupling constant, λ. The insets at the bottom show the two ΓA E eigenvectors (un-normalized), which apply to the holes at the top of the σ-bands (bond-orbital coefficients) as well as to the optical bond-stretching phonons (relative change of bond lengths). Right: F(ω) (black and bottom scale), $\alpha^2(\omega)F(\omega)$ (green) and $\alpha^2_{tr}(\omega)F(\omega)$ (purple).*

Close to ΓA, they have exactly the same symmetry and similar dispersions as the light and heavy σ-holes, although with the opposite signs. The E eigenfunctions shown at the bottom of Fig. 55 now refer to displacement patterns, e.g., $\{-1,0,1\}$ has one bond shortened, another bond stretched by the same amount, and the third bond unchanged. These E displacement patterns will obviously modulate the electronic bond energy, such as to split the light- and heavy-hole bands. It was judged that the corresponding electron-phonon (e-ph) matrix element, $g_{\sigma,\mathrm{obs}}$, will be the dominating one.

We then calculated the e-ph interaction which is represented by the Eliashberg spectral function $\alpha^2(\omega)F(\omega)$ which for superconductivity as well as for transport is shown in the right panel of Fig.55. The dominance of the σ–σ coupling via the optical bond-stretching mode is clearly seen in the left panel of the figure, where the area of a red circle is proportional to the contribution to the electron-phonon coupling constant from the particular mode. This gives rise to the huge peak in the two Eliashberg functions around $\omega_{\mathrm{obs}} = 590\,\mathrm{cm}^{-1} = 73\,\mathrm{meV}$. The total $\lambda = \lambda_\sigma + \lambda_\pi = 0.62 + 0.25 = 0.87$ is moderately large.

We first assumed isotropic pairing and obtained a T_c of 40 K by solving the Eliashberg equations for $\mu^* = 0.10$ which is at the low end of what is found for simple *sp* metals. The temperature dependence of the specific dc-resistivity calculated with the standard Bloch-Grüneisen expression is nearly isotropic and in accord with recent measurements on dense wires over the entire temperature range from 40 to 300 K.

We finally solved the Eliashberg equations for a number of temperatures from 0 K to above T_c for a fixed μ^* in the superconducting as well as in the normal state. From this we calculate the difference in specific heat in the two states which is compared to our original measurements and to some more recent measurements on high quality samples in Fig. 56. It may be seen that in the calculations the specific heat jump is considerably larger at T_c than in the experiments and also that the experiments show larger heat capacity at low temperatures.

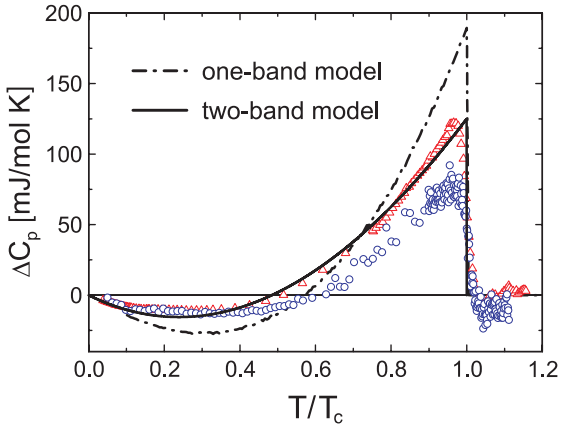

Figure 56: *Experimental data of the heat capacity difference $\Delta C_p = C_p(0\,\mathrm{Tesla}) - C_p(9\,\mathrm{Tesla})$ measured by us (○) and by Bouquet et al. [Physical Review Letters* **87***, 047001 (2001)] (△). The dash-dotted line is the theoretical result of the one-band model and the thick solid line corresponds to the two-band model from the solution of the Eliashberg equations. The two-band model reproduces much better the specific heat jump as well as the low temperature behavior.*

We therefore relaxed the assumption of an isotropic one-band model and instead considered a two-band model with the possibility of different gaps on the σ and π Fermi surface sheets. The reason for discarding this model originally was the experimental fact that a two orders of magnitude change in scattering rate changed T_c by merely ≈ 2 K. With interband scattering and a two-band model T_c would change much more. However, if the interband scattering is small and only intraband scattering is responsible for the change in scattering rate then a small change of T_c would be possible.

We therefore recalculated the Eliashberg functions allowing for two different order parameters for the σ and π-electrons. The corresponding Eliashberg functions are shown in Fig. 57. As expected the most significant contribution comes from the coupling of the bond-stretching phonon modes to the σ-band.

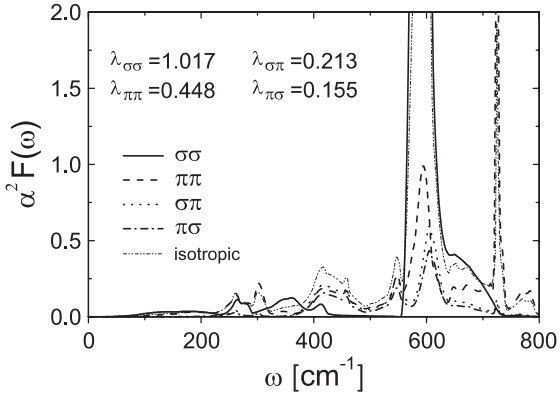

Figure 57: *The four superconducting Eliashberg functions $\alpha^2 F(\omega)$ obtained from first-principles calculations for the effective two-band model are compared with the isotropic Eliashberg function for the one-band model. The coupling constant of the isotropic one-band model has a value of $\lambda_{iso} = 0.87$.*

Besides the spectral functions we need the information of the Coulomb matrix element μ_{ij}. With the help of the wavefunctions from our first-principles calculations we can approximately calculate the ratio of the μ-matrix. The ratio between σσ, ππ and σπ were 2.23/2.48/1. This allows one to express μ^*_{ij} by these ratios and one single free parameter which is fixed to get the experimental T_c of 39.4 K from the solution of the Eliashberg equations.

Using our calculated Eliashberg functions on the imaginary (Matsubara) axis together with the above matrix μ^*_{ij} we obtain the gap values $\Delta_\sigma = \lim_{T\to 0} \Delta_\sigma(i\pi T) \simeq 7.1$ meV, and $\Delta_\pi \simeq 2.7$ meV, which corresponds to $2\Delta_\sigma/k_B T_c = 4.18$ and $2\Delta_\pi/k_B T_c = 1.59$ and

which are in good agreement with several experiments. We solved the two-band Eliashberg equations as function of temperature and calculated the difference between the specific heat in the superconducting state and the normal state which is shown in Fig. 56. It may be seen that not only the specific heat jump at T_c but also the low temperature behavior is in much better agreement with experiments than the results of the one-band model.

The superconductor MgB_2 at high pressures

I. Loa, K. Kunc, K. Syassen, R.K. Kremer, and K. Ahn

The report of Nagamatsu *et al.* [Nature **410**, 63 (2001)] on superconductivity in MgB_2 with a relatively high critical temperature of $T_c = 39$ K has triggered great interest in this compound. MgB_2 has a layered hexagonal crystal structure of the AlB_2 type which can be viewed as a boron honeycomb framework (graphite-like sheets) intercalated with Mg. On the basis of BCS theory, the high critical temperature was attributed to a fortunate combination of strong bonding, 'reasonable' electronic density of states at the Fermi level, and high phonon frequencies. This view of phonon-mediated superconductivity is supported by the observation of a sizable boron isotope effect. Stimulating for our work was in particular a report that T_c decreases with increasing pressure. This was confirmed by a number of investigations, including our own ($dT_c/dP = -1.4$ K/GPa).

We have studied the effect of high pressure on structural, electronic, and lattice dynamical properties of MgB_2 by first-principles calculations and Raman spectroscopy [I. Loa *et al.*, Solid State Communications **118**, 279 (2001); K. Kunc *et al.*, Journal of Physics: Condensed Matter **13**, 9945 (2001)]. The main motivation was to find out whether the decrease of T_c under pressure is predominantly due phonon frequency shifts or to changes in the electronic density of states near the Fermi level.

Total-energy calculations based on density functional theory yield information on the structural changes of MgB_2 under pressure. We predicted a bulk modulus of $B_0 = 139$ GPa and a small pressure-induced decrease of the crystallographic c/a ratio which later on turned out to be in good agreement with experimental data.

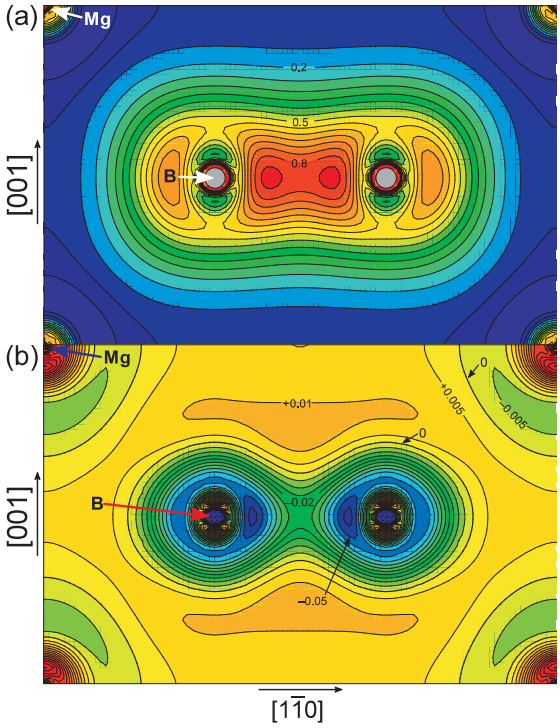

Figure 58: *(a) Charge density distribution of MgB_2 in the (110) plane with contour lines at intervals of 0.05 e/Å^3. (b) Change of the charge density distribution* ρ *at 20 GPa compared to 0 GPa. Contour lines are at intervals of 0.005 e/Å^3.*

With regard to bonding properties, Fig. 58(a) shows the charge density distribution in the (110) plane of MgB_2. One can clearly see

the covalent B–B bonds. In addition, a significant amount of charge in the interstitial indicates metallic-type bonding between the Mg and B sheets. Figure 58(b) shows the difference between the charge densities at 20 and 0 GPa. There occurs a small transfer of charge from the region between the B atoms into the nearby interstitial region which can be regarded as a transfer from σ- to π-type bonds. The main characteristics of the bonding in MgB_2, however, remain unchanged at pressures up to 20 GPa.

Strong electron-phonon coupling, which is required for phonon-mediated superconductivity, was found for the E_{2g} phonon branch along the Γ-A direction in a number of calculations [Y. Kong *et al.*, Physical Review B **64**, 020501(R) (2001)]. These studies reported frequencies of the Raman active $E_{2g}(\Gamma)$ phonon between 486 and 665 cm^{-1}. So far, this phonon mode has not been identified unambiguously by neutron inelastic scattering or in Raman experiments. Due to the uncertainties of the experimental data theoretical methods gain in importance. The immediate interest in the calculation of the shifts of phonon frequencies as a function of pressure is in the context of interpreting the pressure dependence of T_c. Furthermore, they can be useful for the identification of spectral features in Raman spectra.

Figure 59 summarizes the results of our frozen phonon calculations. A striking feature of the $E_{2g}(\Gamma)$ mode is its strong anharmonicity; it is larger by an *order of magnitude* than that of the $B_{1g}(\Gamma)$ mode. This is equally true for the corresponding mode $E_{2u}(A)$ at the Brillouin zone boundary and, apparently, holds for the whole branch $E_{2g}(\Gamma)$–$E_{2u}(A)$. Based on results of Yildirim *et al.* [Physical Review Letters **87**, 037001 (2001)] we estimate a 9 to 13% upshift of the $E_{2g}(\Gamma)$-frequency due to anharmonicity. Similarly, the shift in $E_{2u}(A)$ can be estimated at 7 to 10% (see the shaded areas in Fig. 59).

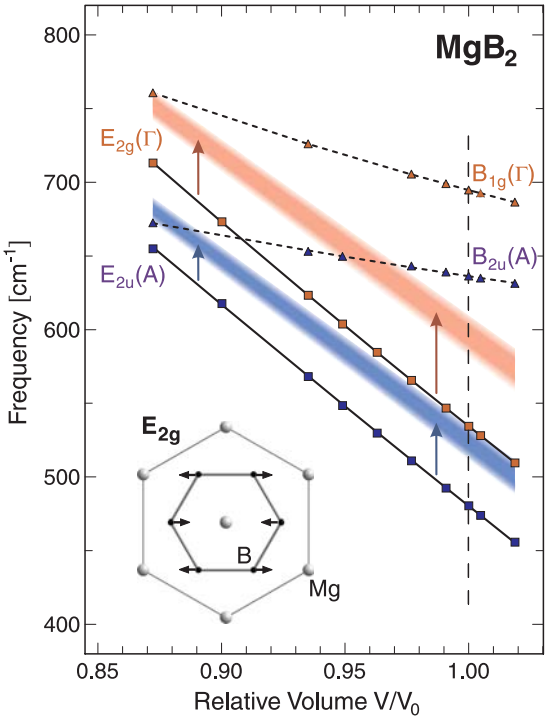

Figure 59: *Calculated harmonic frequencies of the two highest-energy phonon modes at* Γ *and* A *in the Brillouin zone of MgB_2 as a function of relative volume. The shaded areas represent estimates for the $E_{2g}(\Gamma)$ and $E_{2u}(A)$ frequencies taking into account anharmonic corrections.*

The variations of phonon frequencies ω with volume are described by the mode Grüneisen parameter $\gamma_0 = -[d\ln\omega / d\ln V]_{V_0}$. For the calculated *harmonic* phonon frequencies of the $E_{2g}(\Gamma)$ and the $E_{2u}(A)$ we obtain Grüneisen parameters of 2.5 and 2.8, respectively. Taking into account the corrections for anharmonicity these values reduce to $\gamma_0 = 2.0$–2.2 and $\gamma_0 = 2.3$–2.5, respectively.

On the basis of the McMillan expression for T_c we estimate $dT_c/dP \approx -1.8$ K/GPa taking into account the calculated changes in phonon frequency and electronic density of states [K. Kunc *et al.*, Journal of Physics: Condensed Matter **13**, 9945 (2001)]. Experimental values of dT_c/dP in the range –0.7 to –2.0 K/GPa have been reported. This large spread in the data was attributed to differences in the samples studied and to various degrees of non-hydrostatic

stresses. Our estimate of the pressure dependence of T_c is close to the upper limit of the experimental values. This, however, is not surprising because we used the large Grüneisen parameter of the $E_{2g}(\Gamma)$–$E_{2u}(A)$ phonon branch. Non-negligible contributions from other vibrational modes with smaller pressure dependencies are expected to reduce the pressure shift of T_c compared to our estimate.

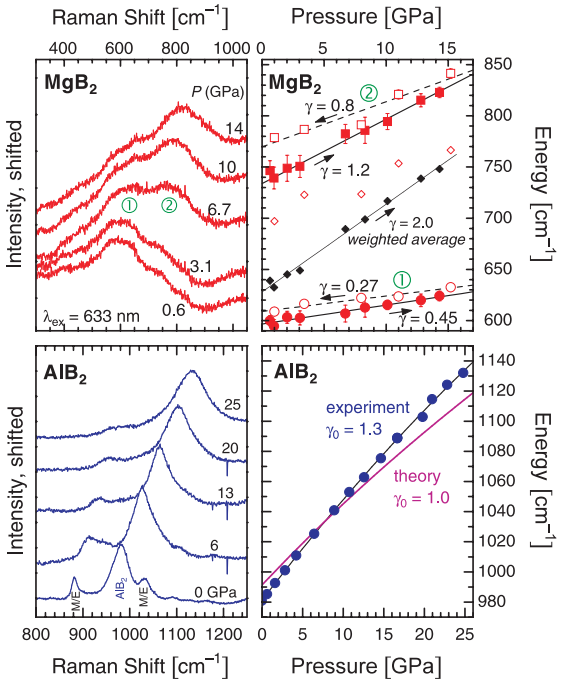

Figure 60: *Raman spectra for increasing pressures ($T = 300$ K) and peak positions as a function of pressure for MgB_2 (top) and AlB_2 (bottom). Solid and open symbols refer to data measured at increasing and decreasing pressures, respectively. M/E refers to the methanol-ethanol pressure medium.*

We have searched for experimental confirmation of the calculated results. Figure 60 shows Raman spectra of MgB_2 recorded at increasing pressures in the range 0–14 GPa. The 0.6 GPa spectrum, exhibiting a broad peak near 600 cm^{-1} with a high-energy shoulder, is representative for the ambient-pressure Raman spectra of numerous samples we have investigated. It is also quite similar to ambient-pressure Raman spectra reported by other authors who have attributed the 600 cm^{-1} feature to the Raman active E_{2g} zone-center phonon. With increasing pressure the shoulder gains intensity and the spectrum exhibits two clearly resolved peaks. The enhanced intensity of the higher-energy peak persisted upon pressure release until the cell was opened and the sample was exposed to air. Neither of the observed peaks can be attributed to the Raman-active $E_{2g}(\Gamma)$ mode nor to the silent $B_{1g}(\Gamma)$ mode. The observed pressure-induced peak shifts translate to mode Grüneisen parameters of $\gamma_1 = 0.27$–0.45 and $\gamma_2 = 0.8$–1.2 for peaks (1) and (2), respectively. Hence, the calculated Grüneisen parameter of the $E_{2g}(\Gamma)$ phonon and the experimental value for peak (1) differ by a factor of ≈ 6. Similarly, the experimental data for peak (2) and the calculated values for the $E_{2g}(\Gamma)$ mode disagree. Thus, the interpretation of Raman features of MgB_2 remains under debate.

Among the diborides, the Raman problem appears to be specific to MgB_2. For instance, in the case of AlB_2 we observe a well-defined Raman peak and the measured pressure dependence of the phonon energy is in rather good agreement with the calculation for the $E_{2g}(\Gamma)$ mode (Fig. 60). It should be noted that samples of AlB_2 exhibit an Al deficiency of $\approx 10\%$ which was not taken into account in the calculation. Nevertheless, the agreement between experimental and calculated results for AlB_2 lends additional support to the calculated phonon properties for MgB_2.

To conclude, the results summarized here indicate a dominant role of the phonon spectrum with regard to the pressure dependence of T_c. Changes in the electronic density of states near the Fermi level are only of secondary importance.

Two-gap superconductivity in MgB_2

P. Szabó, P. Samuely, and J. Kačmarčík (Institute of Experimental Physics, Kosice and MPI-FKF and CNRS, Grenoble); A.G.M. Jansen (MPI-FKF and CNRS, Grenoble); T. Klein, J. Marcus, D. Fruchart, and S. Miraglia (CNRS, Grenoble); C. Marcenat (CEA-DRFMC, Grenoble)

In the months following the surprising discovery of superconductivity in MgB_2 early 2001, most of its superconducting properties have been investigated extensively. In contrast to the cuprates, the first tunneling spectroscopy experiments have shown that this system is a *s*-wave superconductor and the isotope effects point towards the electron-phonon interaction for the pairing mechanism. By means of Andreev reflection experiments on point contacts with MgB_2, we have found evidence for the existence of two distinct superconducting energy gaps. This gives experimental support for the multiband model of superconductivity recently proposed by Liu *et al.* [Physical Review Letters **87**, 87005 (2001)] thus showing that MgB_2 belongs to an original class of superconductors in which two distinct 2D and 3D Fermi surfaces contribute to superconductivity.

The electrical transport in ballistic contacts between a normal (N) and a superconducting (S) electrode can be described by the model developed by Blonder, Tinkham and Klapwijk (BTK) which treats the transparency across the N/S interface with a single Z parameter: from a pure conducting interface (Z = 0) where the Andreev reflection dominates up to the well known insulating barrier, i.e., the Giaever tunneling case with $Z \gg 1$. The analysis of the current-voltage characteristics of S/N contacts with the BTK model provides direct spectroscopic information about the superconducting energy gap.

Point contact measurements have been performed on polycrystalline MgB_2 samples with $T_c = 39.3$ K and $\Delta T_c = 0.6$ K. A standard lock-in technique at 400 Hz was used to measure the differential resistance as a function of applied voltage on the point contacts. The microconstrictions were prepared by pressing a copper tip (formed by electrochemical etching) on the freshly polished surface of the superconductor yielding contact resistances from 100 Ω down to 5 Ω.

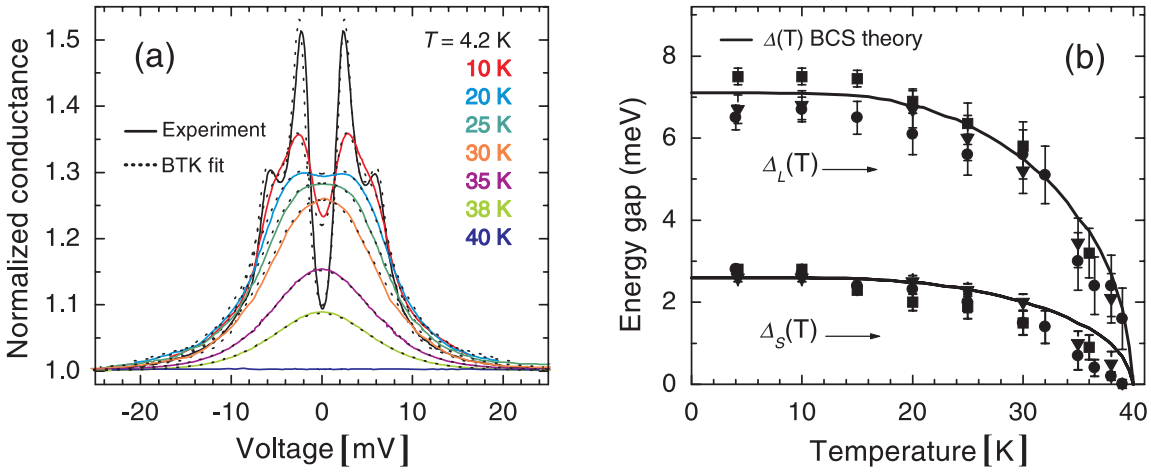

Figure 61: *(a) Differential conductances of a Cu-MgB_2 point contact measured (full lines) and fitted (dotted lines) for the thermally smeared BTK model at indicated temperatures with fitting parameters α = 0.71 and Z = 0.52 ± 0.02 for all temperatures. (b) Temperature dependencies of small and large energy gap ($\Delta_S(T)$ and $\Delta_L(T)$) determined from the fitting on three different point contacts as displayed with three corresponding different symbols. Full lines represent BCS predictions.*

Figure 61(a) shows a typical example of the normalized conductance versus voltage for a Cu/MgB_2 contact at different temperatures below the critical temperature. The two-gap structure is clearly revealed by the two maxima placed symmetrically around zero-bias voltage. The conductance curves could be fitted by the sum of two BTK conductances, $\alpha\sigma_S + (1-\alpha)\sigma_L$, with a weight factor α between the small- and large-gap contributions. The two-gap features are reproduced in the spectra of other contacts. However, the relative weight of the two structures changed from contact to contact with α varying from 10 to 90%. The scattering in α is probably related to different crystallographic orientations at the different microconstrictions.

The dotted lines in Fig. 61(a) show the fit to the sum of two BTK contributions. The temperature evolution of the spectra could be described without changing the transparency coefficient Z and the weight factor α. It is evident from the deduced energy gaps in Fig. 61(b) that both gaps are closing near the same critical temperature. Averaged over different contacts we obtained $\Delta_L = 6.8 \pm 0.3$ meV and $\Delta_S = 2.8 \pm 0.1$ meV, yielding BCS ratios $2\Delta_L/k_B T_c \simeq 4.1$ and $2\Delta_S/k_B T_c \simeq 1.7$. These findings are in very good agreement with the predictions of the multigap superconductivity in MgB_2 based on density functional calculations of the electron-phonon coupling [A. Liu *et al.*, Physical Review Letters **87**, 87005 (2001)]. From these calculations follows that the large-gap results from the 2D part of the Fermi surface with a gap ratio larger that the BCS value 3.53, whereas the small-gap results from the 3D part with a ratio smaller than 3.53.

In Fig. 62 we show the magnetic field dependence of the point contact spectra. The small-gap structure disappears already in a field of 1–2 T. This magnetic field induced suppression of the small-gap structure can be observed at temperatures close to T_c and gives another indication for the existence of two superconducting gaps near to a common critical temperature. The large-gap structure disappears in much higher fields around 15 T.

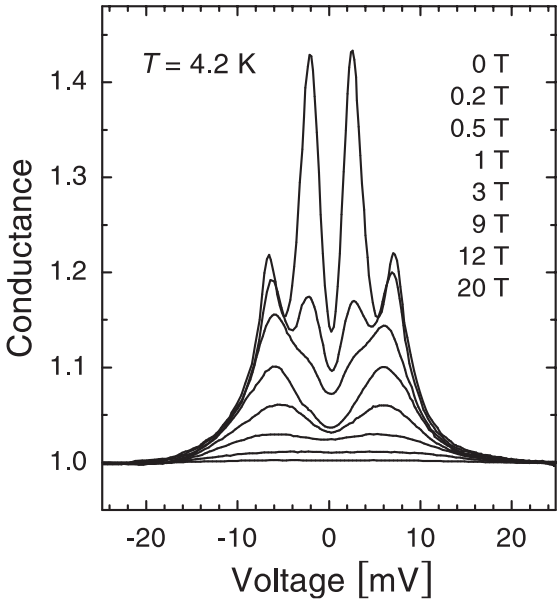

Figure 62: *Differential conductance of Cu-MgB_2 point contacts for different magnetic fields showing the gap suppression at different field ranges for small- and large-gap structures. The data have been obtained from the data sets of two different contacts, obtained at fields above and below 9 T.*

The existence of two superconducting gaps as observed in the point contact spectra on MgB_2 is supported by similar findings using other experimental techniques like Raman scattering, specific heat, and penetration depth measurements. Although experiments on MgB_2 point to a rather classical BCS superconductor with a phonon-mediated pairing mechanism, the existence of a more complex gap structure related to the electron-phonon coupling between different parts of the Fermi surface makes this compound unique among the BCS superconductors.

Enhancements of the superconducting transition temperature within the two-band model

A. Bussmann-Holder

The two-band model as introduced by Suhl, Matthias and Walker [Suhl *et al.*, Physical Review Letters **3**, 551 (1959)] accounts for multiple energy bands in the vicinity of the Fermi energy which could contribute to electron pairing in superconducting systems. Their assumption that pairing might occur in various energy bands that are located in the vicinity of the Fermi energy implied that interband interactions between those bands take place in order to assure a homogeneous superconducting state. Interestingly, they observed that a two-order parameter scenario leads to an enhancement of the superconducting transition temperature as compared to a single-band model. Here the effect of the coexistence of a dynamic polaronic lattice distortion with superconductivity on the superconducting transition temperature T_c is investigated. In addition anisotropic pairing and the mixing of *d*- and *s*-wave superconducting order parameters is admitted. In all calculations it is assumed that the pairing interactions within the two bands considered are too weak to induce superconductivity. Thus it is possible to investigate the effect of the interband interactions on anisotropic superconductivity and also to show in how much a polaronic distortion can influence superconductivity. The two band Hamiltonian considered here, in already condensed form, reads:

$$H = H_0 + H_1 + H_2 + H_{12} \tag{17}$$

$$H_0 = \sum_{k_1\sigma} \xi_{k_1} c^+_{k_1\sigma} c_{k_1\sigma} + \sum_{k_2\sigma} \xi_{k_2} d^+_{k_2\sigma} d_{k_2\sigma}$$

$$H_1 = \sum_{k_1 k_1' q} V_1(k_1, k_1') c^+_{k_1+\frac{q}{2}\uparrow} c^+_{-k_1+\frac{q}{2}\downarrow} c_{-k_1'+\frac{q}{2}\downarrow} c_{k_1'+\frac{q}{2}\uparrow}$$

$$H_2 = \sum_{k_2 k_2' q} V_2(k_2, k_2') d^+_{k_2+\frac{q}{2}\uparrow} d^+_{-k_2+\frac{q}{2}\downarrow} d_{-k_2'+\frac{q}{2}\downarrow} d_{k_2'+\frac{q}{2}\uparrow}$$

$$H_{12} = \sum_{k_1 k_2 q} V_{12}(k_1, k_2) \{ c^+_{k_1+\frac{q}{2}\uparrow} c^+_{-k_1+\frac{q}{2}\downarrow} d_{-k_2+\frac{q}{2}\downarrow} d_{k_2+\frac{q}{2}\uparrow} + h.c. \} ,$$

where H_0 is the kinetic energy of the bands $i = 1, 2$ with $\xi_{k_i} = \varepsilon_i + \varepsilon_{k_i} - \mu$. Here ε_i denotes the position of the c- and d-band with creation and annihilation operators c^+, c, d^+, d, respectively, and μ is the chemical potential. The pairing potentials $V_i(k_i, k_i')$ are assumed to be represented in factorized form like $V_i(k_i, k_i') = V_i \varphi_{k_i} \psi_{k_i}$ where $\varphi_{k_i}, \psi_{k_i}$ are cubic harmonics for anisotropic pairing which yields for dimension $d = 2$ and on-site pairing: $\varphi_{k_i} = 1$, $\psi_{k_i} = 1$, extended *s*-wave: $\varphi_{k_i} = \cos(k_x a) + \cos(k_y b) = \gamma_{k_i}$ and *d*-wave: $\varphi_{k_i} = \cos(k_x a) - \cos(k_y b) = \eta_{k_i}$, where a, b are the lattice constants along x and y directions; throughout this paper $a = b$. By performing a BCS mean-field analysis of Eqs. (17) a self-consistent set of coupled gap equations is obtained which has to be solved simultaneously to determine T_c and the temperature dependencies of the gaps. If the interactions V are constants, the resulting gaps are momentum independent. A more interesting case is obtained by assuming the following general momentum dependence of the intraband interactions: $V_i = g_0^{(i)} + g_\gamma^{(i)} \gamma_k \gamma_{k'} + g_\eta^{(i)} \eta_k \eta_{k'}$ where the first term yields onsite pairing, the second extended *s*-wave pairing and the last term *d*-wave pairing. Here it is assumed that V_1 is proportional to g_0 while V_2 is either determined by g_0 or by g_η. In addition the two bands considered are one-dimensional in the case of the *c*-bands while the *d*-related band is two-dimensional with the following dispersion:

$$\varepsilon_{k_2} = -2t \left[\cos(k_x a) + \cos(k_y b) \right] .$$

Throughout the following the values for the intraband interactions are $V_1 = V_2 = 0.01$, where $V_1 = \widetilde{V}_1 N_s$, $V_2 = \widetilde{V}_2 N_d$. Within this scenario the selfconsistent set of equations is solved numerically as function of $V_{12} = \widetilde{V}_{12} \sqrt{N_s N_d}$ where N_s, N_d are the density of states of band 1, 2, respectively. The results are shown in Fig. 63 where

both cases $V_2 \sim g_0$ and $V_2 \sim g_\eta$ are considered. In both cases small values of V_{12} are sufficient to induce superconductivity. With increasing V_{12} dramatic enhancements of T_c are obtained which easily exceed 100 K. Interestingly the *d*-wave component in the two component systems has an additional T_c-increasing factor which increases with increasing interband coupling.

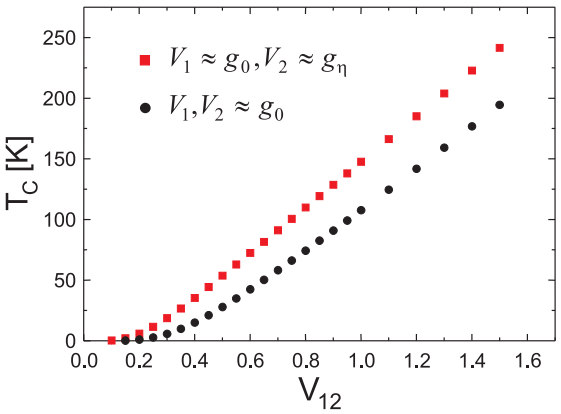

Figure 63: *The dependence of the superconducting transition temperature on the interband coupling V_{12} for the case of both, V_1 and $V_2 \sim g_0$ (circles) and the case where $V_1 \sim g_0$, $V_2 \sim g_\eta$ (squares).*

This finding clearly shows that a mixed order parameter symmetry favors superconductivity, as opposed to two onsite pairing interactions.
In order to determine the possible coexistence of dynamic polaronic lattice distortion with superconductivity it is assumed that for temperatures $T \gg T_c$ a strong coupling of the one-dimensional electronic band to phonons with momentum q dependent energy $\hbar\omega$ takes place. This corresponds to modifying the first part of Eq. (17) as:

$$\overline{H}_0 = \sum_{k_1\sigma} \xi_{k_1} c^+_{k_1\sigma} c_{k_1\sigma} + \sum_q \hbar\omega_q b^+_q b_q + \frac{1}{\sqrt{N}} \sum_{q,\sigma,k_1} g(q)\, c^+_{k_1+q\sigma} c_{k_1\sigma} (b_q + b^+_{-q}). \quad (18)$$

Here b^+, b are phonon creation and annihilation operators and $g(q)$ is the electron-phonon coupling. Following previous work the k_1 related electronic energies are renormalized by the electron phonon coupling as:

$$\widetilde{H}_0 = \sum_{k_1\sigma} (\xi_{k_1} - \Delta^*)\, c^+_{k_1\sigma} c_{k_1\sigma},$$

with $\Delta^* = g(q_0) \frac{2}{\sqrt{N}} \langle b^+_q \rangle \delta_{q,q_0}$, where q_0 is the wave vector which characterizes the width of the polaron induced distortion. Including these modifications of the one dimensional electronic band in the calculation of T_c and considering again the above two cases the results shown in Fig. 64 are obtained. The polaronic band shift Δ^* first increases T_c enormously but then depresses its value to zero with increasing band shift Δ^*. Since the magnitude of Δ^* depends on the electron-phonon coupling the results show that small and intermediate coupling polaronic distortions lead to a pronounced increase in T_c but reduce T_c in the strong coupling limit. Physically this situation corresponds to an interplay between the interband coupling favoring superconductivity and the lattice distortion which causes localization. Again a strong enhancement of T_c is observed for the case of two different order parameters as compared to the two *s*-wave order parameter case.

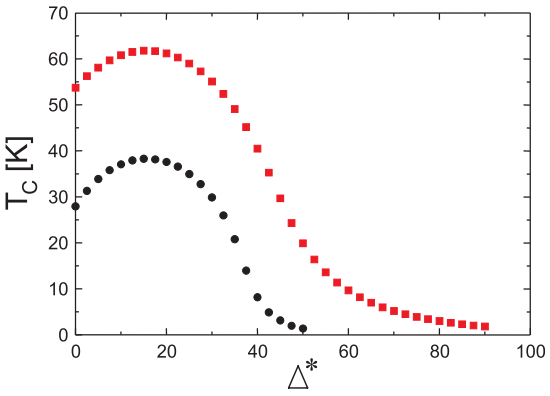

Figure 64: *The dependence of T_c on the polaronic shift Δ^*. The squares refer to s–d coupled order parameters, while the circles correspond to the s–s coupled case.*

In conclusion, new aspects of the two-band model for superconductivity have been investigated by considering the influence of different order parameter symmetries on T_c and by studying the effect of a polaronic distortion on it. Combining *s*- and *d*-wave order parameters

always enhances T_c substantially as compared to two isotropic order parameters since here low energy scales appear from the *d*-wave channel. The interband coupling also enhances T_c substantially and even at moderate coupling T_c values $> 100\,K$ are obtained. A polaronic distortion favors superconductivity as long as the corresponding electron-phonon interaction is not too large. For intermediate to large values of the coupling, superconductivity is rapidly depressed and even vanishes for too strong couplings.

Lattice expansion does not explain the T_c increase in chloroform- and bromoform- intercalated C_{60}

R.E. Dinnebier, O. Gunnarsson, H. Brumm, E. Koch, and M. Jansen;
P.W. Stephens and A. Huq (SUNY Stony Brook)

The groundbreaking experiments of J.H. Schön *et al.* have demonstrated that chemical doping is not the only way to make the fullerenes metallic and superconducting. Using a field-effect transistor setup they showed that pristine C_{60} can be field-doped and becomes superconducting with transition temperatures T_c up to 11 K for electron doping [J.H. Schön *et al.*, Science **288**, 656 (2000)] and 52 K for hole-doping [J.H. Schön *et al.*, Nature **408**, 549 (2000)]. For the chemically electron doped fullerenes it is known that T_c increases with the lattice constant, which is explained by the corresponding increase in the density of states [O. Gunnarsson, Review of Modern Physics **69**, 575 (1997)]. This was the motivation for investigating fullerene crystals intercalated with inert molecules that act as spacers to expand the lattice. And, indeed, it was found that T_c increases to spectacularly high values of 80 K for $C_{60}{\cdot}2CHCl_3$ and 117 K for $C_{60}{\cdot}2CHBr_3$, seemingly confirming the assumption that in order to increase T_c one simply has to increase the density of states [J.H. Schön *et al.*, Science **293**, 2432 (2001)].

Here we report structural determinations of the $C_{60}{\cdot}2CHCl_3$ and $C_{60}{\cdot}2CHBr_3$ co-crystals and give a comparison with pristine C_{60}. We find that intercalation of chloroform and bromoform indeed increases the volume per C_{60} molecule. That increase is mainly due to an expansion of the lattice perpendicular to the closest-packed planes, which are presumably the free surface on which the superconducting FET's have been grown; the area per fullerene remains essentially uncharged. In contrast to chemically electron-doped fullerenes, which are bulk superconductors, superconductivity in the field doped materials is confined to the immediate neighborhood of the surface. The prepared surface is not necessarily a simple truncation of bulk; for example there may be reconstruction, different fullerene orientations, a different concentration of intercalants, etc. However, it is reasonable to expect that the lattice spacings of the 3D structure should persist to the surface, and therefore estimates of the density of states (DOS) derived from the 3D structure will provide a useful insight into the superconductivity. To understand the effect of intercalation on the DOS at the Fermi energy, we have performed tight-binding calculations. We find that, in contrast to what one would expect based on the increase in T_c, the DOS for pristine C_{60} is actually larger than for the co-crystals. Comparing $C_{60}{\cdot}2CHCl_3$ and $C_{60}{\cdot}2CHBr_3$ we find that although the DOS differs slightly, this is by far not enough to explain the difference in the observed transition temperatures.

$C_{60}{\cdot}2CHBr_3$ and $C_{60}{\cdot}2CHCl_3$ were obtained by dissolving C_{60} in bromoform/chloroform with further evaporation. High resolution X-ray powder diffraction data of $C_{60}{\cdot}2CHCl_3$ and

C_{60}·2CHBr$_3$ were collected at various temperatures in a closed cycle helium cryostat at a wavelength of 1.15 Å on beamline X3B1 of the Brookhaven National Synchrotron Light Source in transmission geometry with the samples sealed in 0.7 mm lithiumborate glass capillaries (Fig. 65).

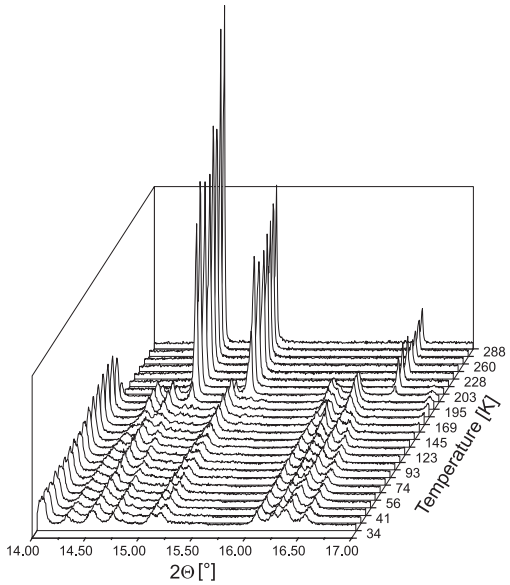

Figure 65: *Scattered X-ray ($\lambda = 1.15015(2)$ Å) intensity for C_{60}·2CHCl$_3$ as a function of diffraction angle 2Θ and temperature T. The temperature range of each scan is on the order of 10 K (cooling on the fly).*

The crystal structure of the different phases of C_{60}·2CHBr$_3$ and C_{60}·2CHCl$_3$ were determined by Rietveld refinements using flexible rigid bodies (Fig. 66). At room temperature, C_{60}·2CHCl$_3$ and C_{60}·2CHBr$_3$ are isotypic to magnesiumdiboride (space group P6/mmm, aluminumdiboride structure type) in which a primitive hexagonal packing is formed by C_{60} molecules with the trigonal prismatic voids at (1/3, 2/3, 1/2) and (2/3, 1/3, 1/2) fully occupied by chloroform or bromoform molecules, respectively. Therefore the structure can be viewed as a sequence of alternating layers of C_{60} and intercalated molecules perpendicular to the *c*-axis. With a six-fold axis through the center of the bucky ball (molecular symmetry $3\overline{m}$) and inversion centers in the center of the chloroform and bromoform molecules (molecular symmetry 3*m*), a minimum of twofold disorder is created, whereas Rietveld refinements confirm almost spherical shell electron density for the C_{60} molecule and at least threefold disorder for the chloroform molecules [G. Waidmann *et al.*, Zeitschrift für Anorganische und Allgemeine Chemie **621**, 14 (1995)].

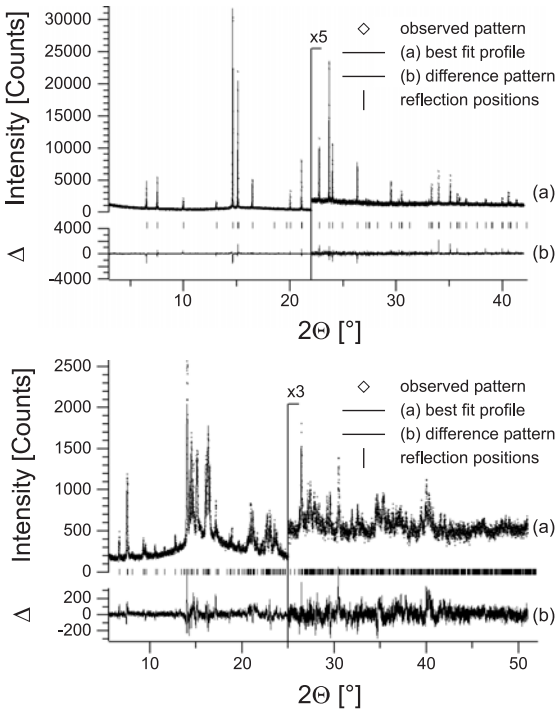

Figure 66: *The scattered X-ray intensity for C_{60}·2CHCl$_3$ at T = 295 K (top), and T = 50 K (bottom) as a function of diffraction angle 2Θ. Shown are the observed patterns (diamonds), the best Rietveld-fit profiles (line) and the difference curves between observed and calculated profiles in an additional window below. The high angle parts of the room temperature and the low temperature phase are enlarged for clarity.*

Upon cooling, both materials pass through a monoclinic phase (which will be discuss elsewhere) into a fully-ordered low temperature triclinic phase (space group $P\overline{1}$) at ≈ 150 K with cell dimensions similar to those of the hexagonal room temperature phase. The crystal structure of the triclinic low temperature phase may be viewed as an anisotropically distorted hexagonal room temperature structure. Whereas the

dimensions of the hexagonal closed packed layers of C_{60} molecules show only small distortions when compared to the room temperature structure, the distance between the C_{60} layers (triclinic *b*-axis) increases considerably, causing a decrease in dimensionality. The C_{60} molecules are oriented such that two hexagons on opposite side of the C_{60} molecule are congruent with the triclinic *b*-axis (corresponding to the hexagonal *c*-axis) running through the centers of the hexagons and one of their three short carbon-carbon bonds oriented parallel to *c*-axis (Fig. 67). This way, eight short bonds of a C_{60} molecule (two in *pm a*- and *pm c*-direction each) face short bonds of neighbor molecules with twisting angles between 60 and 90°.

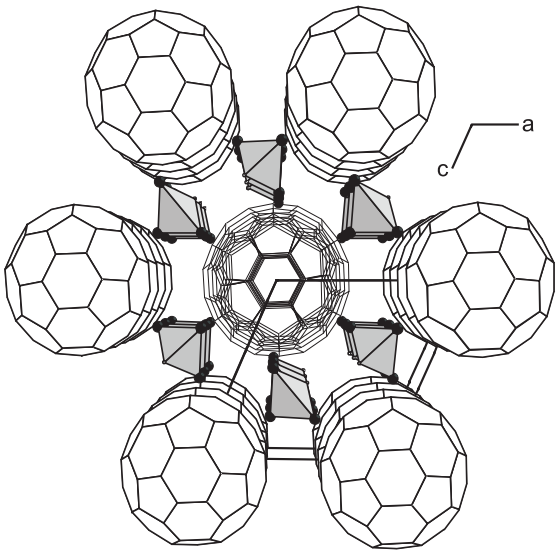

Figure 67: *Crystal structure of the low temperature phase of C_{60}·2CHCl$_3$ at T = 50 K (isotypic to C_{60}·2CHBr$_3$) in a view along b-axis showing the close relationship to the hexagonal room temperature phase.*

The differences in the orientation of the C_{60} molecules between the low temperature phases of C_{60}·2CHCl$_3$ and C_{60}·2CHBr$_3$ are only marginal. The shortest carbon-carbon distances occur between the C_{60} molecules within a layer along the *a*- and *c*-axis (≈ 3.3 Å). In contrast, the shortest carbon-carbon distances between C_{60} molecules of consecutive layers is increasing considerably when going from chloroform (≈ 3.6 Å) to bromoform (≈ 3.8 Å) doped C_{60}, which is in accordance with the observed increase in the lattice parameters.

The orientation of the chloroform and bromoform molecules in the two trigonal prismatic voids are related by inversion symmetry. Two halogene atoms point towards the middle between two C_{60} molecules of consecutive layers, whereas the third halogen atom points either up or down. Consecutive voids along the *b*-axis show the same orientation. The decrease of disorder from the hexagonal to the triclinic structures is accompanied by a loss of long range order and a decrease of the average coherence length (domain size) from approximately 7 μm down to 0.2 μm (in case of C_{60}·2CHCl$_3$) causing severe peak broadening. It should be noted that despite the low quality of the powder patterns at low temperature, the weighted profile R-value (R-wp) of the triclinic low temperature phase is sensitive enough to determine the orientation of the C_{60} molecule within reasonable accuracy: The R-wp of a completely misaligned C_{60} molecule deviates by more than 3%.

Heating-cooling cycles showed pronounced hysteresis (up to 40 K) and coexistence of the different phases over a large temperature range. In general, the transition temperature and the existence of the different phases of C_{60}·2CHCl$_3$ and C_{60}·2CHBr$_3$ depends strongly on their thermal history. In the case of C_{60}·2CHCl$_3$, additional intermediate phases of low symmetry occurred during slow cooling. At the low temperatures where superconductivity is observed basically all material is transformed into the thermodynamically stable low temperature phase as described above.

To describe the electronic structure of C_{60}·2CHCl$_3$ and C_{60}·2CHBr$_3$ we have set up a tight-binding formalism that properly describes the variation of T_c for A_3C_{60} (A = K, Rb). We put one radial 2*p* orbital on each carbon atom and calculate the molecular orbitals (MO) of a

free C_{60} molecule. Only the five-fold degenerate h_u MO is kept, and the hopping integrals between the h_u MOs on different molecules are calculated. The resulting Hamiltonian matrix is diagonalized. The $CHCl_3$ and $CHBr_3$ molecules are neglected in the calculation. Density functional calculations put the highest occupied and lowest unoccupied MOs of a free $CHCl_3$ molecule 1.7 eV below and 2.5 eV above the h_u-orbital of the free C_{60} molecule. These large energetic separations suggest that the $CHCl_3$ molecules contribute little to the structure of the h_u-derived band. The same should be true for $CHBr_3$. We consider the close-packed (010) surface of triclinic $C_{60}{\cdot}2CHCl_3$ (resp. Br) and the (111) surface of cubic pristine C_{60} in the $Pa\bar{3}$ space group. Since, due to the strong electric field, only the surface layer is believed to be doped, we study the corresponding two-dimensional lattices of C_{60} molecules arranged in an (approximately) hexagonal structure. This approach neglects the effects of the strong electric field on the surface layer and the (weak) coupling to the underlying layers.

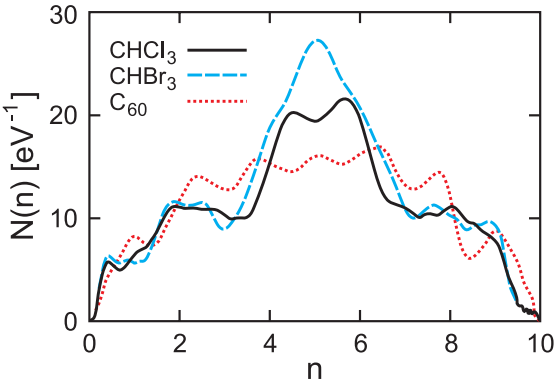

Figure 68: *Density of states N(n) at the Fermi energy as a function of the doping n. The figure compares results for the (010) surface of $C_{60}{\cdot}2CHCl_3$ and $C_{60}{\cdot}2CHBr_3$ and the (111) surface of pure C_{60}.*

Figure 68 shows the calculated density of states (DOS). The largest difference to the bulk is the reduced number of neighbors at the surface from eight to six for the $P\bar{1}$ $(0\bar{1}0)$ surface and from twelve to six for the $Pa\bar{3}$ (111) surface. This results in a reduced band width and an increased DOS. The DOS for C_{60} and $C_{60}{\cdot}2CHCl_3$ in Fig. 68 are comparable, but the DOS of C_{60} is larger for doping from about 2 to 3.5 where substantial T_c's have been observed. Based on the DOS one would thus expect T_c for C_{60} to exceed that of $C_{60}{\cdot}2CHCl_3$ – in contrast to experiment.

The orientations of the C_{60} molecules in the different structures play, however, an important role. Actually the surface area per molecule for $C_{60}{\cdot}2CHCl_3$ (86.5 Å^2) is slightly larger than for C_{60} (85.4 Å^2). The hopping between the molecules is, nevertheless, somewhat stronger for $C_{60}{\cdot}2CHCl_3$. The reason is that it mainly takes place via a few 'contact atoms'. The hopping is thus very sensitive to the relative phases of the h_u-orbitals at these atoms. These phases are relatively unfavorable for the $Pa\bar{3}$ structure of pure C_{60}, making the hopping somewhat weaker. To illustrate this, we rotated the C_{60} molecule in $C_{60}{\cdot}2CHCl_3$ by just 5° around the *b*-axis. This increases the second moment $\langle\varepsilon^2\rangle$ of the DOS by 15%. Rotating the molecules around the three crystallographic axes we find that $\langle\varepsilon^2\rangle$ changes by factors in the range 0.75–2.36. Since the DOS behaves roughly as $1/\sqrt{\langle\varepsilon^2\rangle}$, this suggests that a change in the C_{60} orientation is likely to decrease the DOS and a possible increase should be at most 15% for $C_{60}{\cdot}2CHCl_3$, still leaving it smaller than for C_{60}.

Comparing $C_{60}{\cdot}2CHCl_3$ and $C_{60}{\cdot}2CHBr_3$ is even more clear-cut since they basically only differ by their lattice constants, while the relative orientations of the molecules are similar. In the doping range 2 to 3.5 the DOS is increased by at most 10%. Solving the isotropic Eliashberg equations using realistic parameters we find, however, that the DOS of $C_{60}{\cdot}2CHBr_3$ would have to be about 25 to 35% larger than for $C_{60}{\cdot}2CHCl_3$ in order to explain the change in T_c. Thus even for the structurally similar intercalated crystals the increase in T_c cannot be understood as a result of the expansion of the lattice alone.

What might then be the reasons for the observed strong enhancement of T_c? What comes to mind first is that superconductivity may not be limited to the surface layer. However, to obtain a substantial doping, the levels in the surface layer have to be well separated from those in the layers underneath. Therefore their contribution to the DOS can be expected to be small. Also the strong electric field in the surface layer may play an important role. A simple estimate suggests, however, that its effect on the DOS should not be very large. There also could be some coupling to the vibrational modes of the $CHCl_3$ and $CHBr_3$ molecules, which might tend to enhance T_c. The large separation of their levels from the C_{60} h_u-orbital suggests, however, that this coupling is weak. Finally, as discussed above, the DOS can be quite sensitive to the orientations of the C_{60} molecules. It is conceivable that they could be different at the surface. For instance, the $CHCl_3$ and $CHBr_3$ molecules, having a dipole moment, would tend to align with the electric field at the surface, possibly influencing the orientations of the C_{60} molecules. The surface of pristine C_{60} could also be reconstructed in such a way that its DOS is reduced.

Above we have based our discussion on the DOS at the Fermi energy, as has been done in the past. This describes the variation of T_c for A_3C_{60} well, i.e., as a function of the lattice parameter for fixed doping. However, it does not describe the strong doping dependence of T_c, since the DOS of the merohedrally disordered A_3C_{60} is rather constant. In addition, for the electron-doped systems, field-doping and chemical doping give similar values of T_c. This is surprising, since the reduced number of neighbors at the surface should lead to a larger DOS and a correspondingly higher T_c. These problems raise questions about the conventional interpretation just in terms of the density of states.

Magnetic resonant mode in a single-layer high temperature superconductor

H. He, C. Ulrich, and B. Keimer; Y. Sidis, P. Bourges, and L.P. Regnault (CEA, France);
N.S. Berzigiarova and N.N. Kolesnikov (Russian Academy of Sciences)

Electronic conduction in the copper oxide high temperature superconductors takes place predominantly in structural units of chemical composition CuO_2, in which copper and oxygen atoms form an approximately square planar arrangement. Most theoretical models of high temperature superconductivity are therefore based on a two-dimensional square lattice. In real materials, however, deviations from this simple situation are nearly always present. For instance, buckling distortions of the CuO_2 layers that are found in many copper oxides are thought to have a significant influence on the electronic structure and on the superconducting transition temperature T_c. Interlayer interactions in materials with closely spaced CuO_2 layers (forming bi- or trilayer units) or additional copper oxide chains in the crystal structure present further complications whose influence on the superconducting properties remains a subject of debate. Experiments on $Tl_2Ba_2CuO_{6+\delta}$, a material with unbuckled, widely spaced CuO_2 layers and a maximum T_c around 90 K, have therefore played a pivotal role in resolving some issues central to our understanding of these materials.

We have performed inelastic neutron scattering measurements of $Tl_2Ba_2CuO_{6+\delta}$ near optimum doping ($T_c \approx 90$ K) that provide evidence of a sharp magnetic resonant mode below T_c. A resonant spin excitation of this kind has been ex-

tensively characterized by neutron scattering in the bilayer copper oxide $YBa_2Cu_3O_{6+\delta}$ and was recently also observed in $Bi_2Sr_2CaCu_2O_{8+\delta}$, another bilayer compound. At all doping levels, strong line shape anomalies of this collective spin excitation below T_c bear witness to a substantial interaction with charged quasiparticles. Conversely, anomalies in the quasiparticle spectra observed by a variety of charge spectroscopies (including in particular angle resolved photoemission, optical conductivity, and tunneling) have been interpreted as evidence of coupling to the neutron mode.

The correspondence between anomalous features in the spectra of spin and charge excitations has stimulated much theoretical work on the role of spin excitations in high temperature superconductivity. It is therefore of great interest to establish whether the resonant spin excitation is a general feature of the various crystallographically distinct families of superconducting copper oxides. The failure to detect such an excitation in the single-layer compound $La_{2-x}Sr_xCuO_{4+\delta}$, despite much experimental effort, has hampered a unified phenomenology of the copper oxides, and it has left us with two distinct classes of high-T_c oxides with very different spin excitation spectra. This unsatisfactory situation provided the motivation for our experiment on a material with an 'ideal' crystal structure and low intrinsic disorder.

Together with $HgBa_2CuO_{4+\delta}$, $Tl_2Ba_2CuO_{6+\delta}$ holds the T_c record for single layer materials (about 92 K), indicating that disorder effects (which are presumably at least in part responsible for depressing T_c in $La_{2-x}Sr_xCuO_{4+\delta}$) are minimal in this material. Unfortunately, the volume of the largest $Tl_2Ba_2CuO_{6+\delta}$ crystals currently available is more than two orders of magnitude too small for inelastic neutron scattering, a situation that is unlikely to improve anytime soon because of difficulties associated with the toxicity of thallium. We therefore assembled a multicrystal array containing about 300 individual crystals of optimally doped $Tl_2Ba_2CuO_{6+\delta}$, a section of which is shown in Fig. 69(a). The rocking curve of the array had a full width at half maximum of 1.5° (Fig. 69(b)). The quality of the alignment was confirmed by studying selected acoustic phonons, which were used for a calibration of the magnetic cross section. The experiments were carried out on neutron triple axis spectrometers that use beam focusing techniques to ensure efficient beam delivery onto small samples.

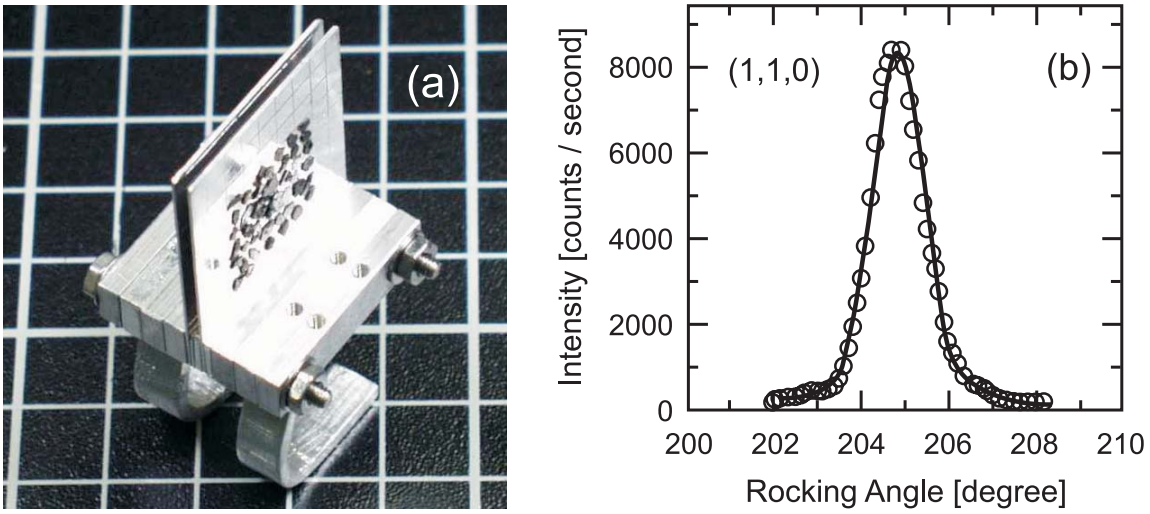

Figure 69: *(a) Photograph of the array of co-oriented $Tl_2Ba_2CuO_{6+\delta}$ single crystals. The crystals are glued onto Al plates only two of which is shown. (b) Rocking curve of the entire multicrystal array around the (1,1,0) Bragg reflection. The line is a Gaussian with a full width at half maximum of 1.5°.*

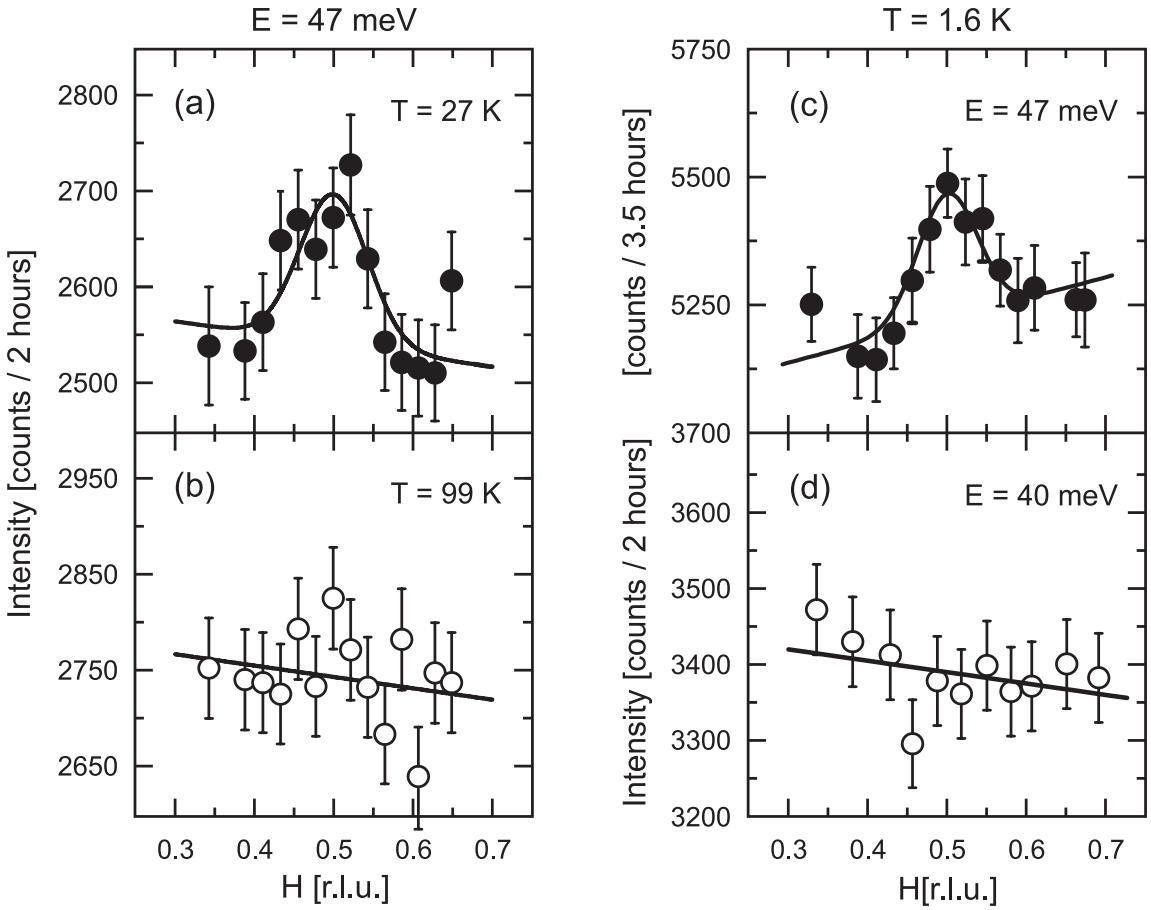

Figure 70: *(a), (b) Constant-energy scans along* $\mathbf{Q} = (H,H,L)$ *with* $L = 10.7$ *at an energy of 47.5 meV at temperatures above and below* T_c*. The components of the wave vector are given in reciprocal lattice units (r.l.u.), that is, in units of the reciprocal lattice vectors* $a^* = b^* = 1.62\,\text{Å}^{-1}$ *and* $c^* = 0.27\,\text{Å}^{-1}$ *of the tetragonal structure. The in-plane component* $(\frac{1}{2}, \frac{1}{2})$ *corresponds to the antiferromagnetic wave vector* $\boldsymbol{Q}_{AF} = (\pi, \pi)$ *in a notation where the lattice parameter is set to unity. (c), (d) Constant-energy scans at different excitation energies below* T_c*.*

Figures 70 and 71 show constant-energy and constant-$\boldsymbol{Q}$ scans, respectively, on the multicrystal array. An enhancement of the intensity sharply concentrated around the in-plane wave vector $\boldsymbol{Q} = (\pi, \pi)$ (that is, the wave vector characteristic of antiferromagnetic order in undoped copper oxides) and excitation energy 47 meV is observed below T_c. This is precisely the signature of the resonant mode in $YBa_2Cu_3O_{6+\delta}$ and $Bi_2Sr_2CaCu_2O_{8+\delta}$. When normalized per copper oxide layer, the spectral weight of the mode is comparable to that in the bilayer systems.

The intensity is independent of the momentum transfer perpendicular to the layers, as expected for weak interlayer exchange interactions. These and other data provide persuasive evidence that the resonant mode is indeed present in $Tl_2Ba_2CuO_{6+\delta}$ and must hence be regarded as a property of a single, isolated copper oxide layer. Interestingly, the mode energy found in $Tl_2Ba_2CuO_{6+\delta}$ exceeds the ones in both $YBa_2Cu_3O_7$ and $Bi_2Sr_2CaCu_2O_{8+\delta}$. This is in agreement with models according to which the resonant mode is a collective excitation pulled below the quasiparticle pair production continuum by exchange interactions. The lower mode energy in the bilayer materials could thus be a consequence of the strong interactions between the two CuO_2 layers that form a bilayer unit.

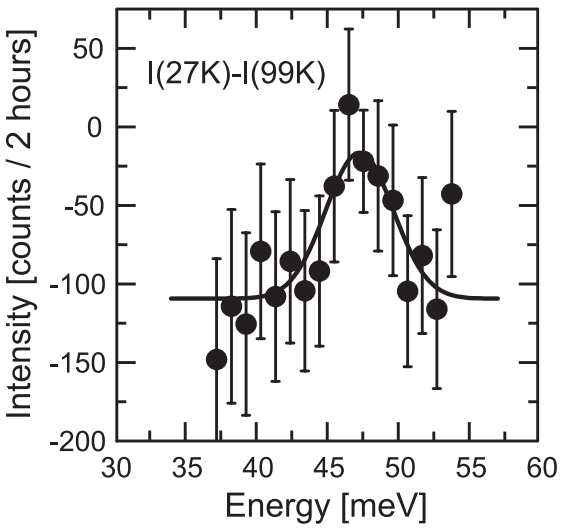

Figure 71: *Difference between constant-**Q** scans at $T = 99\,K (> T_c)$ and $T = 27\,K (< T_c)$, at wave vector **Q** = (0.5, 0.5, 12.25). The line is a Gaussian profile of width equal to the instrumental resolution. The constant negative offset arises from temperature dependent phonon scattering.*

In summary, we have taken another step in a program to develop a comprehensive experimental description of the spin dynamics of the copper oxide superconductors. This study demonstrates that inelastic neutron scattering experiments can be performed on materials of which only mm^3-sized single crystals are available. With time, other copper oxide families thus far not studied with neutrons may also become accessible to this technique.

The most important implication of our findings regards the unified phenomenological picture recently developed for spin and charge spectroscopies of the copper oxides. The spectral anomalies that have been interpreted as evidence of coupling to the collective spin excitation are also present in optical conductivity and tunneling data on single-layer $Tl_2Ba_2CuO_{6+\delta}$, and equally pronounced as in analogous data on bilayer materials. If the mode had turned out to be absent (or its spectral weight substantially diminished) in $Tl_2Ba_2CuO_{6+\delta}$, this general approach would have become untenable. It is now time to further refine the description of the coupled spin and charge excitations in the cuprates, and to fully evaluate its implications for the mechanism of high temperature superconductivity.

Construction of a novel high resolution neutron spectrometer at the Research Reactor Munich (FRM-2)

T. Keller, H. Klann, M. Ohl, H. Schneider, and B. Keimer;
K. Habicht (HMI Berlin)

A novel neutron spectrometer combining the resonance spin echo (NRSE) and the three axis spectroscopy (TAS) techniques is currently under construction at the FRM-2. The instrument will allow the determination of energies and linewidths of dispersing excitations, including both phonons and magnons, over the entire Brillouin zone. This is not possible with conventional neutron or optical spectrometers, which either lack in resolution or in the accessible *Q*-range. In a combined NRSE-TAS instrument, the spin echo technique provides the energy resolution in the μeV range, while the TAS background spectrometer defines the momentum resolution. The instrument applies a focusing technique first proposed by Mezei in the 1970's: by tilting the boundaries of the spin echo precession fields relative to the neutron beam the spin echo resolution function is tuned to the slope of the dispersion curve.

Spin echo phonon focusing was successfully demonstrated at a prototype NRSE spectrometer installed at the triple axis spectro-

meter V2 at Berlin Neutron Scattering Center (BENSC) [T. Keller *et al.*, Physica B **241-243**, 101 (1998)]. The NRSE technique uses precisely flat radio frequency spin flippers instead of the large DC solenoids of conventional neutron spin echo spectroscopy to define the precession field boundaries. Field inclination is achieved by rotating the rf-flipper coils. From experiments conducted at this prototype spectrometer, we have obtained important parameters for the design of a new instrument at the FRM-2 (Fig. 72).

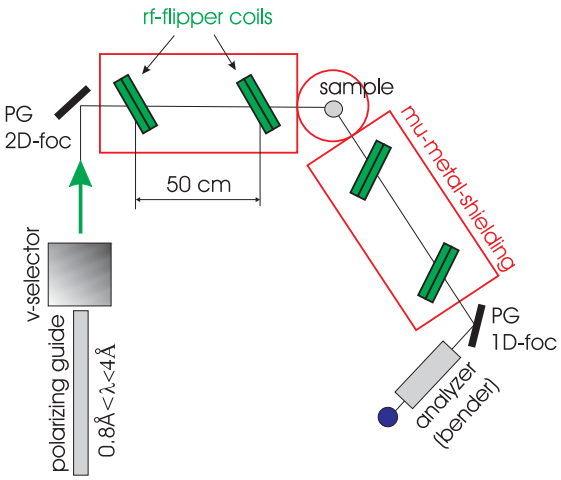

Figure 72: *Sketch of the NRSE-TAS spectrometer at the FRM-2. The polarizing neutron guide with supermirror coating located at a thermal beam tube provides a polarized neutron flux* $d\phi/d\lambda \simeq 3 \cdot 10^9\ cm^{-1}s^{-1}Å^{-1}$. *A carbon fibre Fermi velocity selector removes second order contamination. Monochromator and analyzer crystals (PG: pyrolytic graphite) with variable curvature allow to adjust the momentum resolution. The radio frequency coils and the sample are housed inside a mu-metal magnetic shield to reduce the sensitivity against external fields.*

As the expected interest for the new instrument is predominantly in the area of excitations with high energies (1–100 meV, resolution 1–100 μeV), the spectrometer is placed on a thermal beam tube at the end of a polarizing neutron guide with a very high flux for neutron wavelengths between 0.8 Å and 4 Å. In combination with a conventional graphite monochromator, the polarizing guide clearly outperforms Heusler monochromators (by a factor of 3 at 2 Å) and ^{3}He spin filters. At the time of this writing, construction of the spectrometer at the FRM-2 is almost complete. All major components are in place (Fig. 73), and the instrument will be ready for commissioning as soon as the reactor obtains its final operating license.

Figure 73: *Photograph of the current setup at the FRM-2.*

In the meantime, experiments have been performed on the prototype spectrometer at the BENSC in order to explore the capabilities of the technique. One of the motivations for building the spectrometer is derived from the electron-phonon interaction which plays a crucial role for most transport phenomena in metals. In particular, it has been demonstrated by tunneling spectroscopy a number of years ago that it is responsible for superconductivity in elemental metals. Modern ab initio band structure calculations for simple metals predict the electron-phonon coupling of every phonon over the entire Brillouin zone, as well as its contribution to the superconducting condensation energy. The phonon line broadening due to the electron-phonon interaction is typically of the order of 10 μeV. It is possible to achieve an energy resolution in this range by optical methods, but these are limited to $Q = 0$.

Figures 74 and 75 demonstrate that the NRSE-TAS technique is capable of resolving the intrinsic linewidth of a transverse acoustic phonon in Pb away from $Q = 0$. The beam polarization at the detector *versus* spin echo time

τ (proportional to the frequency applied to the rf-flipper coils) is the Fourier transform of the phonon line shape. A Lorentzian line transforms to an exponential with slope proportional to the line width Γ (Fig. 74).

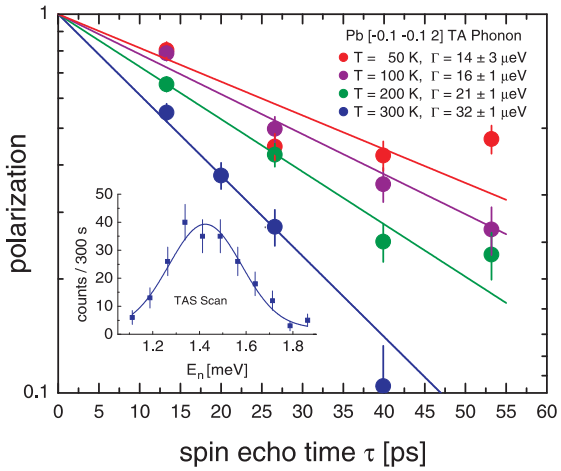

Figure 74: *NRSE-TAS linewidth measurement obtained for a TA phonon in Pb at the prototype spectrometer at BENSC. The beam polarization at the detector is plotted against the spin echo time τ. As described in the text, the slope on a semi-logarithmic plot gives the phonon line width. The inset shows a TAS energy scan on the same phonon with spin echo switched off.*

As the NRSE instrumental resolution is $\simeq 0.5\,\mu$eV (corresponding to $\tau_{max} = 1000$ ps), the measured phonon width is not resolution limited. (For comparison, the inset in Fig. 74 shows a TAS energy scan of the same phonon, with the spin echo coils switched off, whose peak width, $\approx 200\,\mu$eV, is given by the TAS instrumental resolution.)

Figure 75 shows the line width extracted from the spin echo profiles as a function of temperature. As the Pb sample is cooled, the phonon line width Γ decreases before saturating at a temperature independent value of 15 μeV. Whereas the temperature dependent part is due to phonon anharmonicity, the temperature independent contribution can be attributed at least in part to the electron-phonon interaction. At the moment, the low neutron flux at the prototype spectrometer limits these studies to acoustic phonons at low energy. Once it is fully operational, the new spectrometer at the FRM-2 will allow quantitative tests of the band structure calculations for Pb over the entire Brillouin zone as well as detailed studies of the effect of superconductivity on the phonon line widths. This will be a starting point for analogous investigations of more complex systems such as high temperature superconductors.

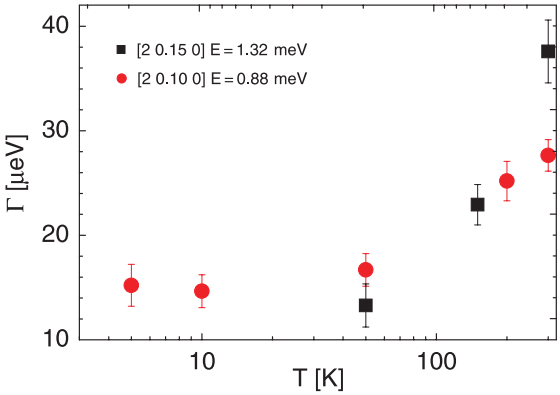

Figure 75: *Temperature dependence of the line width of the TA phonon in Pb extracted from the profiles of Fig. 74, showing temperature dependent and temperature independent contributions.*

Finally, the NRSE technique also has a high potential for other new applications. For instance, Rekveldt recently proposed to use the setup for high resolution diffraction (*Larmor diffraction*). The basic idea is to mark each neutron trajectory by a Larmor precession angle, thus obtaining very high resolution ($\Delta d/d \leq 10^{-6}$ where d is the lattice spacing) independent of beam divergence (up to several degrees) and monochromaticity [M.Th. Rekveldt *et al.*, Journal of Applied Crystallography **35**, 28 (2002)].

Growth of triple-layered cuprates $Bi_2Sr_2Ca_2Cu_3O_{10+\delta}$ single crystals

B. Liang and C.T. Lin

In the Bi-based cuprates superconducting systems, three superconducting phases have been identified to date. They are generally formulated by $Bi_2Sr_2Ca_{n-1}Cu_nO_{2n+4+\delta}$, where $n = 1, 2, 3$ represents the number of CuO_2 layers. A common feature of these three phases is predominant layer-growth morphology with strong anisotropy in properties. There are numerous studies concerning physical properties of $Bi_2Sr_2CuO_{6+\delta}$ (Bi-2201, $n = 1$; $T_c = 10$ K), and $Bi_2Sr_2CaCu_2O_{8+\delta}$ (Bi-2212, $n = 2$; $T_c = 90$ K); however, few studies have been done on $Bi_2Sr_2Ca_2Cu_3O_{10+\delta}$ (Bi-2223, $n = 3$; $T_c = 110$ K) due to lack of high-quality Bi-2223 single crystals. Owing to the complex solidification behavior, incongruent melting and narrow crystallization fields, it is hard to grow high-quality $Bi_2Sr_2Ca_{n-1}Cu_nO_{2n+4+\delta}$ crystals using conventional growth techniques. The traveling solvent floating zone (TSFZ) technique, however, has been proven to be suitable for the incongruent melt growth since it allows the crystal growth to occur continuously near one point on the temperature-composition phase diagram.

Since the activation energies for formation of Bi-2201, Bi-2212 and Bi-2223 phases are only slightly different, syntactic intergrowth of these phases is frequently observed in $Bi_2Sr_2Ca_{n-1}Cu_nO_{2n+4+\delta}$ ($n = 1, 2, 3$) samples prepared by different methods. Among the three superconducting phases, Bi-2223 has narrowest compositional range and narrowest temperature range of about 50°C below the incongruent melting line; therefore, obtaining single-phase Bi-2223 crystals has been a particularly difficult task. To investigate and develop reproducible growth conditions for preparing high-quality Bi-2223 crystals is of great interest and challenge. Recently we have applied the modified TSFZ method to investigate the growth of Bi-2223 crystals and successfully obtained large Bi-2223 single crystals measured up ($10 \times 6 \times 0.5$) mm.

The feed rods used for the crystal growth were prepared by the conventional solid state method. Powders of Bi_2O_3, $SrCO_3$, $CaCO_3$ and CuO (all of 99.9% purity) with cation ratio $Bi : Sr : Ca : Cu = 2.1 : 1.9 : 2.0 : 3.0$ were well mixed and calcined at 780°C for 48 hours in air with intermediate grindings. The calcined powder was formed into cylindrical rods ($\approx$ Ø 6 mm $\times$ 80 mm). The rods were hydrostatically pressed under a pressure of $\approx$ 70 MPa and sintered at 850°C for 50 hours in air. Prior to the crystal growth the high-density feed rod ($\approx$ 90% of the crystal density) was obtained by premelting the rod at a rapid rate of 25 mm/h. The quality of the premelted feed rods is critical to the TSFZ technique because the molten zone is sustained by the feed rod through surface tension during the crystal growth. Therefore a straight, long and equal-diameter feed rod is required to stabilize the molten zone over a long growth period.

Single crystals were grown by TSFZ method equipped with 4 halogen lamps as an infrared radiation source. A sharp temperature gradient of $\approx$ 300°C/cm along the molten zone was obtained by the use of 4 lamps of 300 W. A short premelted feed rod ($\approx$ 20 mm in length) was used as a seed rod in the crystal growth. Both the feed and seed rods were counter rotating (25 rpm/15 rpm) to ensure efficient mixing of the liquid. The mixed gas flow of argon and oxygen was applied. Due to the highly anisotropic crystallization rate for Bi-based cuprates, it is very difficult to obtain thick single crystals along the *c*-axis direction. Therefore, slow growth rates of 0.20, 0.10, 0.06 and 0.04 mm/h were used in an attempt to obtain large crystals. The experimental conditions are summarized in Tab. 1.

Table 1. *Growth conditions, crystal compositions derived from EDX analysis, presence of dominant phase determined from XRD and susceptibility measurements, and T_c of Bi-2223 single crystals.*

Feed rod composition	Crystal composition	Growth atmosphere	Growth rate [mm/h]	Dominant phase	$T_{c,onset}$ [K]
$Bi_{2.1}Sr_{1.9}Ca_2Cu_3O_{10+\delta}$	$Bi_{2.18}Sr_{1.82}Ca_{1.27}Cu_{2.15}O_{10+\delta}$	80% Ar + 20% O_2	0.20	Bi–2212	80
$Bi_{2.1}Sr_{1.9}Ca_2Cu_3O_{10+\delta}$	$Bi_{2.16}Sr_{1.84}Ca_{1.32}Cu_{2.34}O_{10+\delta}$	80% Ar + 20% O_2	0.10	Bi–2212	93
$Bi_{2.1}Sr_{1.9}Ca_2Cu_3O_{10+\delta}$	$Bi_{2.08}Sr_{1.92}Ca_{1.69}Cu_{2.69}O_{10+\delta}$	80% Ar + 20% O_2	0.06	Bi–2223	102
$Bi_{2.1}Sr_{1.9}Ca_2Cu_3O_{10+\delta}$	$Bi_{2.11}Sr_{1.89}Ca_{1.83}Cu_{2.87}O_{10+\delta}$	20% Ar + 80% O_2	0.04	Bi–2223	103

The Bi-2223 phase is incongruently melting and stable only within a narrow temperature range of about 50°C. A minor variation in composition can cause major changes in the phase contents, leading to a significant decrease of the volume fraction of Bi-2223 phase. For a narrow crystallization field a constitutional supercooling readily causes the cellular growth front, which results in the formation of multi phases. To overcome this problem, a slow zone-traveling rate and a sharp temperature gradient around molten zone must be applied during the growth.

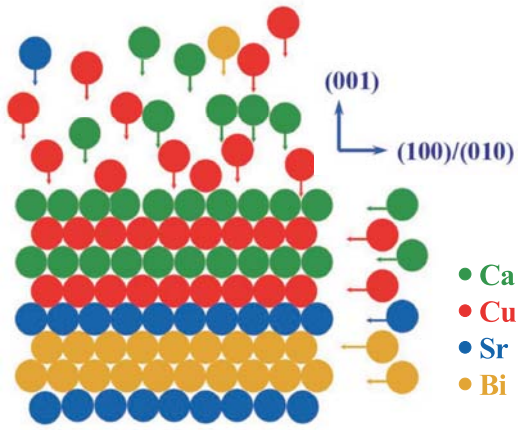

Figure 76: *Growth contour of the layer structure of Bi-2223 crystals.*

According to the Bi-2223 lattice structure, it might be assumed that the growth of (001) plane is a layer-by-layer process and a whole (001) face requires exposure to only one species of atom at a given instant for a layer to propagate. Other atoms in the vicinity of the (001) growth plane, therefore, cannot be adsorbed and diffuse to a 'kink' site in the lattice. Figure 76 schematically illustrates an instantaneous growth contour for layer-by-layer growth, along the (001) crystallographic axis. Growth of the Bi layers commence once the Sr layer is complete and Sr layer commences after Bi. The layer growth runs in cycles according to the growth contour of the layer structure, -Sr-Bi-Bi-Sr-Cu-Ca-Cu-Ca-Cu-, therefore, for (001) growth the diffusion of the relatively few Ca (Sr or Bi or Cu) atoms to the surface of the crystals is hindered by a large amount of Bi, Sr and Cu (Bi, Ca and Cu or Sr, Ca and Cu or Bi, Sr and Ca) atoms. This results in a serve depletion of Ca (Sr or Bi or Cu) atoms at the growth interface and an extended diffusion layer above the (001) plane. Because of this relatively long diffusion path along the (001) direction, a slow growth rate is thus desired for obtaining a thick crystal. Such diffusion phenomena do not exist for the (100) growth face since growth interface can directly adsorbed Bi, Sr, Ca or Cu atoms. Therefore the crystallization rate along the (100) direction is much faster ($\approx 10^3$ times) than that in the (001) direction, leading to the plate like morphology of Bi-2223 crystals, which exhibit the large *ab*-planes but small dimensions along the *c*-axes.

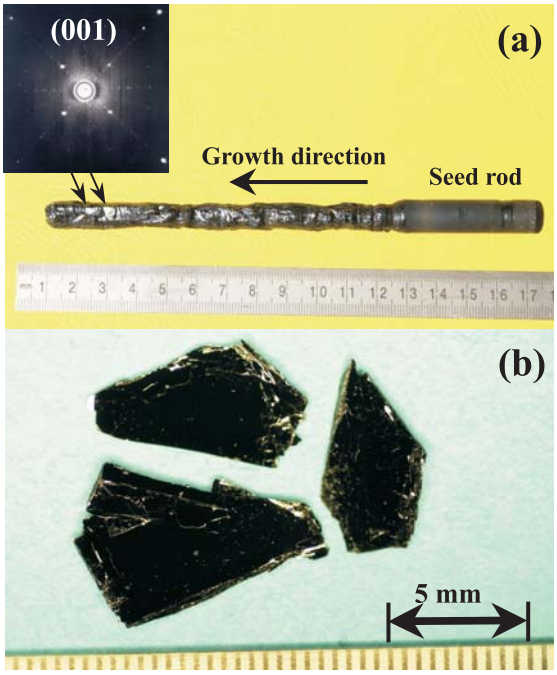

Figure 77: *(a) Bi-2223 as-grown ingot exhibiting the (001) facets on the surface. (b) Typical Bi-2223 single crystals cleaved from the ingot grown with a rate of 0.06 mm/h.*

Figure 77(a) shows an as-grown Bi-2223 ingot obtained with a growth rate of 0.06 mm/h. Many shiny facets can be seen from the cylindrical surface of the ingot. Laue X-ray back-reflection photography revealed that these facets are along the (001) crystallographic plane. Since the crystal growth was initiated on a polycrystalline seed rod, only needle-shaped crystallites were observed in the initial part after the ingot was cleaved. The crystallites became gradually larger as the ingot grew. However, the continuous growth of these grains was periodically interrupted when new planar growth fronts were created. This indicates that a frequent self-adjusted flux composition took place during the growth. As a result, the cleaved crystals exhibit 'V' shape, as shown in Fig. 77(b). The largest single crystal obtained was approximately $(10\times6\times0.5)$ mm, which is the largest ever reported.

The composition of each ingot was determined by EDX analysis. The results are presented in Tab. 1. The compositions of crystals grown at slow rates of 0.04–0.06 mm/h are close to Bi-2223 phase. Nevertheless, the compositions of crystals obtained at rates of 0.10–0.20 mm/h are close to Bi-2212 phase, demonstrating that the faster growth rates are unfavorable for the formation of Bi-2223 phase.

Single-crystal XRD measurements were made on a number of as-grown crystals chosen from each ingot to check the crystallinity. Figure 78 shows a single-crystal XRD patterns for the crystal grown with a rate of 0.04 mm/h. Only sharp (00*l*) peaks are observed, indicating the good crystallinity of the sample. All diffraction peaks can be indexed into the Bi-2223 phase with the *c*-axis lattice parameter of 36.552(6) Å.

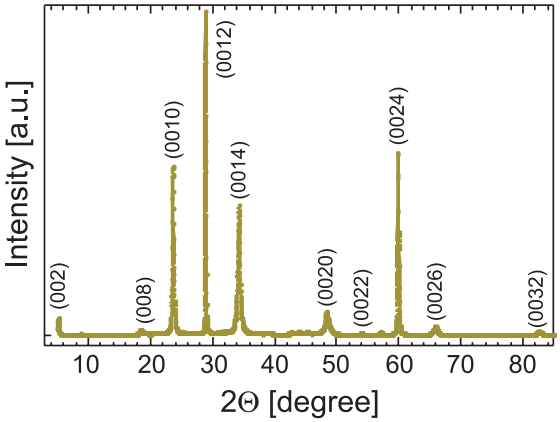

Figure 78: *Single crystal XRD pattern of as-grown Bi-2223 crystal grown with a rate of 0.06 mm/h, showing pure 2223 phase.*

Powder XRD measurements were performed on ground crystals in order to examine the presence of impurity phases as well as to determine the crystal structure and lattice parameters. It is noteworthy that the growth rate dramatically influences the phase formation of crystals. The crystals obtained at a rate of 0.20 mm/h exhibit majority phase of Bi-2212 and small amount of Ca_2CuO_3 and some unidentified phases. The crystals grown at a slower rate of 0.10 mm/h consist of Bi-2212, Ca_2CuO_3 as well as a small amount of Bi-2223 phase. When growth was performed at

a very slow rate of 0.04 mm/h, nearly single-phase Bi-2223 crystals were obtained from the as-grown ingot. Using a least-square refinement program the single-phase Bi-2223 crystals were determined to be orthorhombic structure with the lattice parameters $a = 5.408(2)$ Å, $b = 5.413(7)$ Å and $c = 36.868(1)$ Å (space group $A2aa$). These results demonstrate that a faster growth rate is unfavorable for the formation of Bi-2223 phase due to the extremely narrow crystallization field.

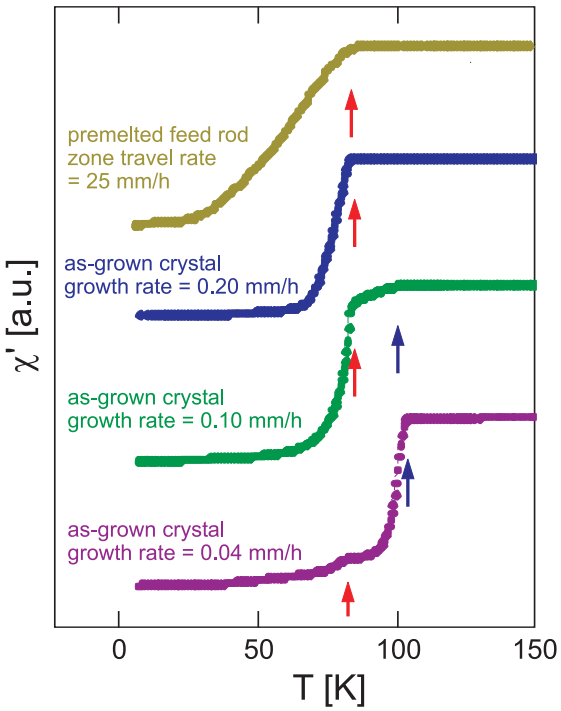

Figure 79: *Temperature dependence of AC-susceptibility measured on premelted feed rod and crystals grown with different rates, showing the effect of growth rate on the phase formation of Bi-2223 crystals. Only the real part (χ') of the AC-susceptibility is plotted.*

A large number of as-grown crystals from each ingot were checked using magnetic susceptibility measurements. These results also reveal that the crystal growth rate apparently influences the phase formation in crystals. Figure 79 shows the temperature dependence of the real part of AC-susceptibility measured on premelted feed rod as well as on as-grown crystals obtained at different growth rates. The premelted feed rod exhibits very broad superconducting transitions with onset $T_c \approx 80$ K, indicating that the principal superconducting phase in feed rod is Bi-2212 phase with an inhomogeneous oxygen distribution. The crystal grown at a rate of 0.20 mm/h exhibits a relatively sharp transition also around 80 K. No trace of a transition around 110 K could be seen, implying that the majority superconducting phase in fast-grown crystals is still Bi-2212 with relatively homogeneous oxygen distribution. When the growth rate decreases to 0.10 mm/h, the as-grown crystal displays two superconducting transitions around 100 and 80 K, corresponding to Bi-2223 and Bi-2212 phases, respectively. When an extremely slow growth rate of 0.04 mm/h was used, the as-grown crystals have a Bi-2223 phase $> 90\%$.

Post-annealing experiments were carried out at 500–850°C for 120–500 hours in an effort to improve the crystal quality with respect to phase purity and oxygen homogeneity. The effect of annealing was studied by both XRD and magnetic susceptibility measurements. A phase-transform process from Bi-2212 to Bi-2223 was observed. Such a phase transformation might be explained via a layer-intercalation mechanism, which suggests that Bi-2212 phase can be transformed to Bi-2223 phase through layer-by-layer intercalation of the Ca-Cu-O bi-layers into the existing Bi-2212 structure. Figure 80 shows the temperature dependence of AC-susceptibility measured on Bi-2223 as-grown and annealed crystals. The as-grown crystal shows two superconducting transitions around 102 K and 80 K, corresponding to Bi-2223 and Bi-2212 phases, respectively. As the annealing temperature is elevated and/or the annealing time increased, the transition at 80 K is gradually suppressed, indicating a decrease of the Bi-2212 phase. The crystal annealed at 850°C for 500 hours shows a sharp transition at 110 K with only a small remnant at 80 K. This indicates that nearly single-phase Bi-2223 crystals were obtained using slow growth rates (≤ 0.06 mm/h) and subsequent long-time annealing.

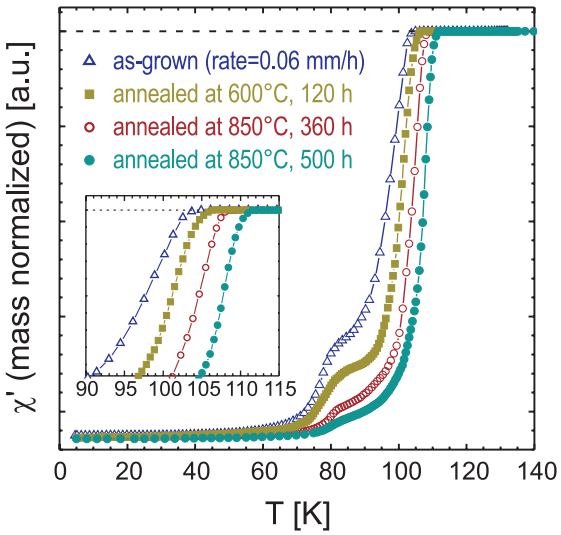

Figure 80: *Temperature dependence of AC-susceptibility measured on as-grown and post annealed crystals. Only the real part (χ') of the AC-susceptibility is plotted. The curves have been mass normalized to unity for the sake of comparison.*

The result of susceptibility measurements does not only demonstrate the influence of annealing on the phase transformation in crystals but also shows the effect of annealing on the superconductivity of Bi-2223 crystals. As shown in the inset of Fig. 80, the onset T_c increases from 102 K for the as-grown crystal to 110 K for the crystal annealed at 850°C for 500 hours. Usually it is difficult to precisely determine the oxygen content for single crystals, particularly for the large ones; however, from the tendency of T_c's change observed from the annealing experiments, one can suggest that the as-grown Bi-2223 crystals are in the underdoped region.

The in-plane and out-of-plane resistances as a function of temperature were measured on selected annealed crystals composed of almost pure Bi-2223 phase. The measured resistance was transformed to the respective resistivity ρ_{ab} and ρ_c using the crystal dimension. Figures 81(a) and (b) show the typical in-plane resistivity ρ_{ab} and out-of-plane resistivity ρ_c as a function of temperature, both of which show very sharp transition at 110 K. The typical *T*-linear behavior for ρ_{ab} and semiconductive upturn for ρ_c can be seen. The values of the resistivity for Bi-2223 crystals are of the same order of magnitude as those for Bi-2212 crystals.

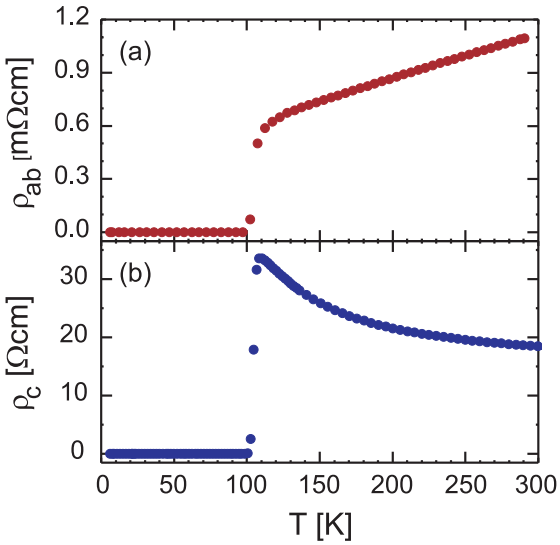

Figure 81: *Temperature dependence of (a) in-plane and (b) out-of-plane resistivity for Bi-2223 crystals annealed at 850 °C for 360 hours in oxygen flow.*

In summary, nearly single-phase (≈ 98–99%) Bi-2223 crystals have been obtained using the modified TSFZ technique with slow growth rates of 0.04–0.06 mm/h and subsequent annealing. Crystals as large as (10×6×0.5) mm were cleaved. Single crystal XRD measurements demonstrate the good crystallinity of samples except for those cleaved from the initial part of the ingot. Powder XRD and magnetic susceptibility measurements indicate that the growth rate directly influences the formation of Bi-2223 phase in crystals. As-grown crystals obtained at a very slow rate of 0.04 mm/h contain a Bi-2223 phase > 90%. Long-time annealing helps the phase transformation from Bi-2212 to Bi-2223 in the crystals. After annealing at 850°C for 500 hours, crystals almost have single-phase. T_c is found to increase from 102 K for as-grown crystals to 110 K for long-time annealed crystals. Both in-plane and out-of-plane resistances as a function of temperature show very sharp transition at 110 K. The general characteristic of resistivity in Bi-2223 crystals is similar to that of Bi-2212 crystals.

Influence of pressure on the properties of the layered superconductors $RE_2C_2Br_{2-x}I_x$ (RE = Y, La)

K. Ahn, R.W. Henn, R.K. Kremer, and A. Simon; W.G. Marshall (ISIS Facility);
P. Puschnig and C. Ambrosch-Draxl (Universität Graz)

Since the seminal papers by Ginzburg and Kirznits it is widely believed that two-dimensional layered materials provide optimum conditions for superconductivity with high T_c. Well known examples are the cuprate superconductors and more recently the 40 K superconductor MgB_2. Other superconductors with quasi-two-dimensional layered structures are the Ta and Nb dichalcogenides as well as organic superconductors which, however, display less spectacular transition temperatures. Of particular interest for superconductivity in layered materials is the question how the superconducting properties depend on the interlayer coupling. A variation of the coupling between the layers can be achieved by chemical means, as for example by doping with oxygen as demonstrated for the high-T_c cuprates or by intercalation as investigated for the dichalcogenides.

Another way to vary interlayer coupling and to change the superconducting properties is to apply external pressure. For example, the highest T_c of 164 K among the superconducting cuprates was obtained by applying pressure of 30 GPa to $HgCa_2Ba_2Cu_3O_{8+\delta}$. Superconductivity in the carbide halides of the rare earth metals $RE_2C_2X_2$ (RE = Y, La; X = Cl, Br, I) was discovered by Simon and coworkers in 1991 [see annual report I-77/1991]. The $RE_2C_2X_2$ compounds crystallize with layered structures with units of bilayers of close-packed rare earth metal atoms which are sandwiched between doublelayers of halogen atoms. The octahedral voids in the metal atom doublelayers are occupied by dimeric C–C dumbbells. Such X-RE-C_2-RE-X units stack with bonding via van der Waals forces and crystallize with a monoclinic structure. The C_2 orbitals are of essential importance regarding the electronic properties and the superconductivity of the $RE_2C_2X_2$ compounds: Overlap of antibonding $C_2-\pi^*$ molecular orbitals with energetically neighboring RE–d states causes a shortening of the C–C distance with respect to an ordinary molecular C–C double bond. This covalency gives rise to electron delocalization and metallic character of the $RE_2C_2X_2$ compounds. To gain further insight into the electronic structure and superconducting properties we have carried out detailed pressure experiments.

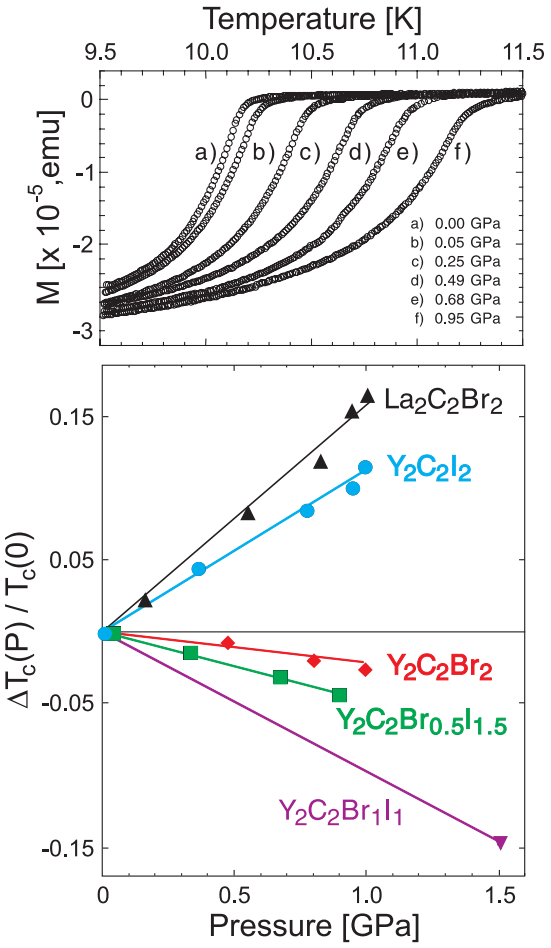

Figure 82: *Top: Magnetization of a sample of $Y_2C_2I_2$ at various pressures as indicated as obtained in a magnetic field of ≈ 0.5 mT. Bottom: Variation of T_c of various $RE_2C_2X_2$ with pressure.*

Depending on the particular system application of pressure may raise or decrease the critical temperature T_c. Figure 82 displays the magnetization of $Y_2C_2I_2$ as function of pressure indicating a rather sizable *increase* of T_c with pressure. An even larger relative pressure increase of T_c is observed for $La_2C_2Br_2$ showing a T_c of 7.03(5) K at ambient pressure. $Y_2C_2Br_2$ and other phases with a mixed halogen composition, however, undergo a decrease of T_c when pressure is applied.

Via the electron-phonon coupling constant λ this pressure dependence of T_c may be related to the variation of the electronic and the phononic system

$$\lambda \propto \frac{N(E_F)\langle g^2\rangle}{\langle \omega^2\rangle} \,. \qquad (19)$$

If we assume that the electron-phonon matrix element $\langle g^2\rangle$ and the average squared phonon frequency $\langle \omega^2\rangle$ increase smoothly with pressure the large observed increase of T_c for $La_2C_2Br_2$ and $Y_2C_2I_2$ indicates a sizable increase of the electronic density of states $N(E_F)$ when the cell volume is reduced by applying pressure indicating a remarkably structured $N(E)$ close to the Fermi energy E_F.

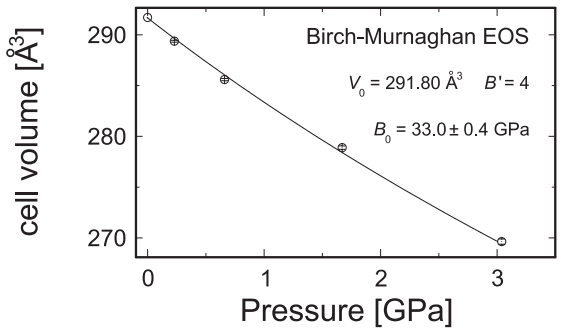

Figure 83: *Birch-Murnaghan fit (full line) to the pressure dependent cell volume data of $Y_2C_2I_2$ (POLARIS ISIS facility).*

To study the response of the lattice to pressure and to gain an estimate of $\langle \omega^2\rangle$ we performed detailed powder neutron experiments under pressure of $Y_2C_2I_2$ ($T_c \approx 10$ K) using a Paris-Edinburgh type pressure cell at the ISIS POLARIS TOF diffractometer. Up to a pressure of ≈ 3 GPa we observe a monotonous decrease of the cell volume shown in Fig. 83. A least-squares fit to a Birch-Murnaghan relation converged to a bulk-modulus of 33.0(4) GPa.

Profile refinements with the Rietveld method of the neutron powder diffraction patterns collected with applied pressure provide the pressure dependent atomic coordinates and cell parameters (Figs. 84(a) and (b)). These data were used as input to calculate the electronic structure of $Y_2C_2I_2$ with high precision. The results verify a growth of the density of states at E_F by about 50% and demonstrate that the characteristic valley structure at E_F observed for $Y_2C_2I_2$ is gradually filled. Quantitative estimates with a reasonable assumption for the mode Grüneisen parameter reveal that lattice stiffening reduces the increase of T_c by about 30% due to the sheer pressure changes of the electronic structure.

Above ≈ 3.5 GPa we discover a new high-pressure phase of $Y_2C_2I_2$ (Fig. 84(d)). The diffraction pattern at 3.03 GPa shows loss of intensity, especially, of the peaks around 2.3 and 2.8 Å, respectively, and the emergence of a new peak at ≈ 2.5 Å (Fig. 84(c)). The pressure-induced structural phase transition is reversible but appears to leave considerable strain after pressure release and, in particular, sizable disorder between the layers. The pressure released samples have a reduced T_c of about 7 K. $T_c \approx 10$ K can be restored by reannealing the samples for 1 day at 1050°C.

Detailed further investigations using neutron powder and X-ray powder techniques are underway to solve the crystal structure of the new high pressure phase of $Y_2C_2I_2$ and to search for pressure-induced phase transitions in the other phases of the superconducting layered rare earth carbide halides.

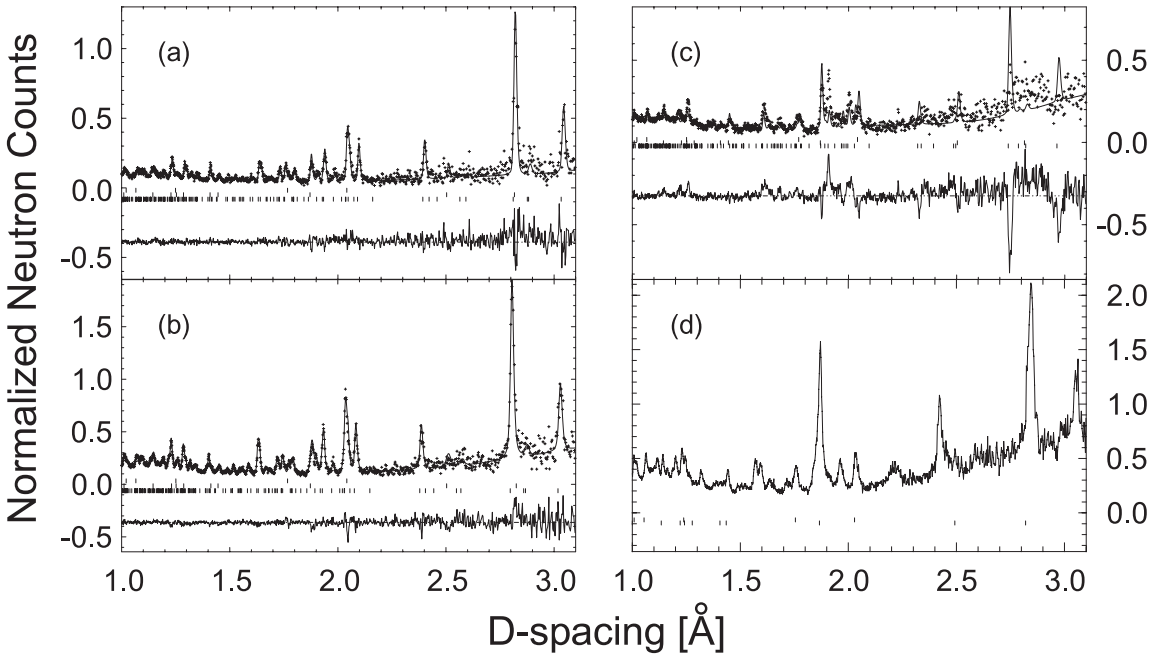

Figure 84: *Neutron powder patterns of a sample of $Y_2C_2I_2$ at (a) 0.14 GPa, (b) 0.72 GPa, respectively. Data collected at $2\theta = 90^\circ$ are shown as dots. The solid lines are the results of Rietveld profile refinements. Vertical bars indicate the position of the reflections used to generate the patterns. Upper bar row, medium bar row and low bar row indicate the reflections of the Ni gasket, WC anvils and of the $Y_2C_2I_2$ samples, respectively. The lower solid lines represent the difference between the observed and calculated patterns. Diffraction patterns at (c) 3.03 GPa show the results of comparison with a theoretical pattern indicating significant deviations from the ambient pressure to be present. (d) Diffraction pattern at 6.0 GPa evidences the new high-pressure phase. (The reflections emerging from the Ni gasket and the WC anvils are indicated by the vertical bars.)*

New structures and materials

In this chapter we report on the multifarious activities of the Institute in the field of the synthesis and characterization of new materials with interesting structures and unexpected properties. The synthesis and characterization of $[Sr(NH_3)_8]C_{70}\cdot 3NH_3$, a fulleride containing linear C_{70} chains, marks the first example of an accurate structure determination among polymeric fullerides, establishing a basis for a theoretical analysis of the rich structural and electronic properties of these materials. The most striking feature of $CsAu\cdot NH_3$ is the deep blue color, reminiscent of the solution of alkali metals in liquid ammonia. The observation of Ba_4O tetrahedra in $NaBa_2O$ puts a new twist to the long standing story of suboxide chemistry in this institute. $Na_{1-x}Sr_xNbO_3$ represents a new example of a composition induced metal to insulator transition in d^0 d^1 systems. The alkali metals Li and Na and zirconium tungstate, ZrW_2O_8, exhibit new polymorphs when exposed to high pressures. The chapter concludes with two presentations highlighting the use of microscopy for the structural characterization of solids, a high resolution electron microscopy study for the elucidation of the real structure when disorder is present and scanning tunneling microscopy of the catalytic process of CO oxidation over a RuO_2 surface.

Synthesis, characterization and bonding properties of polymeric fullerides $AC_{70}\cdot nNH_3$ (A = Ca, Sr, Ba, Eu, Yb)

H. Brumm, E.M. Peters, U. Wedig, and M. Jansen

One of the most obvious characteristics of fullerenes is that they are easily reduced and can accept a large number of negative charges – so far, the ions C_{60}^{-} to C_{60}^{12-} and C_{70}^{-} to C_{70}^{9-} have been detected. They are mainly obtained in compounds with electropositive metals and give rise to a great diversity of structural and electronic phenomena in these compounds. The fulleride anions may be present as isolated units, as dimers, or as polymers.

Fullerides of alkali and alkaline earth metals can be insulators, semiconductors, or metallic conductors. Some become superconducting with remarkably high transition temperatures, e.g., T_c equals 33 K for Rb_2CsC_{60} and 117 K for field-effect hole doped $C_{60}\cdot 2CHBr_3$, respectively. However, a consistent interpretation of the large range of experimental results obtained to date has been hampered by the conspicuous lack of reliable structural information.

Until now complete structure determination of polymeric fulleride species, based on the refinement of all atomic positions without any geometrical restrictions has not been possible. Thus, the available information does not yet offer any reliable basis for an analysis of the extent of the localization of the charges in polymeric ionic fullerides. In expanding our studies of fullerides to systems including linear polymeric $[C_{70}^{2-}]_n$ species we have been able to synthesize $[Sr(NH_3)_8]C_{70}\cdot 3NH_3$ (1) in the form of black crystals by reduction of C_{70} with strontium in liquid ammonia at room temperature. (1) has been characterized by means of single

crystal X-ray analysis and Raman spectroscopy, and analyzed by quantum chemical methods. Using the same process, C_{70} has also been reduced with Ca, Ba, Eu and Yb, and the resulting products have been analyzed by Raman spectroscopy.

In the course of the single crystal X-ray analysis of (1), all non-hydrogen atoms, including the carbon atoms of the fullerene cage, could be determined and their positions refined using anisotropic displacement parameters without the application of any geometrical restrictions. The values for the anisotropic displacement parameters of the fulleride ions are reasonable and do not indicate any kind of orientational or librational disorder. (1) crystallizes in the monoclinic space group P $2_1/c$, and the Sr atoms are coordinated by eight ammonia molecules in form of a distorted, two-capped trigonal prism with bond lengths in the range of 2.678(2)–2.827(2) Å. Three of these eight ammonia molecules act as donors for weak hydrogen bonds to other ammonia molecules of crystallization.

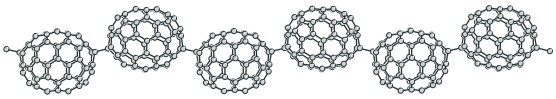

Figure 85: *Molecular structure of the polymeric* $[C_{70}^{2-}]_n$ *anion.*

The compound contains polymeric chains $^1_\infty[C_{70}^{2-}]$ (Fig. 85) where the C_{70} cages are linked to linear chains by single bonds between carbon atoms located in each of the two opposing five-membered rings along the fivefold axis of the neutral, undistorted cage. The chains form a hexagonal close packing of rods in the [001] direction (Fig. 86). The length of this bridging bond is 1.575(3) Å, suggesting a sp^3-hybridization of the atoms involved. Due to the one-dimensional connectivity, leading to the presence of two sp^3-hybridized carbon atoms, the point group symmetry of the C_{70} unit is lowered from D_{5h} for the uncharged fullerene to C_2. Although the crystallographic symmetry of the C_{70}-site is C_1, this additional point group symmetry (i.e., C_2) of the individual cages does not appear to be broken within the accuracy of the bond length determination.

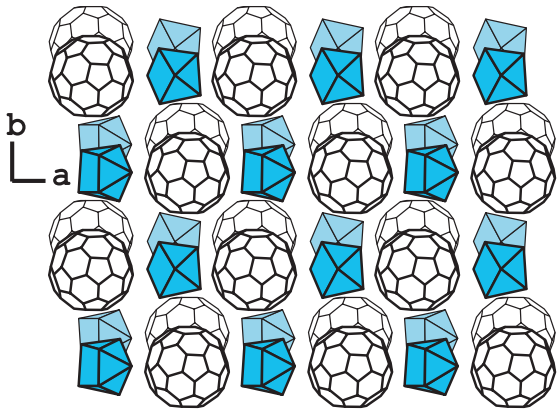

Figure 86: *Crystal structure of* $[Sr(NH_3)_8]C_{70}\cdot 3NH_3$ *viewed along the* $[C_{70}^{2-}]_n$ *chains.*

The Raman spectra of $AC_{70}\cdot nNH_3$ (A = Ca, Sr, Ba, Eu, Yb) exhibit bands characteristic of C_{70} (Fig. 87). However, due to symmetry reduction additional bands appear (factor group splitting). The most striking feature of the Raman spectra is the appearance of an additional band at $\nu \approx 945\,cm^{-1}$. Comparable bands have also been observed in the spectra of linked fullerenes, but in most cases these bands are not discussed in detail. To the best of our knowledge these bands correspond to the skeletal ν_{asym}(C–C) of the sp^3-hybridized bridging carbon atoms.

The very accurate knowledge of the crystal structure allows a comparison with theoretical investigations. For the model systems $[C_{70}H_2]^{2-}$ and $[C_{70}(CH_3)_2]^{2-}$ (isolated molecules), the structure has been optimized in C_1 symmetry with no restrictions, employing various Gaussian basis sets (minimal up to triple zeta with polarization functions) and ab initio methods (Hartree-Fock, DFT(LDA), DFT(GGA)). Typically, density functional calculations with small basis sets result in enlarged bond lengths, especially with gradient corrected functionals, while in the Hartree-Fock calculations the alternation of the bond lengths is

slightly overestimated. With a split valence basis set, the mean deviation of the calculated bond lengths compared to the corresponding experimental values in the C_{70}^{2-} units of the polymer is only 0.2 pm, with a standard deviation of 0.8 pm. Thus the large structural changes due to reduction and polymerization of C_{70} are perfectly captured in the theoretical calculations.

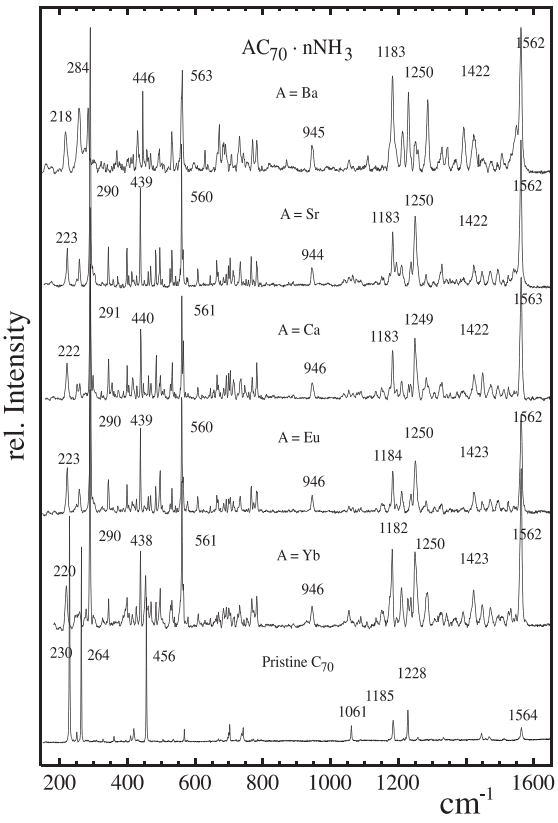

Figure 87: *Raman spectra of $AC_{70}{\cdot}nNH_3$ (A = Ca, Sr, Ba, Eu, Yb) and pristine C_{70}.*

The domains of the electron localization function (ELF) exhibit a characteristic shape depending on the bonding character in $[C_{70}(CH_3)_2]^{2-}$. When integrating the electron density within the basis of disynaptic attractors, one clearly can distinguish between the aromatic character of the six-membered rings in the belt of the cage (view 4 in Fig. 88), the conjugated double bonds in the caps (view 3 in Fig. 88), and the single bonds to the bridging carbon (view 1 in Fig. 88). Monosynaptic attractors are located at one of the carbons adjacent to the bridging atoms and at atoms with small angular sums (view 2 in Fig. 88).

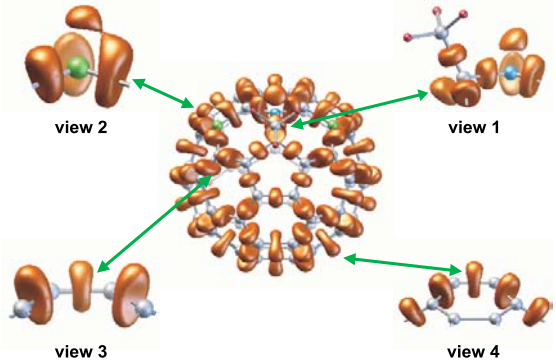

Figure 88: *Electron localization function domains (ELF = 0.8) in $[C_{70}(CH_3)_2]^{2-}$ calculated at the Hartree-Fock level with a split valence basis set.*

Structurally, C_{70} can be described as consisting of two 'caps' corresponding to one half of a C_{60} unit connected by a phenylene-type belt. From our investigations, we conclude that the high stability of this belt that is coupled to the preservation of the aromaticity in its hexagonal subunits is decisive for the reactivity of C_{70} and its tendency of forming polymeric anions. Clearly, since the distortions of the C_{70} cage upon reduction and polymerization are of a rather localized character, it has been necessary to perform the quantum chemical investigation on C_{70} and its derivatives without using symmetry or structural restrictions.

New gold compounds showing unusual properties

A.-V. Mudring, J. Nuss, U. Wedig, J.P. Ramalho, A.H. Romero, M. Parrinello, and M. Jansen;
F.E. Wagner (TU München); S. Krämer and M. Mehring (Universität Stuttgart)

Since in a given solid atoms of the same type prefer identical valence states and comparable geometric surroundings, solids containing the same element in a positive as well as negative oxidation state at the same time are extremely rare. The mixed valency in such compounds, e.g., the alkalides $M^-[M^+\text{crypt}]$ (M = alkaline metal), is stabilized by the positive electron affinity of the metal as well as by the gain in energy by complexation of the positively charged species.

Analogous considerations apply to the first examples of mixed-valent phases containing gold simultaneously in the oxidation states $+1$ as well as -1, $Rb_5Au_3O_2$, $Rb_7Au_5O_2$ and $Cs_7Au_5O_2$, recently characterized by us. In these 'intergrowth' structures (Fig. 89) belonging to the sequence $[MAu]_n[M_3AuO_2]$ with $n = 2, 4$, Au atoms$(+1)$ are linearly coordinated by two oxygen atoms, a coordination characteristic for oxoaurates(I), while the negatively charged gold atoms are exclusively surrounded by alkali metal atoms with interatomic distances lying in the common range of auride-alkali metal distances. Furthermore, the $Au(-1)/M(+1)$ substructure is virtually identical to the one found in the already known binary aurides CsAu and RbAu. The aurate$(+1)$ and auride(-1) parts are spatially separated preventing a neutralization via an internal redox process.

Our assignment of the oxidation states by crystal chemical evidence is supported by the results of Mößbauer spectroscopy, which clearly show the presence of two different gold species, since the chemical shifts and the quadrupole splittings indicate $[AuO_2]^{3-}$ units and Au^- ions.

Similarly, band structure calculations obtained either by density functional (LMTO) or Hartree-Fock calculations (CRYSTAL98) followed by an analysis of the band character, a population analysis (Mulliken, COHP) and an investigation of the electron localization function (ELF), unambiguously show the different character of the gold atoms and yield a consistent picture of the electronic structure. One gold atom is indeed a slightly polarized Au anion, and the *d*-shell of the gold atoms within the dumbbells is not completely filled (Fig. 90). However, the charge of Au(+) is definitively smaller than expected by general considerations and is smeared out within the dumbbells, perhaps stabilizing the observed mixed valency.

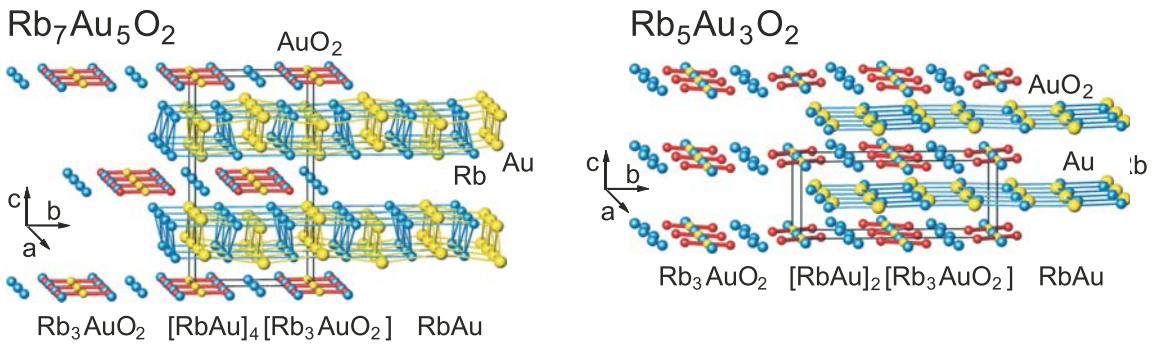

Figure 89: *Structure of $Rb_7Au_5O_2$ (left) and $Rb_5Au_3O_2$ (right).*

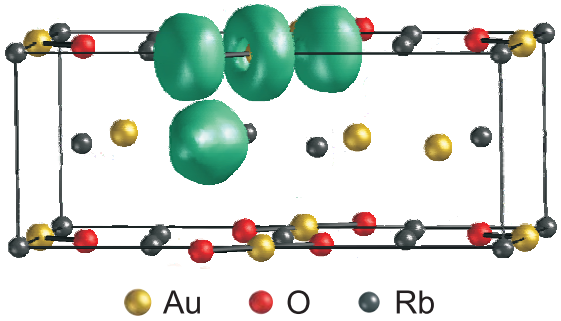

Figure 90: *Selected ELF-domains (ELF = 0.375) in $Rb_5Au_3O_2$.*

The reactions leading to the compounds shed new light on the chemistry of gold, and underline the similarity with the halogenes, which obviously goes beyond the mere structural chemistry: Although one of the most inert metals, gold readily disproportionates in the presence of basic oxides, similar to the behavior of the halogenes,

$$3Rb + 5Au^0 + 2Rb_2O \longrightarrow [RbAu^{-1}]_4[Rb_3Au^{+1}O_2] \quad (20)$$

$$Cl_2^0 + 2NaOH \longrightarrow NaCl^{-1} + NaCl^{+1}O + H_2O. \quad (21)$$

Another astonishing observation in the chemistry of gold is the ready dissolution of CsAu in liquid ammonia yielding a yellow solution. However, upon slow removal of ammonia, CsAu was not recovered directly, but instead an intensely blue solid crystallized first, which has been confirmed by structural analysis to be an ammoniate $CsAu \cdot NH_3$ (Fig. 91). Both color and UV-Vis-NIR spectra closely resemble those of blue solutions of alkali metals in ammonia, and suggest a possible electron transfer from gold, for which first indications are found in the crystal structure of $CsAu \cdot NH_3$.

The structure can be interpreted as an intercalation compound of CsAu with NH_3. Slabs of overall composition CsAu closely related to solvent free CsAu (Fig. 91) are separated by single NH_3 layers, similar to, e.g., $Cs_7Au_5O_2$, with AuO_2^{3-} units instead of NH_3. In $CsAu \cdot NH_3$, the gold atoms are shifted towards each other forming zig-zag-chains with comparatively short Au-Au-distances, indicating some bonding interaction. This compound, an ammoniate of an alloy, is without precedence from a chemical as well as a structural point of view, and in order to get some insight into the electronic structure of this solid further experimental and theoretical efforts have been made.

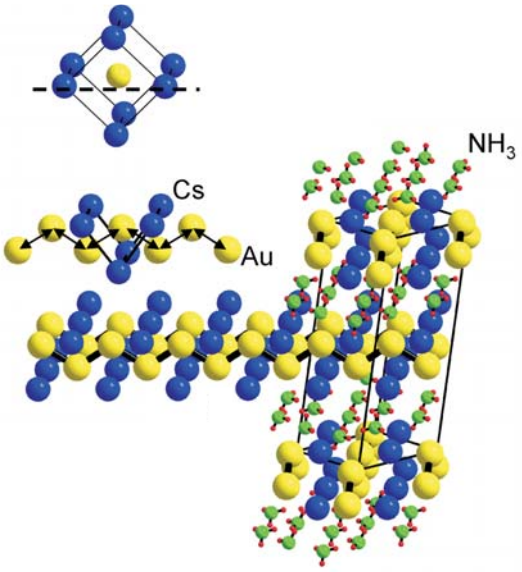

Figure 91: *Structure of $CsAu \cdot NH_3$.*

^{197}Au Mößbauer spectroscopy gives unambiguous evidence for a significant reduction of the (6*s*) electron density at the gold nucleus compared to the parent CsAu. Magnetic measurements as well as ESR-spectroscopy give no evidence for single, unpaired electrons. ^{1}H NMR investigations show that the properties of solid ammonia are basically preserved, and that the dynamics of the ammonia molecules can be described analogous to the one in solid NH_3.

The ^{133}Cs spectra (Fig. 92) display a strongly broadened and asymmetrical lineshape with a high frequency tail which has not been detected in CsAu. Since the spin-lattice relaxation rates vary over the signal, with a sizeable enhancement for Cs nuclei showing a large frequency shift, the line broadening is inhomogeneous in character. The behavior of both, lineshape and relaxation, can be explained within a model of dilute localized inhomogeneities in the electron

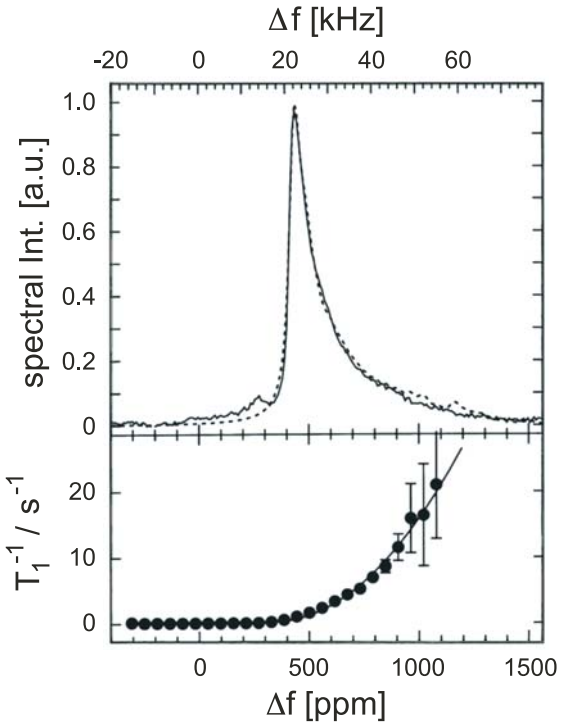

Figure 92: *^{133}Cs NMR spectrum of CsAu · NH_3 at 86 K (top) and the relaxation times T_1 (bottom). The dotted line comes from model calculations. Note that CsAu exhibits a chemical shift of ≈ 420 ppm vs. $CsNO_3$.*

density distributed along the CsAu chains, which induce an additional site dependent frequency shift and an enhanced fluctuation strength. The origin of the inhomogeneities can be attributed to a reduction of the charge density in the Au partial structure by a charge transfer to other structural regions.

Assuming a bipolaron state of spin paired electrons (charge 2*e*, spin $S = 0$) would explain both, the observed Cs NMR behavior and the diamagnetism of the bulk samples as determined by SQUID measurements. The 'electron(s)' are distributed over several NH_3 molecules and the charge transfer constitutes only a few percent of an electron per Au. This explanation is at least partly supported by an electronic structure calculation of CsAu · NH_3 via Density Functional Theory (DFT) in the local density approximation (LDA). Analyzing the maximally localized Wannier functions, one finds that for CsAu the valence electrons are localized on the gold atom, as expected. The doubly occupied valence states can be partitioned into two groups exhibiting a clear *s*+*d* character. In contrast, for CsAu · NH_3 the lowest five Wannier functions maintain the character they had in the parent compound, but the Wannier function with the highest energy is spread over a significantly larger region and its center is slightly shifted from the gold atom towards the nearest ammonia layer, losing the *d* character and resembling more a slightly distorted *s* state. We believe that it is this particular state which is responsible for many of the properties of CsAu · NH_3, i.e., the (formal) intercalation of ammonia into CsAu reduces the Coulomb field exerted by the cesium ions on gold, destabilizing the negatively charged gold, and as a consequence transferring some electron density from the Au site to the ammonia part of structure.

$NaBa_2O$ – a fresh perspective in suboxide chemistry

G.V. Vajenine and A. Simon

The 1932 edition of Gmelin's Handbook of Inorganic Chemistry cites several works describing a supposedly metallic suboxide of barium with the composition Ba_2O, which could be reportedly obtained by reacting the metal with BaO at temperatures around 1100°C, for example. In the 1960 complimentary volume on barium the existence of the suboxide is questioned. Solubility of metallic barium in the oxide was cited as a reason for the confusion leading to the erroneous reports of Ba_2O. So far no barium suboxides have been reliably characterized.

The chemistry of alkali metal (A) suboxides, on the other hand, was developed in the 1970s following the initial reports on cesium suboxides in the beginning of the last century. In all of the investigated metallic cesium and rubidium compounds oxygen-centered A_6O octahedra of metal atoms could be identified, condensed to larger clusters through face-sharing.

The motif of octahedral clusters repeats itself in the still growing family of alkaline earth metal (AE) subnitrides, in which $(AE)_6N$ clusters or their aggregates form stoichiometric compounds with sodium. Both the alkali metal suboxides and alkaline earth metal subnitrides feature a rather unique combination of ionic bonding within the A_6O or $(AE)_6N$ clusters and metallic bonding involving the remaining valence electrons in the rest of space.

As Na-K alloys proved to be an excellent flux for the preparation of alkaline earth metal subnitrides, it was also used to prepare a barium suboxide. Additionally, we hoped that a sodium matrix might stabilize the desired suboxide, as it does in the subnitrides $NaBa_3N$, Na_5Ba_3N, and $Na_{16}Ba_6N$.

Cooling down appropriate Na-K-Ba-O mixtures resulted in producing needle-shaped single crystals of a new compound $NaBa_2O$. The crystal structure could be solved and refined based on single crystal and powder X-ray diffraction data (orthorhombic in space group *Cmma* with $a = 6.5907(3)$ Å, $b = 15.327(1)$ Å, $c = 6.9385(5)$ Å, and $Z = 4$; Ba in 0,0.08701(2),0.19869(5), Na in $0,\frac{1}{4},0.6889(7)$, O in $\frac{1}{4},0,0$, $R1/wR2$(all data) = 0.0309/0.0777), the stoichiometry could be confirmed by elemental analysis. $NaBa_2O$ is the first compound in the Na-Ba-O system.

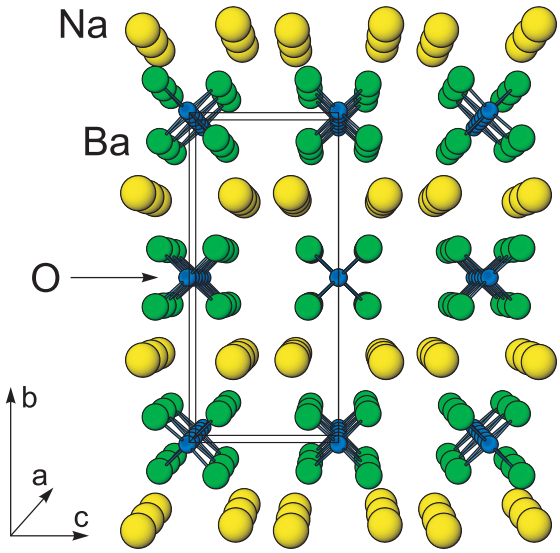

Figure 93: *The view of the $NaBa_2O$ crystal structure along the linear $^1_\infty[Ba_{4/2}O]$ chains. The orthorhombic unit cell is outlined.*

The most striking feature of the crystal structure of $NaBa_2O$ is the presence of Ba_4O tetrahedra instead of the expected Ba_6O octahedra. Edge-sharing between the tetrahedra leads to $^1_\infty[Ba_{4/2}O] \simeq Ba_2O$ chains, which are stacked parallel to each other and are separated by sodium atoms (Fig. 93), resembling the arrangement of Ba_3N chains in $NaBa_3N$ and Na_5Ba_3N. Although the $^1_\infty[Ba_{4/2}O]$ chains in $NaBa_2O$ are analogous to the $^1_\infty[SiQ_{4/2}]$ (Q = S or Se) chains in the silicon dichalcogenides, the packing of the $^1_\infty[Ba_{4/2}O]$ chains and Na atoms results in a new structure type. These chains also determine the preferred crystal growth direction of needle-like $NaBa_2O$ crystals.

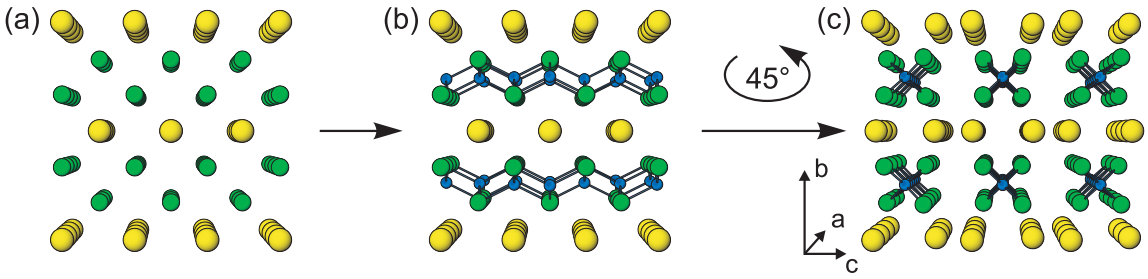

Figure 94: *Construction of the crystal structure of $NaBa_2O$ starting from a generic bcc lattice of metal atoms as in elemental Na or Ba. The lattice has every third layer occupied by Na atoms with Ba atoms in the remaining layers, corresponding to a hypothetical 'NaBa$_2$' alloy (a). The idealized crystal structure of $NaBa_2O$ obtained by filling half of tetrahedral voids in barium double layers of 'NaBa$_2$' by oxygen atoms (b). When this model structure with Ba in 0, 0.08333, $\frac{1}{4}$ and Na in 0, $\frac{1}{4}$, $\frac{3}{4}$ is rotated by 45° around the vertical b-axis (c) and is allowed to relax, the experimentally observed $NaBa_2O$ structure is obtained with the same view as in Fig. 93.*

The Ba–O distance of 2.5286(3) Å is significantly shorter than the Ba–O separation of 2.76 Å in BaO due to the coordination numbers CN = 2 and 4 for Ba and O, respectively, in $NaBa_2O$ compared to those in BaO (CN = 6). The separations between the metal atoms are in the range of those observed in sodium barium subnitrides and are typical for metallic bonding, which is consistent with the formulation $Na^+(Ba^{2+})_2O^{2-}\cdot 3e^-$.

The crystal structure of the suboxide can also be described starting from the body-centered cubic (bcc) packing of metal atoms, as in elemental Na and Ba. In the first step of construction, Ba and Na atoms are arranged in such a way that every third square layer contains Na atoms, with the remaining positions occupied by Ba atoms according to the $MoSi_2$ structure type. In the second step, half of the tetrahedral holes in the remaining Ba double layers are filled in an ordered fashion by O atoms so that the resulting $^1_\infty[Ba_{4/2}O]$ chains run in the [110] direction of the initial bcc lattice (Fig. 94). Full occupation of these voids would result in a $ThCr_2Si_2$-type structure. Based on this construction, one would expect the ideal *a*:*b*:*c* ratio of $\sqrt{2}$:3:$\sqrt{2} \simeq$ 1:2.12:1 for $NaBa_2O$, which is within 5% of the 0.95:2.21:1.00 ratio for the observed values of the lattice constants. Incidentally, the value $c/\sqrt{2} = 4.91$ Å lies between the values of the lattice constants of elemental sodium (*a*' = 4.29 Å) and barium (*a*' = 5.02 Å), suggesting that the above-described construction is realistic.

Surprisingly, the crystal volume of $NaBa_2O$ per formula unit ($V = V_{cell}/Z = 175.2$ Å^3) is larger than the sum V(Na) + 2V(Ba) = 166.3 Å^3. This is quite unusual in the view of a significant volume contraction which accompanies the formation of regular barium oxide BaO: V(Ba) = 63.4 Å^3 → V(BaO) = 42.1 Å^3. This contraction is caused by a volume reduction due to the formal oxidation of Ba^0 to Ba^{2+}. In the case of $NaBa_2O$, formally viewed as $Na^+(Ba^{2+})_2O^{2-}\cdot 3e^-$, the electrostatic repulsion between the oxide anions and the remaining valence electrons can be held responsible for the relatively large crystal volume.

Similar structural expansion has been observed in the other known alkali metal suboxides and alkaline earth metal subnitrides. These rather open crystal structures suggest a possibility of interesting high-pressure behavior, which has already been confirmed in preliminary experiments.

Structures and properties of the perovskite-type compounds $Na_{1-x}Sr_xNbO_3$ ($0.1 \leq x \leq 0.9$) a composition-induced metal-insulator transition

R.K. Kremer, A. Simon, and J. Köhler;
S. Istomin (Moscow State University); G. Svensson (Stockholm University)

Composition-induced metal-insulator transitions in complex perovskite-type oxides containing transition metals with d^0–d^1 electronic configuration are rare. For such a transition to take place the presence of enough charge carriers is necessary and in addition the occurrence of suitable paths of overlapping orbitals, which requires that the tilt of the NbO_6 octahedra should not be too large. In the d^0–d^1 oxotantalate system $Na_{1-x}Sr_xTaO_3$ ($0.0 \leq x \leq 0.4$) the electrical resistivity decreases with increasing strontium content, but metallic conductivity is not reached even for the highest possible strontium content $Na_{0.6}Sr_{0.4}TaO_3$ [S.Y. Istomin *et al.*, Journal of Solid State Chemistry **154**, 427 (2000)]. As reduced oxides with the lighter homologue Nb are more stable the system $Na_{1-x}Sr_xNbO_3$ with samples $0.1 \leq x \leq 0.9$ was investigated. They all crystallize as variants of the cubic perovskite-type structure (a_{per}). As a result of the substitution of Na^+ by the larger Sr^{2+} associated with the partial reduction of the small Nb^{5+} to the larger Nb^{4+} the volume of the perovskite subcell in $Na_{1-x}Sr_xNbO_3$ increases with the Sr content x, see Fig. 95.

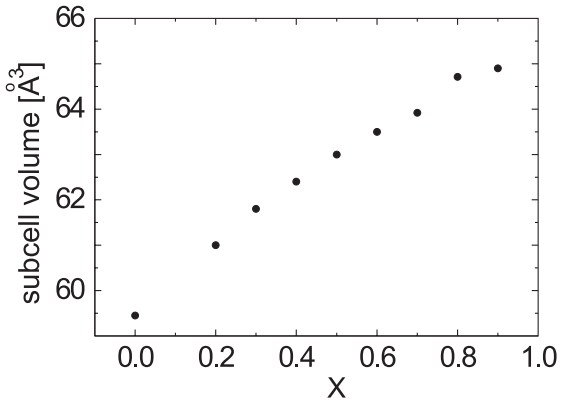

Figure 95: *The volume of the perovskite subcells (a^3_{per}) of $Na_{1-x}Sr_xNbO_3$ vs. the Sr content x.*

X-ray powder diffraction (XRD) studies of the $0.2 \leq x \leq 0.7$ phases indicate a tetragonal structure (*P*4/*mbm*) with unit cell parameters $a \approx \sqrt{2} \cdot a_{per}$, $c \approx a_{per}$, and for $x = 0.8$ and 0.9 the space group *P*4/*mmm* was found with $a \approx a_{per}$ and $c \approx a_{per}$. Rietveld refinements based on XRD and neutron diffraction data confirmed this for samples with $0.3 \leq x \leq 0.7$. However, SAED (**s**elected **a**rea **e**lectron **d**iffraction) and CBED (**c**onvergent **b**eam **e**lectron **d**iffraction) studies show that in crystallites of the $x = 0.2$ and 0.3 phases the tetragonal symmetry is broken, these phases being isotypic with $GdFeO_3$, space group *Pnma* with unit cell parameters $a \approx \sqrt{2} \cdot a_{per}$, $b \approx 2 \cdot a_{per}$, $c \approx \sqrt{2} \cdot a_{per}$. Crystallites of the $0.4 \leq x \leq 0.9$ samples consist of intergrown

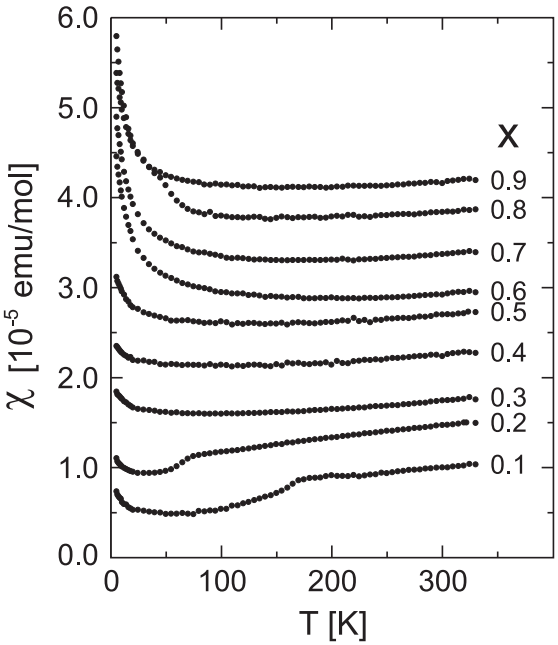

Figure 96: *Temperature dependence of the magnetic susceptibilities vs. temperature for samples $Na_{1-x}Sr_xNbO_3$ ($0.1 \leq x \leq 0.9$).*

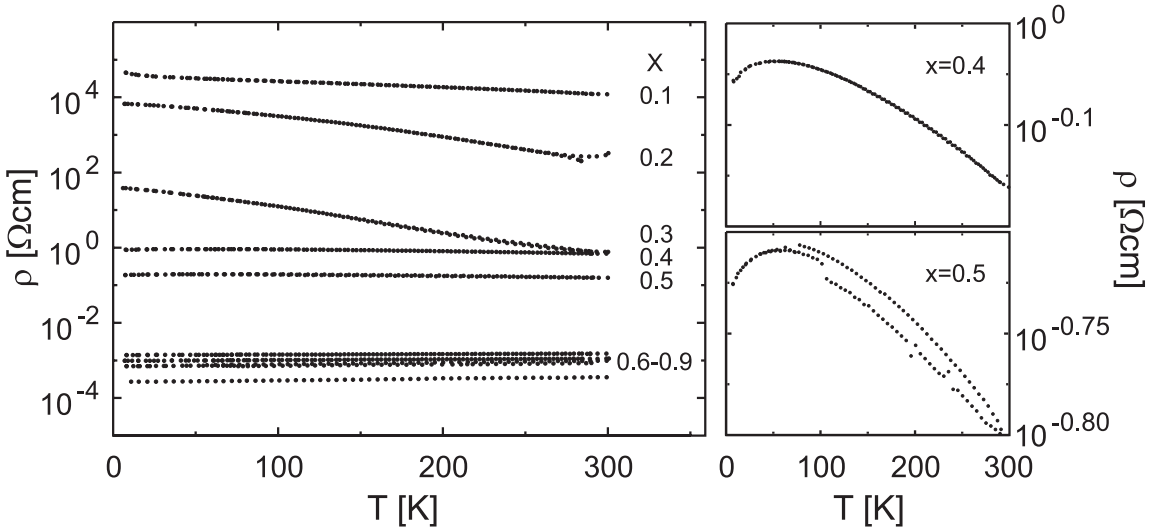

Figure 97: *Resistivity vs. temperature for $Na_{1-x}Sr_xNbO_3$ ($0.1 \leq x \leq 0.9$) together with the corresponding curves for the x = 0.4 and x = 0.5 samples with an enlarged scale (right).*

domains between this orthorhombic structure and a tetragonal variant of the perovskite structure (*P*4/*mbm*) associated with local variations in the Na and Sr content within the crystallites, a result which is interesting in the general context of phase separation.

The magnetic susceptibilities of $Na_{1-x}Sr_xNbO_3$ samples indicate paramagnetism within the entire range $0.1 \leq x \leq 0.9$, see Fig. 96. The paramagnetic susceptibilities are proportional to the carrier concentration. For samples with small carrier concentrations (x = 0.1 and 0.2) discontinuities of the temperature dependence of χ are observed at approximately 160 K and 60 K, respectively. However, these changes of χ are so small that they are probably related to structural changes rather than to changes in the magnetic structure.

The electrical resistivities of $Na_{1-x}Sr_xNbO_3$ samples with $0.1 \leq x \leq 0.9$ range over 8 orders of magnitude from approximately $10^4\,\Omega$ cm to $10^{-4}\,\Omega$ cm, see Fig. 97. Samples with low carrier concentrations (x = 0.1–0.3) are insulating. An unusual *non*-monotonic temperature behavior is found for the x = 0.4 and 0.5 samples. Their resistivities increase with temperatures up to a maximum around $T \approx 75$ K. Such a maximum of the resistivity was also observed for $La_{0.75}TiO_3$, whose composition lies between the insulating $La_{0.7}TiO_3$ and metallic $La_{0.8}TiO_3$ and is discussed in terms of disorder-induced localization [M.J. Maceachern *et al.*, Chemistry of Materials **6**, 2092 (1994)]. The complex temperature dependent behavior of the electrical resistivity of the $Na_{1-x}Sr_xNbO_3$ samples with x = 0.4 and 0.5 might therefore also be related to a fluctuation of the charge carrier concentrations in different crystallites caused by local variations in the Na/Sr ratio combined with vacancies at these positions.

Samples $Na_{1-x}Sr_xNbO_3$ with $0.6 \leq x \leq 0.9$ are metallic, and the linear dependence of the resistivity vs. temperature $\rho = \rho_0 + AT$ indicates an electron-phonon scattering mechanism. Obviously the composition-induced transition from semiconducting to metallic behavior takes place between x = 0.5 and 0.6 with no major structural change occuring but simply due to a large enough carrier concentration. The complex superstructures and electronic features of the perovskite-type niobates $Na_{1-x}Sr_xNbO_3$ ($0.1 \leq x \leq 0.9$) call for further studies, e.g., the clarification of the origin and nature of the metal-insulator transition in this system.

High pressure phases of light alkali metals

K. Syassen; M. Hanfland (ESRF, Grenoble); N.E. Christensen (University of Aarhus);
D.L. Novikov (A.D. Little, Cambridge, USA); I. Loa

The alkali metals represent simple metals in the sense that at normal density the conduction band electrons experience only weak interactions with atomic cores. Compression of the light alkalis Li and Na, however, is expected to induce strong hybridization effects between *s* and *p* valence electron orbitals leading to what has been termed electronic $s \rightarrow p$ transfer. Although, based on band structure calculations, the $s \rightarrow p$ transfer scenario in Li was known for many years, it was not before the recent theoretical work of Neaton and Ashcroft [J.B. Neaton *et al.*, Nature **400**, 141 (1999)] that important consequences for structural properties of compressed Li were considered.

Based on *first-principles* total energy calculations, performed within the framework of density functional theory, they predicted that (i) symmetry-breaking structural transitions should occur at about 2.5-fold compression (40 to 50 GPa) and (ii) Li may become an insulating solid at pressures above 100 GPa by adopting an orthorhombic structure with 8 atoms per cell similar to that of α-gallium. These theoretical predictions stimulated several experimental studies of Li and Na under pressure. The current excitement over the behavior of compressed light alkalis partly stems from its possible relevance for research on dense hydrogen near the insulator-metal borderline.

We have performed synchrotron X-ray powder diffraction experiments of Li and Na in the 100 GPa (1 Mbar) pressure range. Experiments were carried out at the ID9 beamline of the ESRF Grenoble using diamond anvil cell (DAC) techniques. Our interest was primarily in pressure-driven structural phase transitions. We have furthermore performed *first-principles* calculations of the structural stability and electronic properties. Here, we give a summary of our main findings [M. Hanfland *et al.*, Nature **408**, 174 (2000); M. Hanfland *et al.*, Physical Review B submitted; M. Hanfland *et al.*, High-pressure phases of Na above 100 GPa, unpublished].

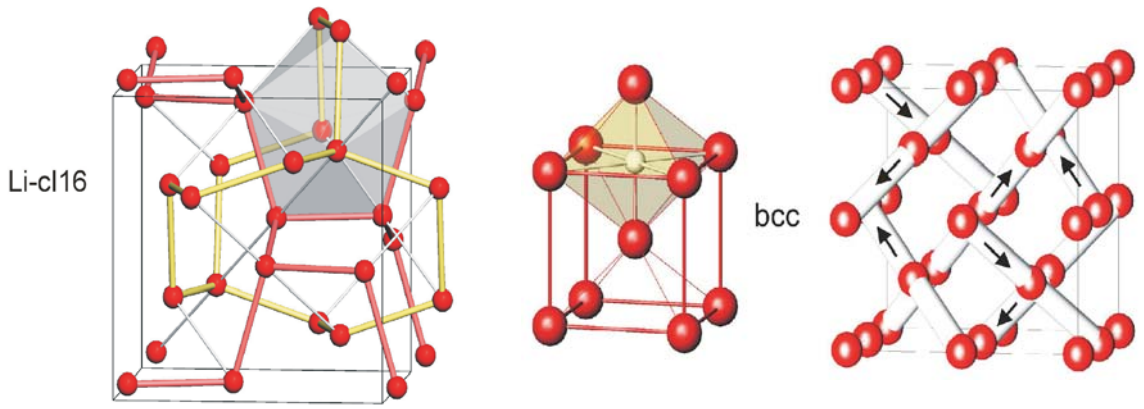

Figure 98: *The crystal structure of Li near 45 GPa. The cubic cell of the body-centered Bravais lattice contains 16 atoms (space group $I\bar{4}3d$, cI16 in Pearson notation). The shortest interatomic contacts, indicated by thick lines, form two interpenetrating 3-coordinated nets. The structure can be interpreted as a 2×2×2 superstructure of bcc obtained by moving rows of atoms parallel to the four body diagonals by vectors [x,x,x] (with sign permutations) as indicated in the right part of the figure. A characteristic feature of Li-cI16 is that interstitial sites (Wyckoff 12a) are surrounded by eight Li atoms forming distorted dodecahedra whereas in bcc the interstitial sites are six-fold coordinated.*

In addition to the known high-pressure *fcc* modification, we have observed two new phases of Li (experiments with Li were performed at $T = 180$ K in order to suppress the diffusion of Li into the strained diamond anvils). Between 38 and 42 GPa Li adopts a rhombohedral primitive structure (Pearson symbol hR1) similar to that of α-mercury. This structure can be regarded as a distortion of *fcc*, involving a compression along one of the 3-fold cubic axes and an increase of interatomic distances in hexagonal close packed layers oriented perpendicular to that axis.

Near 42 GPa, the structure of Li becomes cubic again, however, with 16 atoms per unit cell (Fig. 98). The space group is $I\bar{4}3d$ and atoms occupy the Wyckoff 16c site with coordinates (x,x,x), i.e., there is only one internal position parameter ($x \approx 0.05$). This structure type was not previously observed for any other elemental solid. In the following we refer to the phase as Li-cI16. The structure of a high-pressure form of Ga belongs to the same space group, but the Ga atoms occupy the Wyckoff 12a site, which is the center of the distorted dodecahedron shown in Fig. 98.

The 16-atom cubic structure is easily derived from *bcc* (SG *Ia–3d*) as schematically indicated in Fig. 98. The arrangement of atoms in Li-cI16 is similar to that of the cation substructures in compounds with the anti-Th_3P_4 and Pu_2C_3 structure type, e.g., Yb_4As_3 or Rb_4O_6. Thus, a trend, which has emerged form structural studies of the heavy alkali metals also applies to Li: the low-symmetry structures encountered when these simple metals are compressed have counterparts in cation substructures of binary compounds. Furthermore, the maxima in the calculated real-space valence electron distribution (Fig. 99) occur at the interstitial Wyckoff 12a site (Fig. 98), which is the location of anionic units in the structurally related binary compounds.

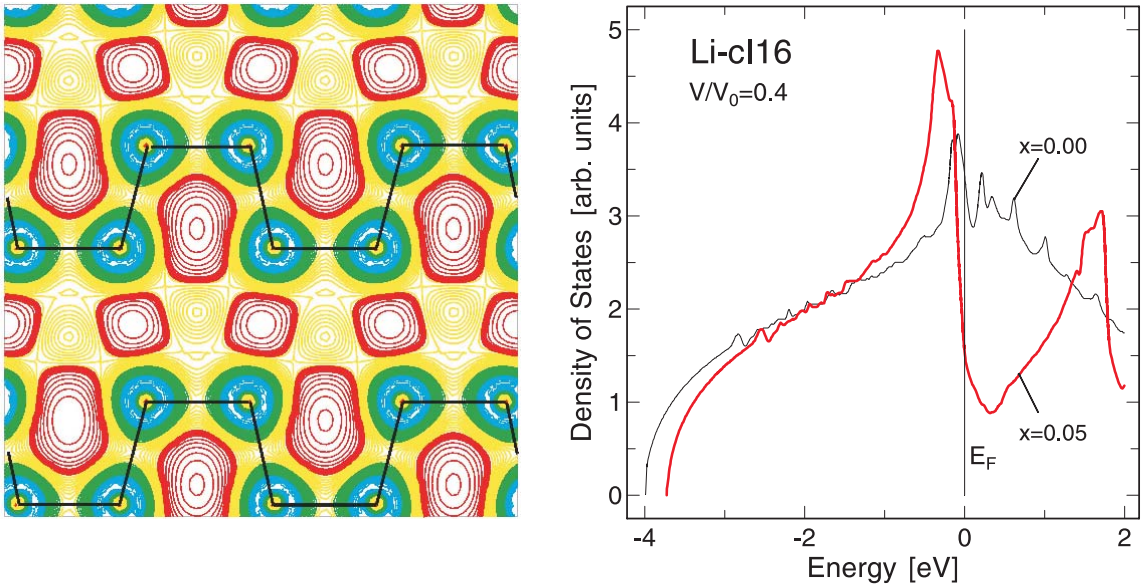

Figure 99: *Calculated electronic properties of Li-cI16 (SG $I\bar{4}3d$, $Z = 16$) at a relative volume of $V/V_0 = 0.4$, corresponding to 48 GPa calculated pressure. Left: Valence electron density in a plane parallel to (100). Projected positions of nearest-neighbor atoms are connected by straight lines. Density maxima occur in interstitial regimes marked by thick contours. Inside these contours, the valence electron density is higher than the average density. Right: For the optimized positional parameter of $x \approx 0.05$ a pronounced minimum occurs in the density of states near the Fermi energy E_F. The minimum is absent in the case of an undistorted ($x = 0.0$) 16-atom supercell of the bcc structure.*

The calculated electronic density of states (DOS) for the undistorted ($x = 0.0$) superstructure of *bcc* peaks close to the Fermi level E_F (Fig. 99) which is due to a flat degenerate band near E_F. The distortion towards $x = 0.05$ lifts the band degeneracy and changes the band dispersions, causing a pronounced minimum in the DOS close to E_F and a maximum of mainly *p* orbital character about 0.4 eV below E_F. In other words, band structure theory indicates that Li shows semimetal-like electronic features at pressures above 42 GPa. With respect to *bcc*, the distortion towards Li-cI16 is reminiscent of a Peierls type instability where a symmetry-breaking structural distortion leads to a gain in band structure energy.

Our theoretical modeling of the phase stability of Li based on density functional theory fully reproduces the observed phase transition sequence near 30–50 GPa (i.e., *fcc* → hR1 → cI16). With respect to all other structures considered in the calculations the optimized Li-cI16 structure is found to be lowest in enthalpy from 48 GPa up to 165 GPa, where it would yield to the orthorhombic phase proposed by Neaton and Ashcroft. More recently, however, that structure was reported to be dynamically unstable [R. Rousseau *et al.*, 18th International Conference on High Pressure Science and Technology, Beijing (2001)], an indication that other phases may occur at pressures lower than 100 GPa. Thus, the experimental search for new phases of Li, in particular an insulating one, will continue. Another attractive subject would be a test of the prediction that Li-cI16 may be superconducting with a transition temperature exceeding 50 K [N.E. Christensen *et al.*, Physical Review Letters **86**, 1861 (2001)].

Contrary to Li, the core states of Na involve *p* orbitals, posing orthogonality requirements for *s- and p*-like valence electron states with possible consequences for pressure-induced changes of bonding properties when compared to Li.

We have found that compressed Na transforms, like the other alkali metals, from *bcc* to *fcc*. The transition pressure for Na is rather high (65 GPa at 300 K, 7 GPa for Li). The stability range of the *fcc* phase extends to 103 GPa, where Na transforms directly to the cubic 16-atom structure observed for Li, without any indication for an intermediate phase. Pressure *vs.* atomic volume data of Na are shown in Fig. 100. The volume change at the *bcc-fcc* transition (–0.1%) is close to our resolution limit for volume differences between two cubic phases.

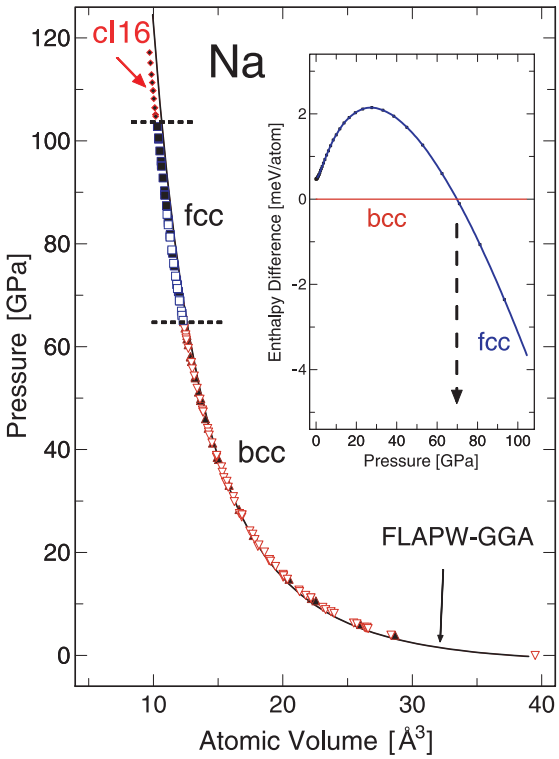

Figure 100: *Pressure-volume data for sodium measured by synchrotron X-ray diffraction at 300 K. Na transforms from bcc to fcc at 65 GPa and to a Li-cI16 analog phase (SG $I\bar{4}3d$) at 104 GPa. At 100 GPa Na is compressed to about 26% of its ambient pressure volume. The solid line marked FLAPW-GGA corresponds to a calculated PV relation for fcc-Na (static lattice limit). The inset displays the calculated enthalpy difference for bcc and fcc Na as a function of pressure.*

To illustrate that *first-principles* calculations yield a compression behavior in good agreement with the experimental data we show in Fig. 100 a *PV* relation calculated for the *fcc* phase of Na (results for *bcc*-Na are hardly distinguishable from those for *fcc*-Na). At

100 GPa the calculated volume is larger by only $\approx 3\%$. In terms of pressure, the difference amounts to ≈ 10 GPa. It cannot be ruled out that part of this difference is due to systematic errors in the pressure scales used in the experimental studies.

The inset of Fig. 100 shows the calculated enthalpy differences for *bcc* and *fcc* phases of Na. Results of calculations by other authors are qualitatively similar, except for a different ordering of phases at ambient pressure in some of the calculations. Increasing pressure first stabilizes *bcc*, but then, near 70 GPa, *bcc* becomes unstable relative to *fcc*. The calculated transition pressure of 70 GPa for the static-lattice limit (estimated uncertainty ± 10 GPa) agrees well with the experimental results at 300 K. Attention is drawn to the magnitude of the enthalpy differences; at all pressures their values are rather small compared to thermal energies at 300 K (25 meV/atom). Thus, in stating good agreement between experimental and calculated phase stability one needs to keep in mind that vibrational energies are not included in the calculations.

The occurrence of the Na-cI16 phase at 103 GPa (Fig. 100) marks the onset pressure for symmetry-breaking transitions in Na. The stability of this phase was tested in total energy calculations [J.B. Neaton *et al.*, Physical Review Letters **86**, 2860 (2001); N.E. Christensen *et al.*, Solid State Communications **119**, 477 (2001)] and it was found to become more stable relative to *fcc* at pressures of 110 GPa to 130 GPa, again in good agreement with the experimental observations. Several other structure candidates were also tested in the calculations, indicating that at higher pressures, but still within the range of DAC techniques, transitions to new phases of Na are to be expected. This does not rule out the possibility to find structures not yet tested in calculations or previously observed for other elements.

In conclusion, the light alkali metals Li and Na, considered to be simple in terms of their structural and electronic properties at ordinary conditions of temperature and pressure, adopt a complex structure at intermediate densities, not previously observed for other elemental solids. The new structure closely resembles the cation substructure of anti-Th_3P_4 (or Pu_2C_3) type compounds; the alkali metal atoms are arranged around interstitial sites which are occupied by the electro-negative partner in the binary compounds. A similar trend was noticed for high-pressure phases of the heavy alkali metals. The possibility of insulating phases of dense light alkalis, as envisioned by Neaton and Ashcroft, remains a subject of current interest. Lattice dynamical aspects of high-pressure phases of alkali metals have recently moved into the focus of theoretical studies. New insight is gained from microscopic theory into vibrational properties, electron-phonon coupling, and thermodynamics, along with some guidance for related experimental studies of physical properties.

A new polymorph of zirconium tungstate synthesized at high pressures and temperatures

A. Grzechnik; W.A. Crichton (ESRF, Grenoble); K. Syassen and P. Adler;
M. Mezouar (ESRF, Grenoble)

Zirconium tungstate, ZrW_2O_8, is a prototype example of a compound with a negative thermal expansion over a large range of temperatures [T.A. Mary *et al.*, Science **272**, 90 (1996); J.S.O. Evans *et al.*, Science **275**, 61 (1997)]. It is of interest for applications requiring materials with engineered thermal properties. Its very flexible structure at room temperature (space group $P2_13$) consists of ZrO_6 octahedra linked through oxygen atoms to WO_4 tetrahedra (Fig. 101). Above the second-order phase transition at 428 K, the structure of ZrW_2O_8 ($Pa\bar{3}$) is disordered with one oxygen site half occupied.

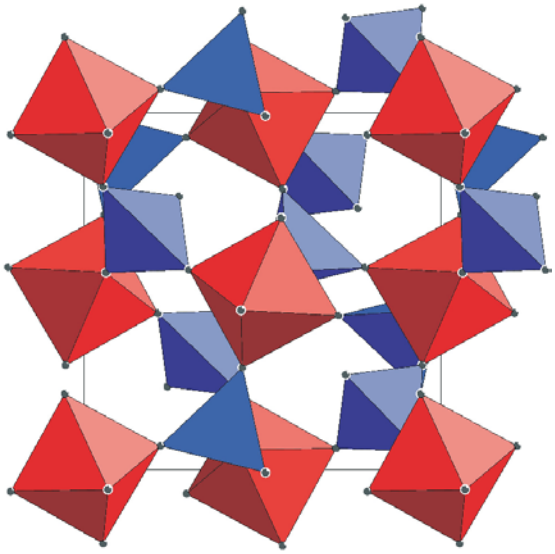

Figure 101: *Polyhedral representation of the crystal structure of zirconium tungstate ($P2_13$) at ambient pressure and room temperature. The structure consists of corner-linked ZrO_6 octahedra and WO_4 tetrahedra.*

The negative thermal expansion from 0.3 K to 1050 K, i.e., to the decomposition temperature, is due to rotational motions of the polyhedra rather than to changes in bond distances. At a pressures of 0.21 GPa (applied at room temperature) the $P2_13$ phase undergoes a first-order phase transition to an orthorhombic polymorph ($P2_12_12_1$). Upon further compression, in the range 1.5–3.5 GPa, ZrW_2O_8 irreversibly amorphizes. The mechanism of pressure-induced amorphization in this material has been described as involving uncorrelated tiltings of the polyhedra, kinetically frozen in an orientationally disordered state, with a possibility of changes in cation coordination.

Irreversible pressure-induced amorphization of oxides has attracted considerable interest in recent years [E.G. Ponyatovsky *et al.*, Materials Science Reports **8**, 147 (1992); S.M. Sharma *et al.*, Progress in Materials Science, **40**, 1 (1996)]. The effect is commonly attributed to the nucleation of a high-pressure phase from the parent polymorph. The thermal energy, however, is not sufficient to produce crystallites large enough for coherent X-ray diffraction. The amorphous state, not showing strict *P-T* existence fields, cannot be defined as a thermodynamically stable phase but as a state in a kinetic process. At room temperature, atom mobility and crystallite growth are hindered.

The results of our *in situ* angle-dispersive synchrotron X-ray powder diffraction studies show that the pressure-induced phenomena in the highly flexible framework of ZrW_2O_8 are more complicated [A. Grzechnik *et al.*, Chemistry of Materials **13**, 4255 (2001)]. Experiments at different pressure-temperature conditions were carried out using a large-volume pressure cell of the Paris-Edinburgh type installed on the beamline ID30 at the European Synchrotron Radiation Facility (Grenoble). ZrW_2O_8 was indeed found to amorphize above 1.5 GPa at room temperature (Fig. 102). The onset pressure for

amorphization decreases with increasing temperature both for the $P2_12_12_1$ and $Pa\bar{3}$ polymorphs. Depending on the pressure at which the amorphous sample is heated, either the *component oxides* or a *new crystalline polymorph* are obtained. This shows that the metastable amorphization is not necessarily a precursor phenomenon to a kinetically hindered phase transition, only.

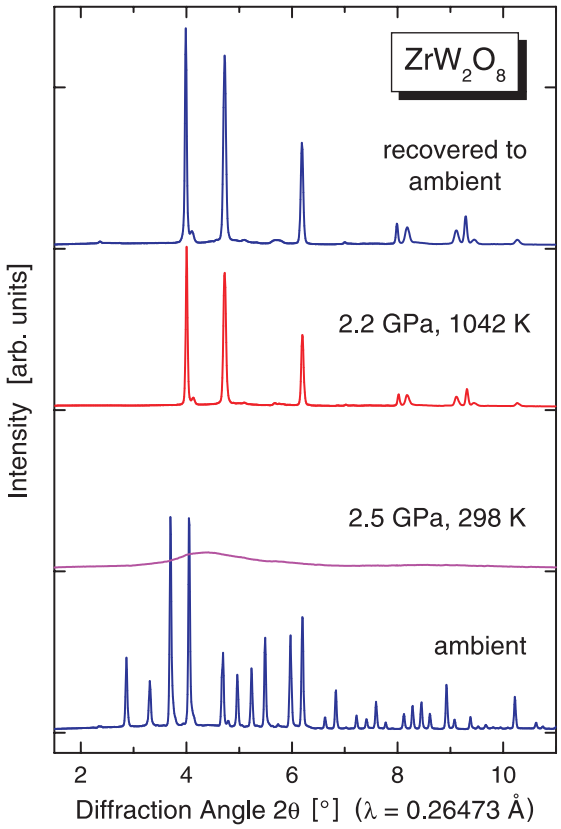

Figure 102: *Synchrotron X-ray powder diffraction diagrams of zirconium tungstate at different conditions of pressure and temperature. The ambient-pressure phase (bottom diagram) turns amorphous at 2.5 GPa and crystallizes into a new phase upon subsequent heating to 1042 K. The new phase can be recovered to ambient. Its structure is a cation-disordered analog of the α-U_3O_8-type structure.*

ZrW_2O_8 decomposes when the X-ray amorphous sample is heated *in situ* at pressures higher ($\approx$ 2.5 GPa) than that for the onset of amorphization. At slightly lower pressures the new phase of ZrW_2O_8 is obtained, which can be recovered at ambient conditions. A structure solution shows that it is of the α-U_3O_8-type (Fig. 103), with no resemblance of its framework to those of any other known polymorphs of related tungstates, molybdates, rhenates, etc.

In the structure of α-U_3O_8 ($P\bar{6}2m$, $Z = 1$) the cations occupy one Wyckoff *3f* site, while the oxygen atoms O(1), O(2) and O(3) reside at the sites *3f*, *3g*, and *2c*, respectively. The U atom is bonded to six oxygens at distances between 2.07 Å and 2.26 Å, with an additional oxygen atom located at 2.55 Å, i.e., the cations are in chains of vertex-sharing pentagonal bipyramids (Fig. 103).

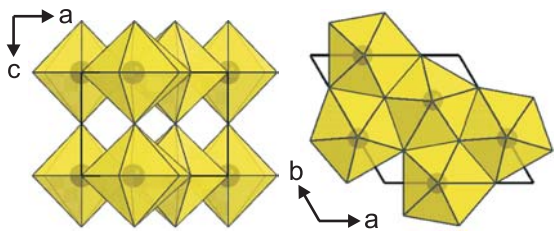

Figure 103: *The new hexagonal phase of zirconium tungstate ($P\bar{6}2m$ ($Z = 1$)) obtained after combined pressure and temperature treatment adopts a cation-disordered U_3O_8-type crystal structure formed by vertex-sharing pentagonal bipyramids with equatorial O(1) and O(3) atoms and apical O(2) atoms.*

There is excellent agreement between the observed pattern of the new phase of ZrW_2O_8 and the calculated one assuming the hexagonal U_3O_8 structural model with the U atoms replaced by Zr and W atoms with occupancies equal to 1/3 and 2/3, respectively, and with all the positional parameters for the cations and oxygen atoms fixed to the values given for α-U_3O_8. Adopting this structure implies that the Zr and W atoms are statistically disordered at the same crystallographic site and are both six-fold coordinated (with an additional distant oxygen atom). It should be noted that neither the patterns of the new phase collected *in situ* at high pressures and high temperatures nor its patterns measured at ambient conditions before and after annealing show any peak splitting or

anomalous anisotropic broadening that would suggest lower symmetry of the structure, i.e., possible ordering of the Zr and W cations in the lattice, in a fashion similar to the temperature effects in the orthorhombic and hexagonal phases of U_3O_8.

The packing of atoms in the α-U_3O_8-type structure of ZrW_2O_8 is more efficient than that in the highly flexible frameworks found in the $P2_13$, $Pa\overline{3}$, and $P2_1P2_12_1$ phases as, for instance, inferred from the comparison of the unit cell volumes – the unit cell volume of 135.21 Å^3 in the $P\overline{6}2m$ ($Z = 1$) phase is 42% and 35% smaller, respectively, than the volumes for one formula unit in the $P2_13$ and $P2_12_12_1$ polymorphs.

Our observations show that there occur *two competing and kinetically constrained pressure-induced processes* in zirconium tungstate as a result of a complete collapse of the mixed tetrahedral-octahedral framework: a *structural transformation* to a dense crystalline phase or a *decomposition* into component oxides. It should be recalled that in the pressure region studied in this work, the coordination number for the W atoms in WO_3 is six, while the coordination number for the Zr atoms in ZrO_2 is seven. Hence, from the crystal chemistry point of view, the driving force for the breakdown of the framework of ZrW_2O_8 is the pressure instability of the tetrahedral coordination around the W atoms leading to the formation of the α-U_3O_8-type phase at pressures just after the amorphization has been completed or to the decomposition into component ZrO_2 and WO_3 oxides at higher pressures.

We expect that *in situ* studies of the interplay between the two competing processes in several other highly flexible framework compounds at high pressures and high temperatures may lead to the synthesis of novel materials.

Diffuse scattering in partially ordered crystals

L. Kienle, V. Duppel, and A. Simon

The crystalline state is usually characterized by a unit cell which is reproduced in three dimensions by translation. For many important materials (e.g., YSZ and other ionic conductors) the 3D periodicity is broken, due to the existence of prominent disorder in the crystals. Experimentally the disorder results in diffuse scattering which can be observed by diffraction experiments. A second useful tool for the *direct* observation of disorder is high resolution electron microscopy (HREM).

We examined complex chalcogenides which are characterized by diffuse ring-shaped intensities in defined layers of the reciprocal space. These diffuse reflections show no significant extension in $[001]^*$ corresponding to 1D ordering of the crystallites in [001] of direct space. A common feature of all compounds is the hexagonal lattice and the possibility to divide the structures into two parts, an ordered honeycomb host lattice and rods which are inserted in the latter ones, respectively, see Fig. 104(a).

The translational symmetry of the host lattice allows two different positions (referring to [001]) of the otherwise identical rods (called rod A and rod B). The configurations of neighbored rods (AA, BB or AB) are essential for the understanding of the diffuse scattering.

In the case of $K_2In_{12}Se_{19}$ a dynamical disorder of the configurations is observed at $T > 400°C$ which is transformed into a statical one at lower temperatures. The associated formation of antiphase domains (configurations AA or

BB) limits the disorder to the domain boundaries which are characterized by the configuration AB. A structural analysis of the possible configurations of neighbored rods shows significant differences in the local structure. The configurations AA and BB result in a remarkably short interatomic distance for some indium atoms of neighbored rods ($d_{\mathrm{In-In}} = 3.528$ Å), see Fig. 104(b). The alternative configuration AB exhibits an enlarged distance between the indium atoms ($d_{\mathrm{In-In}} = 4.049$ Å), see Fig. 104(c). Hence the formation of crystals with a high density of the antiphase boundaries (APB) can be expected.

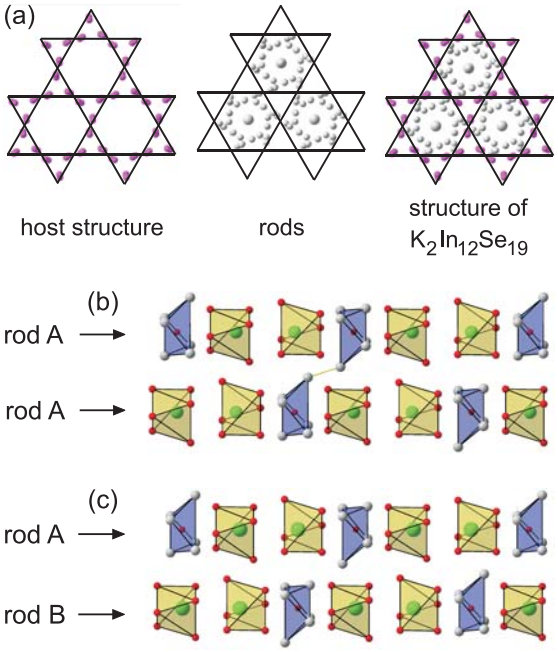

Figure 104: *(a) Description of the structure of $K_2In_{12}Se_{19}$ (right) by the concept of rods (middle) which are inserted in a host structure (left). Projections on (001). (b) and (c) Neighbored rods in the structure of $K_2In_{12}Se_{19}$. The coordination of the atoms Se1 (by In) and K1 and K2 (by Se) are displayed in polyhedral representation. (b) Neighbored rods in position A generate an unusually short distance d_{In-In} (indicated by the line), (c) one rod in position A and one rod in position B, the short distance does not occur.*

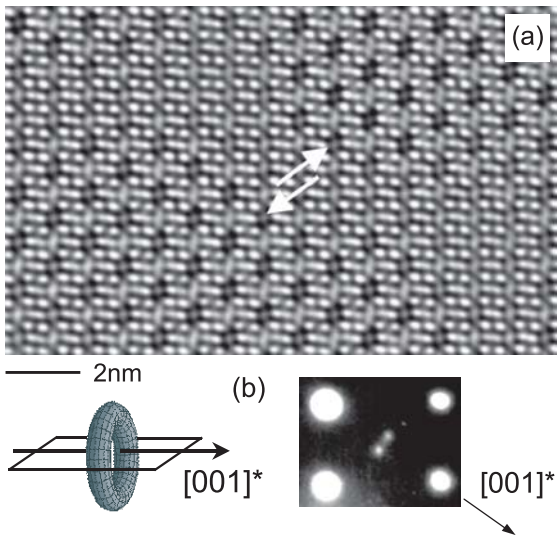

Figure 105: *(a) HREM of ordered domains separated by APB for $K_2In_{12}Se_{19}$ (zone axis [111], $\Delta f = 10$ nm). The arrows indicate the shift of the structure at the boundary. (b) Cutting of a torus by a layer results in two intensity maxima. Schematically representation left, selected area diffraction (SAED) of zone axis [100] right.*

For $K_2In_{12}Se_{19}$ the formation of the partially ordered crystals can be observed experimentally. At the boundary of two domains a characteristic shift of the structure occurs, see the HREM micrograph in Fig. 105(a), which can be interpreted using a model of a real structure that includes the above mentioned antiphase boundaries. The relative shift of the domains represents the difference of the positions A and B of the rods. The sizes of the single ordered domains and the orientations of the domain boundaries exhibit an essential influence on the shape of the diffuse intensities. The diffuse scattering manifests itself only in higher order Laue zones of [001] as diffuse rings. In all other orientations we observed two sharp and very close intensity maxima which result from cutting the diffuse rings through their centers (e.g., for [100], see Fig. 105(b)).

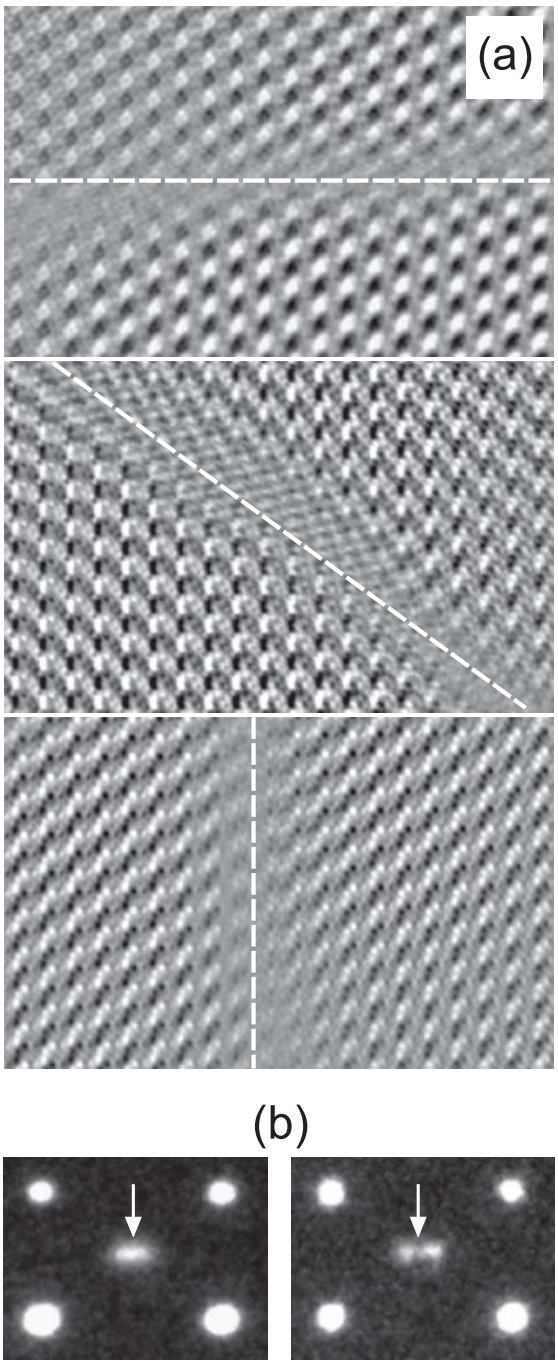

Figure 106: *(a) HREM micrographs after image processing. The different orientations of the domain boundaries (referring to the host lattice) is evident, see broken lines. (b) Enlarged sections of SAED patterns recorded on one crystallite.*

Our observations indicate random orientations of the domain boundaries in (001) to be responsible for the circular shape of the diffuse scattering (see the processed micrographs in Fig. 106(a) for zone axis $[\bar{1}11]$). Only in small areas of the crystallites the averaging is not perfect and the circular shape of the diffuse scattering is modified as indicated by selected area diffraction (SAED). A second important point concerns the sizes of the domains, which determine the diameter of the diffuse rings. Experimentally we found for instance variations of the distance between the diffuse intensity maxima in dependence of the domain size. The SAED patterns in Fig. 106(b) were taken from different regions of *one* crystal. As indicated by the smaller distance of the intensity maxima the left pattern was recorded by focusing on an area with larger domains.

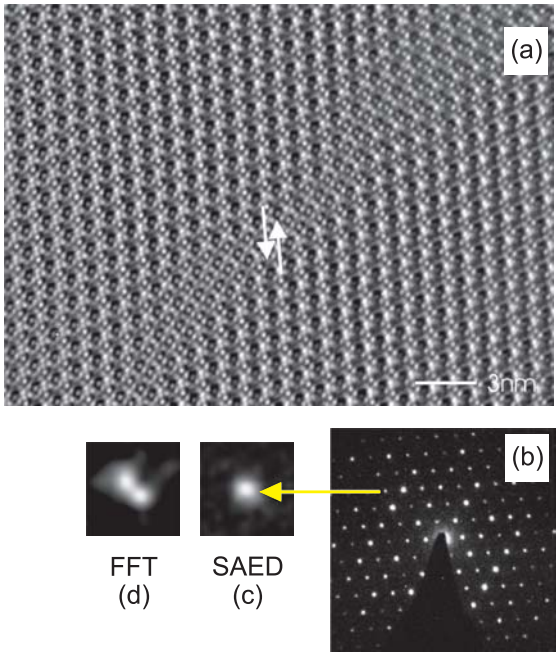

Figure 107: *(a) HREM of ordered domains separated by APB for $K_2In_{12}Se_{15}Te_4$ (zone axis [111], $\Delta f = 10$ nm). The arrows indicate the shift of the structure at the boundary, (b) SAED performed on this crystal exhibits no diffuse scattering (see enlarged section in (c)), (d) enlarged section of the Fourier transform of picture (a) displaying clearly diffuse scattering.*

Chemistry also has a large influence on the real structure and therefore on diffuse scattering. In the cases of $K_2In_{12}Se_{14}Te_5$ and $In_4SSe_2Te_3$ no diffuse reflections can be observed by diffrac-

tion methods (X-ray and electrons), but the HREM micrographs display clearly the presence of APB (see Fig. 107 for zone axis [111]) and the existence of very large ordered single domains related to the pure selenium compound. The Fourier transforms of selected regions of the images emphasize the diffuse character of the reflections (see enlarged sections in Fig. 107) and underline that it is possible to get information about the real structure by HREM that could not be derived by any diffraction method.

Direct imaging of catalytically important processes in the CO oxidation over $RuO_2(110)$

H. Over and A.P. Seitsonen; E. Lundgren, M. Schmid, and P. Varga (TU Wien)

Ruthenium dioxide (RuO_2) reveals unique and promising redox properties, making RuO_2 a potential candidate for a versatile oxidation catalyst. In the bulk rutile structure of RuO_2 the Ru atoms are six-fold coordinated to oxygen atoms, while the O atoms are coordinated to three Ru atoms in a planar sp^2 hybridization. On the stoichiometric $RuO_2(110)$ surface two kinds of under-coordinated surface atoms are stabilized (Fig. 108(a)). These are the bridging oxygen atoms O_{br}, which are coordinated only to two Ru atoms underneath, and the so-called 1f-cus-Ru atoms, i.e., one-fold under-coordinated Ru atoms. In Fig. 108(b) we show an experimental 5 nm×5 nm STM image of this surface taken at room temperature (RT). Clearly, there are rows of protrusions visible along the [001] direction. STM simulations (Fig. 108(c)), using the Tersoff-Hamann model within DFT indicate that the bridging oxygen atoms are imaged as bright regions. This result is quite remarkable as for the $TiO_2(110)$ surface the observed protrusions in STM images were ascribed to 1f-cus-Ti atoms. It demonstrates also that an interpretation of STM images needs additional information, such as provided by DFT calculations.

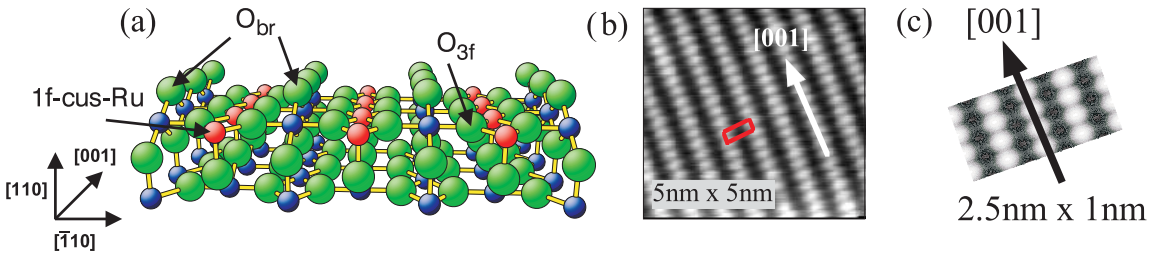

Figure 108: *(a) Stick and ball model of the stoichiometric $RuO_2(110)$ surfaces. O and Ru atoms are shown as large and small balls, respectively. A bridge bonded (O_{br}), a threefold coordinated O atom (O_{3f}) and a one-fold under-coordinated Ru atom (1f-cus-Ru) are indicated. (b) Experimental STM image (constant current mode, taken at room temperature) of a stoichiometric $RuO_2(110)$ surface: 5 nm×5 nm, U = –0.01V, I = 0.46 nA. (c) STM simulation of the stoichiometric $RuO_2(110)$, using the Tersoff-Hamann model. The origin was set to the lateral position of Ru atoms attached to the O_{br} atoms. Therefore the bright spots seen in the simulated STM image are uniquely assigned to bridging O atoms.*

The extraordinarily high activity of stoichiometric $RuO_2(110)$ towards CO oxidation was demonstrated (on the atomic scale) to be controlled by the presence of one-fold coordinatively unsaturated Ru sites (1f-cus-Ru). We emphasize that not defects but rather the regular, under-coordinated surface atoms determine the activity of RuO_2. On the stoichiometric $RuO_2(110)$ surface, CO molecules adsorb strongly (adsorption energy exceeding 1.2 eV) on-top of the 1f-cus-Ru atoms from where the actual oxidation reaction takes place via recombination with undercoordinated (and therefore weakly bound) bridging oxygen to form CO_2 (so-called Mars-van Krevelen mechanism). If several neighboring bridging oxygen atoms have been removed, two-fold coordinatively unsaturated Ru sites (2f-cus-Ru) are created, offering two dangling bonds for the bonding with molecules from the gas phase.

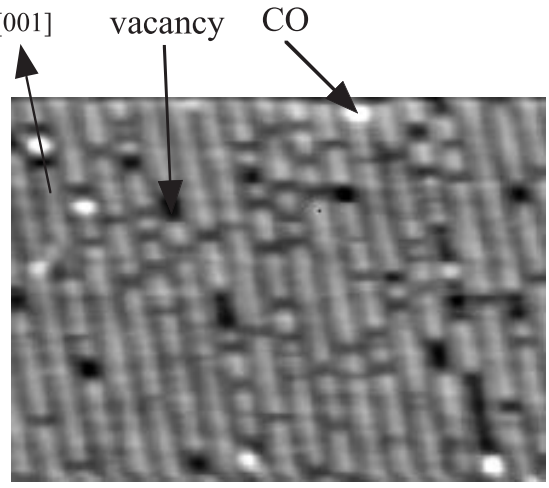

Figure 109: *13 nm × 7 nm STM image (constant current mode, RT) of the (partially) reduced $RuO_2(110)$ surface that was prepared by exposing 0.5 L CO at 370 K. U = 0.01 V, I = 0.46 nA. The rows of bridging O atoms (bright rows) are interrupted by single and grouped vacancies. The single bright features are assigned to adsorbed CO molecules on the vacancies along the bridging O rows.*

In Fig. 109 this removal of bridging oxygens is verified by an STM image that was taken after the stoichiometric $RuO_2(110)$ surface had been exposed to 0.5 L CO at 370 K. The bright rows reveal isolated vacancies and strings of vacancies. Occasionally isolated bright spots are visible in the vacancies along the bridging oxygen rows, i.e., above the 2f-cus-Ru atoms. These features are assigned to adsorbed CO molecules. The adsorption energy of a single CO molecule substituting a bridging O atom is 1.73 eV. If all O_{br} atoms have been removed, CO molecules bridging the 2f-cus-Ru atoms or terminating the 1f-cus-Ru atoms are bound by 1.85 eV and 1.61 eV, respectively. The activation barriers for CO diffusion are of the order of 1 eV. Therefore, at room temperature the CO molecules can be imaged by STM.

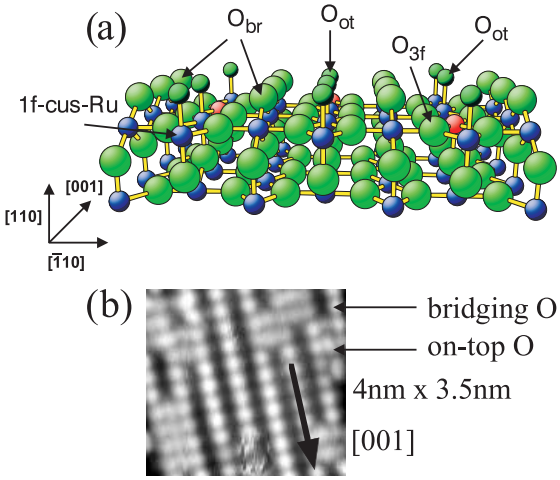

Figure 110: *(a) Stick and ball model of the stoichiometric $RuO_2(110)$ surfaces covered with weakly bound oxygen (O_{ot}) in on-top position above the 1f-cus-Ru atoms. O and Ru atoms are indicated as large and small balls, respectively. (b) STM image (constant current mode, room temperature) of the $RuO_2(110)$ surface which was exposed to 0.1 L oxygen at room temperature. U = 0.01 V, I = 0.46 nA.*

An equally important process is the facile reoxidation of a (partially) reduced $RuO_2(110)$ surface by oxygen supply from the gas phase. A weakly held oxygen species was found to adsorb on-top of the 1f-cus-Ru atoms (Fig. 110(a)), and it has been argued that this species actuates the restoration of the reduced $RuO_2(110)$ surface. The latter process is mandatory to keep the oxide catalyst active under reaction conditions. Oxygen molecules

from the gas phase can efficiently dissociate on $RuO_2(110)$ with a sticking probability of 0.8 at room temperature.

Exposing the stoichiometric $RuO_2(110)$ surface to oxygen at room temperature stabilizes a weakly held oxygen species that desorbs at about 450 K. In Fig. 110(b) we show an STM image of such a prepared $RuO_2(110)$ surface. Clearly additional bright features are visible in this image if compared to the stoichiometric surface (Fig. 108(b)). From the registry of these new features with respect to the bridging O atoms, the weakly held oxygen is inferred to adsorb on-top of the 1f-cus-Ru atoms. Another important aspect is that the protrusions in the STM image appear almost always as pairs, indicating that the mobility of the weakly held oxygen species is limited at room temperature. This observation supports the view that the molecular oxygen species is the precursor state for the dissociation process. At temperatures below 140 K molecular oxygen lies down on the $RuO_2(110)$ surface (as an intact entity), bridging two adjacent 1f-cus-Ru atoms. On increasing the sample temperature, the molecular oxygen dissociates and forms terminal Ru–O bonds to the 1f-cus-Ru atoms. Since the diffusion barrier of the on-top O species is so high (1.2 eV along the [001] direction as determined by DFT calculations) even at room temperature the on-top oxygen atoms are primarily grouped in pairs. However, if there is an adjacent vacancy in the rows of O_{br}, the diffusion barrier of oxygen to migrate from the 1f-cus-Ru to the 2f-cus-Ru site is only 0.7 eV. Therefore this diffusion process is very likely at room temperature and correspondingly important for the restoration of a mildly reduced $RuO_2(110)$ surface.